Cranfield University

Abdullatif Al-Alshaikh

An Experimental and Numerical Investigation of the Effect of Aero Gas Turbine Test Facility Aspect Ratio on Thrust Measurement

School of Engineering

PhD Thesis

Cranfield University

School of Engineering

PhD Thesis

August 2011

Abdullatif Al-Alshaikh

An Experimental and Numerical Investigation of the Effect of Aero Gas Turbine Test Facility Aspect Ratio on Thrust Measurement

Supervisor: Prof. P. Pilidis and Dr. P. Laskaridis

This thesis is submitted in fulfilment of the requirements for the degree of Doctor of Philosophy

Abstract

This work describes the outcome of research program investigating thrust measurements in enclosed test facility for modern aero gas turbine engines. Literature work, experimental work and a description of Computational fluid dynamics simulation system have been developed to improve the accuracy of test bed thrust measurement.

The key parameters covered in the research include test house size in relation to engine size. The effect of the distance of engine to detuner on the thrust correction factor was also investigated. The rule of loss mechanism within the test facility to include intake momentum drag, cradle drag, base drag, recirculation on loss and intake exhaust losses loss. The thrust correction factor prediction technique available in the open literature are compared with the result given by this research and conclusion are drawn. CFD predictions show that the biggest difference with experimental data is only 1 % in TCF for the largest test cell size. For the smallest test cell this difference increases to only 2%. These results in terms of accuracy are lower than what would normally be expected for general CFD work.

The major contributions to thrust measurement technology include the following:

1. The research was able to ascertain that as engine size increases it will become more risky to rely on test bed results as giving an accurate prediction of static thrust.
2. The work has enabled confident prediction that test bed results can give test bed static thrust compared to free air testing with an accuracy of one half of 1%.
3. Using Fluent it has been possible to reproduce a comparable comparison with test bed results. This will give the user of the research a higher level of confidence in predicting thrust measurements for test beds whose size is small in comparison with engine size.
4. It is of course an ambition for all those working in the field to eliminate engine testing. However this is unachievable ambition. This research has shown the way to improve CFD prediction towards achieving this ambition.

Finally detailed recommendations are given for continuation for this research program.

Acknowledgement

First of all I like to thank ***ALLAH*** *who has complete knowledge and guides me in every field of life and enabled me to complete my thesis.*

It is a pleasure to thank the people who made this thesis achievable. I am thankful to my supervisor Dr. P. Laskaridis for his supervision. I would like to express my sincere gratitude to my supervisor Professor P. Pilidis and to Dr. K. W. Ramsden whose encouragement, guidance and support enabled me to complete my thesis. I would also like to thank Mr. B. Charnley , Mr S. Booden for their patience and help to finish my experiments. Thanks to all staff of the Power and Propulsion department for their help. And of course there is always a helping hand when needed from Mrs G. Hargreaves, Mrs. N. Datt, and Mrs S. Sheen.

Also I thank my friends in Islamic society and Saudi society, especially Mr. S. Askar, for their understandings, prayers and supports to completing this project.

An honourable mention goes to my mother and father for supporting me spiritually throughout my life. Thanks to all my family, brothers and sisters for their support and encouragements.
My sincere thanks to my wife for all the support during the years I have been working on this thesis, especially all the great environment she provided to me to write and to talk to her about my project.
To my beloved children, Muneerah, Abdullah, Abdulaziz, and Osama.

Finally thanks are due to King Abdulaziz City for Science and Technology for funding this project.

Contents

List Of Figures

List of Tables

Nomenclature

Greek Symbols

Δ	Difference
λ	Cell Cross Sectional Area / Engine Throat Area
θ	Angle between the Axial and the Tangential Direction
π	One radiant
ρ	Density
τ	Shearing Stress
Φ	Axial Force
Φ_v	Axial Viscous Force
ψ	Porosity
μ	Entrainment Ratio: $W_{secondary}/W_{primary}$

Symbols

A	Area
atm	Atmospheric Condition
aver	Average
b	Area Cell station (9) over Area Cell at Section (0) ratio
bell	Bellmouth
Cp	Pressure Coefficient
cp	Specific Heat at Constant Pressure
Cd	Drag Coefficient
$Cd_{overall}$	Discharge coefficient for the Blast Basket
cell	Test Cell Conditions
comb	combustion

Cx	Measured over Calculated Thrust Ratio
D	Diameter
D_c	Collector diameter
D_{cell}	Detuner Diameter
D_{det}	Nozzle diameter
D_n	Engine Nozzle Diameter
D_{noz}	Drag of the Metric Assembly Until Station (9')
D'_{metric}	Drag of the Engine Carcase Until Station (9')
D'_{metric}	Element of Area Normal to the Axial Direction
dA	Element of Area
eng	Engine
ext	external
F	Absolute Force
F_m	Load Measure by the Load Cells
F_N	Standard Net Thrust
F'_N	Overall Net Thrust
f	Area Engine at Station (f) over Area Cell at Section (0) ratio
G	Gauge Value
H_c	Distance from the floor to the engine centre line
i	Inlet
L	Load Measured by the Load Cells
m_i	Induced air mass flow
m_n	Nozzle air mass flow
max	Maximum
metric	Metric-assembly

min	Minimum
N	Running Speed
noz	Nozzle
P	Stagnation Pressure
p	Static Pressure
R	Universal Gas Constant
T_i	Induced air total temperature
T_i	Nozzle air total temperature
t	Static temperature
v	Velocity
W	Mass Flow
(f)	Test Cell Defined Behind the Bellmouth
(f_{ext})	Test Cell Defined Behind the Bellmouth, Excluding the Engine portion of Area
(f_{int})	Test Cell Defined Behind the Bellmouth, Including the Engine portion of Area
(0)	Test Cell Reference Section Up-Stream to the Engine
(0_{ext})	Test Cell Reference Section Up-Stream to the Engine, Excluding the Pre-Entry Stream Tube Cross Sectional Area
(0_{int})	Test Cell Reference Section Up-Stream to the Engine, Including only the Pre-Entry Stream Tube Cross Sectional Area
(1)	Test Cell Section Defined by the Stagnation Point of the Pre-Entry Stream Tube on the Bellmouth
(1_{ext})	Test Cell Section Defined by the Stagnation Point of the Pre-Entry Stream Tube on the Bellmouth, Excluding the portion of area Internal the Bellmouth
(1_{int})	Test Cell Section Defined by the Stagnation Point of the Pre-Entry Stream Tube on the Bellmouth, Excluding the portion of area External the Bellmouth
(9)	Test Cell Section Defined at the Engine Nozzle Plain

(9_{ext})	Test Cell Section Defined at the Engine Nozzle Plain, Excluding the Nozzle Area
(9_{int})	Test Cell Section Defined at the Engine Nozzle Plain, Including only the Nozzle

Sub-Scripts

Atm	Atmospheric Condition
BF	Bypass flow
BM	Bellmouth
FC	Front cell
m	Mixing Region
m'	After-Mixing Region
pot	Potential Flow
pre	Pre-Entry
ref	Reference Section
s	Secondary Flow
st	Stone Guard
th	Throat Section
2	Accommodation Region Section

Abbreviations

AIAA	American Institute Aeronautic and Astronautic
AEDC	Arnold Engineering Development Centre
AGARD	Advisory Group for Aerospace Research and Development
ARC	Aeronautical Research Council
A.R.	Accommodation Region
ATF	Altitude Test Facility

CFD	Computational Fluid Dynamic
FAR	Fuel Air Ratio
GE	General Electric
IMD	Intake Momentum Drag
ISA	International Standard Atmosphere
MFR	Mass Flow Ratio A_0/A_1
MIDAP	Ministry-Industry Drag Analysis Panel
MPH	Miles per Hour
M.R.	Mixing Region
ndmf	Non Dimensional Mass Flow
NGTE	National Gas Turbine Establishment
NPF	Net Propulsive Force
P.R.	Preliminary Region
RANS	Reynolds-Average Navier Stokes
RR	Rolls-Royce
SLTF	Sea-Level Test Facility
TCF	Thrust Correction Factor
UETP	Universal Engine Test Program

1. Introduction

Gas turbine testing is essential for both the manufacturers and clients. Manufacturers need to prove the engine's thrust and to ensure the overall capabilities. Gas turbine can be tested for different purposes. Testing might be done during the development phase for research and development. It might be also carried regularly during the engine operation life. The later type of testing could be carried out by the engine user based on the designer authority specifications. Generally, engine test might be categorised in different types:

- Research program testing for each component;
- Routine testing, maintenance and troubleshooting;
- Development or prove testing for new or existing engine.

Two types of test facility are being used, sea-level and altitude test facility. On sea level, an engine might be tested either indoors or outdoors. Outdoor test bed with zero cross wind will give the best reference of the gross thrust. The problem is the noise limitation which leads to have the test bed in remote area. Weather also is not predictable and might be a big time consumer so long time of delay might happen. These types of conditions make the indoor test cell more attractable since there is a good development in the noise isolation. Of course, this will save money in terms of time.

Outdoor testing with zero cross wind is the best testing environment whereas no air disturbance or drag forces to be accounted. At this condition the measured thrust will be used as a reference for the corrected measurement inside the cell.

1.1. Research Aim

This research work concentrates on the subject of aero gas turbine testing in enclosed sea level test facilities. When an engine is tested indoors, in addition to the primary flow going into the engine, secondary air will also be induced into the test cell. This secondary air will flow around the engine and will affect the flow characteristics within the cell as well as the performance of the engine. The ratio of secondary air to the primary air is defined as entrainment ratio. Entrainment ratio is one of the main

parameters used to describe the performance of the engine-cell system. Although the secondary air is required to avoid hot gas re-ingestion, cool down the exhaust section of the cell and minimize the jet noise generated by the primary flow, it has a detrimental effect on the thrust measured and the integrity of the cell. The presented work examines the impact of changing the test bed size on the thrust measurements.

Based on the above it is the scope of the present thesis to build on the previous work and examine the effect of the cell aspect ratio (defined here as the ratio of the cross section area of the cell to the intake area of the engine) on the entrainment ratio and the thrust correction factors. Changing the aspect ratio of the cell will have an impact on the flow characteristics and the pressure distribution within the test cell which will have a pronounced effect on the thrust measured.

1.2. Research Objectives:

The objectives of the current research are as follows:

- Investigate the impact of the test bed size on the thrust correction factor by experimental testing.
- Investigate the impact of the test bed size on the thrust correction factor by computational fluid dynamics simulation.
- Explore and select the best and direct applicable thrust correction equation to be used in the research experiments.
- Compare the CFD derived thrust correction factor to the back to back experimental thrust correction factor.

1.3. Study contribution

The author individual contributions to knowledge include the following:

- The research is able to ascertain that as engine size increases it will become more risky to rely on test bed results as giving an accurate prediction of static thrust.
- The work has enabled confident prediction that test bed results can give test bed static thrust compared to free air testing with an accuracy of one half of 1%.

- Using Fluent it has been possible to reproduce a comparable comparison with test bed results. This will give the user of the research a higher level of confidence in predicting thrust measurements for test beds whose size is small in comparison with engine size.
- It is of course an ambition for all those working in the field to eliminate engine testing. However this is unachievable ambition. This research has shown the way to improve CFD prediction towards achieving this ambition.

1.4. Thesis Structure

Chapter one gives an introduction of the gas turbine sea level indoor testing. The aim of this research work is given with a list of the objectives.

Chapter two gives a literature review of the gas turbine testing. It starts by defining the types of gas turbine testing facility including the advantages and disadvantages of each type and a detail description of indoor and outdoor gas turbine sea level testing. It presents a detail description of structure for the indoor testing facility.

Chapter two provides a literature review on enclosed test facility for aero gas turbine engines at sea-level. There is a description for the outdoor sea-level test facility and its purpose. The chapter also includes a description of the components of the indoor test facility. The work covers three main components of the indoor test facility; inlet system, test chamber and exhaust system.

Another five parts describe some flow phenomena which take place inside the test facility like vortex formation, flow distortion, flow separation, air recirculation, and cell depression. Each part includes useful guidelines to avoid the effects of such adverse flow phenomena on the stability of the engine and the measurement systems.

The second part of the literature review is dedicated to past studies of the effects of engine-detuner ejector pump on the flow inside the cell. In particular, different ejector parameters are taken into account such as the spacing between the engine and the detuner, the nozzle-detuner diameter ratio and the primary jet conditions. Furthermore,

an energy balance inside the cell is proposed as a method for computing the cell entrainment ratio.

The third part describes the ejector pump effect which takes place as a result of the interaction between the engine nozzle and the detuner. A method of calculating the test cell entrainment ratio is provided. Furthermore, the effect of three main parameter on the ejector pump effect are given.

The fourth part of the literature review covers the thrust correction factors. Moreover the next two parts The Rolls-Royce and the ITP thrust measurement methods are reported.

The last part of the literature review gives the thrust correction equations which have been derived to be applied to small aspect ratio of test facility

Chapter three covers the experimental approach which has been used in this research work. It starts with the experimental setup and the instrumentations. After that the measurements are provided which are followed by the produced results and the discussion.

Chapter four is describing the computational fluid dynamics approach. There is an introduction of the targeted modeled and a description of the used software and the pre-processing steps. Furthermore the methodology for deriving the thrust correction factors are provided. The last part discuss the results and a comparison of the CFD analysis results to the experimental results.

Chapter five discusses the conclusion of the presented work and an outline of the research future work is provided.

Chapter six has a list of all reference that are used in this thesis.

Final section of this thesis is the appendix which have all supportive tables for the experiential and CFD work and results.

2. Literature Review

2.1. *Sea-Level Test Facilities*

Sea-Level test cells for gas turbine engine can be divided in two groups: the outdoor stands and the indoor or enclosed test cell. An outdoor cell consists basically of an open air stand supporting the engine and providing the thrust measurements. The immediate test bed area has to be free of obstructions to assure the validity of the thrust measurements and to avoid flow distortion which can affect the engine performance. Also the thrust stand is located at a suitable elevation off the ground to eliminate inlet flow interferences.

Figure 2.1 shows a general lay-out for outdoor cells and Figure 2.2 is a picture of Rolls Royce new outdoor test facility. From this picture it is possible to notice that the airmeter inlet is a bellmouth. Indeed, in the design of these facilities special attention is dedicated to avoid the influence of ambient disturbances as the wind which could seriously affect the test results. For this reason the bellmouth can also be supported by a large mesh screen fitted around the engine (Walsh and Fletcher, 1998).

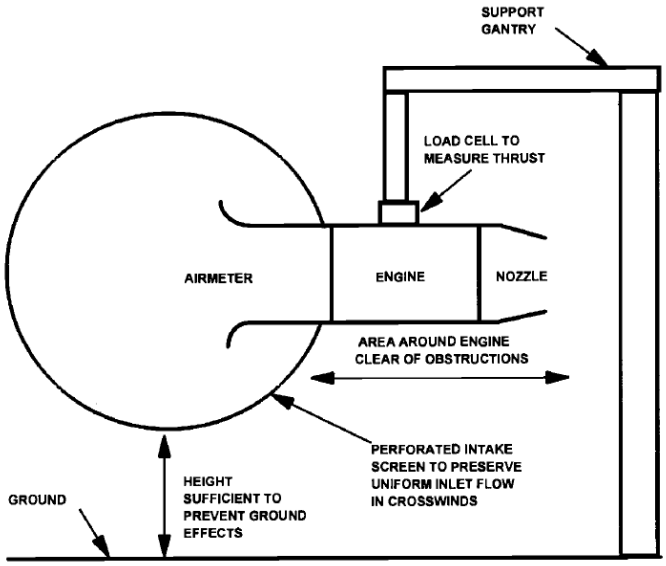

Figure 2.1 Outdoor Test Facility Lay-Out (Walsh and Fletcher, 1998)

A general indoor test cell is a set of buildings consisting of the test-bay with inlet and outlet channels, the control room, preparation area and the equipment room. The test bay (or test main chamber) is the section where the engine is located in its thrust measurement stand during the test. From the control room the engine is fully controlled

during the test. Often, this is also the room where all the data acquisition systems and data reduction processors are located.

Figure 2.2 Rolls-Royce plc Outdoor Jet Engine Test Facility (mdsaero.com)

The preparation room is the area where the engine is set-up prior to the test in order to minimise the non-running time of the engine inside the test room. The equipment room is dedicated to the storage of the compressed air for the cell and the engine, fuel for the engine and all the components for providing the engine with the needed power electricity. Figure 2.3 shows a plan view of the Glen Test House. It includes a control room, a clean room for the servicing and a fuel System test facility.

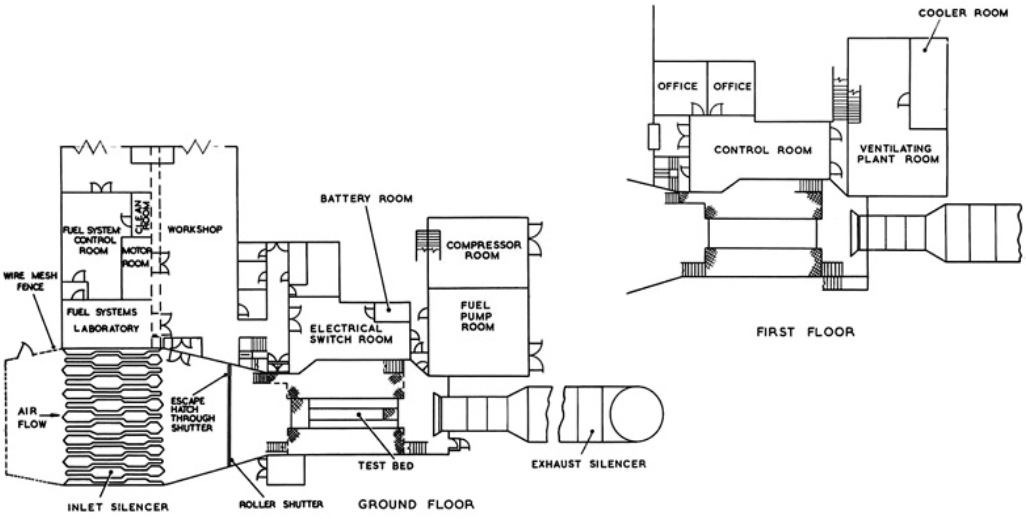

Figure 2.3 Plan layout of indoor test facility, the'Glen' test house (www.ngte.co.uk)

There are several kinds of tests which the facility can deal with and therefore a unique configuration to allow all of them is not possible. It is also worth to mention that the indoor test facilities are used for testing turbo shaft engines as well but the indoor test cells taken into account are specifically designed for turbojet or turbofan engines as these facilities represent the core study of this work.

2.2. ENCLOSED SEA LEVEL TEST BED CONFIGURATION

Figure 2.4 is a schematic representation of a typical enclosed sea level gas turbine test cell. As can be seen, the cell basically comprises of the inlet, the test chamber, and the exhaust. The designs of these regions are briefly discussed below.

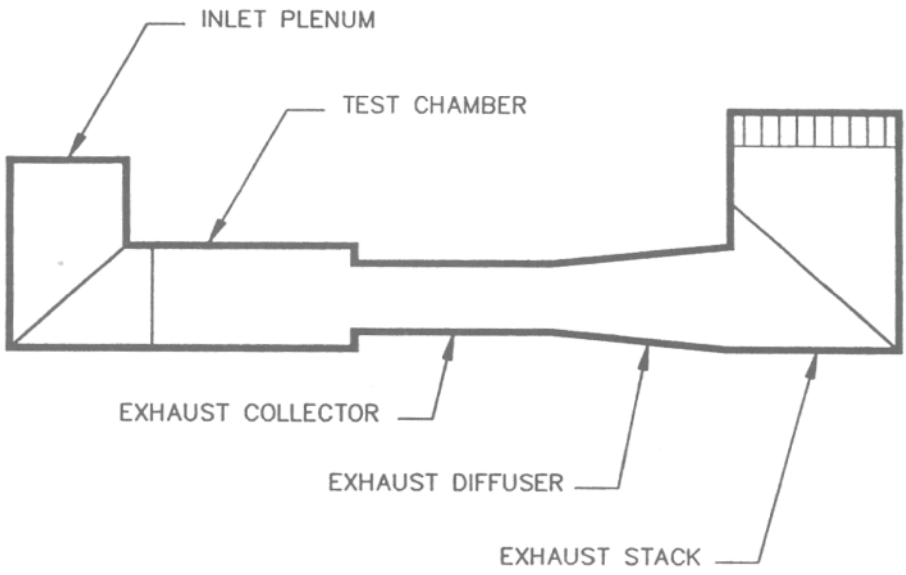

Figure 2.4 Major Test Cell Areas of Consideration (Rudnitski, 1990)

Within any given space constraints the inlet acts to make the flow into the test chamber as uniform and smooth as possible over the operating range of the engine. This is done with flow straighteners which minimise turbulence effects. These features are discussed below.

The engine is mounted securely within the test chamber, on the test frame. To enable measurements of cradle thrust using strain gauges fixed relative to the earth, it is necessary for the frame to have a small degree of axial movement. Because the test chamber houses the engine under test it is provided with the necessary services; fuel, a high pressure air supply to start the engine, electrical power and any instrumentation

required to monitor liquid and/or gas pressures, temperatures, flows or vibration monitoring of the engine.

The exhaust region has the job of reducing the noise radiated from the engine and cooling the gases emitted from the engine nozzle to atmosphere. All the products of combustion from the engine and the secondary air that is flowing past the outside of the engine pass through the exhaust. The position of the exhaust stack must be such that there is no possibility of exhaust gases being drawn back into the inlet and re-ingested into the gas turbine. Such conditions would not only be unrepresentative of the conditions in which the engine would be used, but could actually damage the engine.

2.3. Test Cell Air Inlet System

The test cell inlet system must meet a number of design criteria: it must not be too expensive, it must not be too large, it must reduce engine noise to a reasonable level, it should produce minimum pressure loss of the air flowing through it so that an adequate supply is delivered across the test engine's power range, it must isolate the internal environment from the external so that the air flowing to the engine is clean and the flow is unaffected by e.g. cross winds, dust or rain.

2.3.1. Air Intake

Typically, air intakes are either vertical or horizontal, see Figure 2.5 and Figure 2.6. The balance is between a smoother and more uniform air flow to the engine with a horizontal intake because the flow is directly to the engine without having to turn through 90^{o}, or fewer ground effects and less dust ingested with the vertical intake which can be several metres above ground level. Additionally, because the airflow from a horizontal intake to the engine can be strongly influenced by external wind behaviour it is usual to shield such intakes from cross winds by building side walls in front of the test chamber. Unfortunately, this can help generate eddy phenomena in the airflows close to the inlet; just the type of flow distortion the inlet should be designed to avoid. On the other hand the design of the vertical intake can take advantage of the 90^{o} turn in the air flow to largely eliminate shear effects due to wind direction.

Horizontal intakes are usually less likely than vertical intakes to re-ingest engine combustion products emitted from the exhaust. Not only must the physical separation of inlet and exhaust be adequate, it is also important to avoid placing the exhaust stack upwind of the inlet, particularly if the inlet is to be vertical.

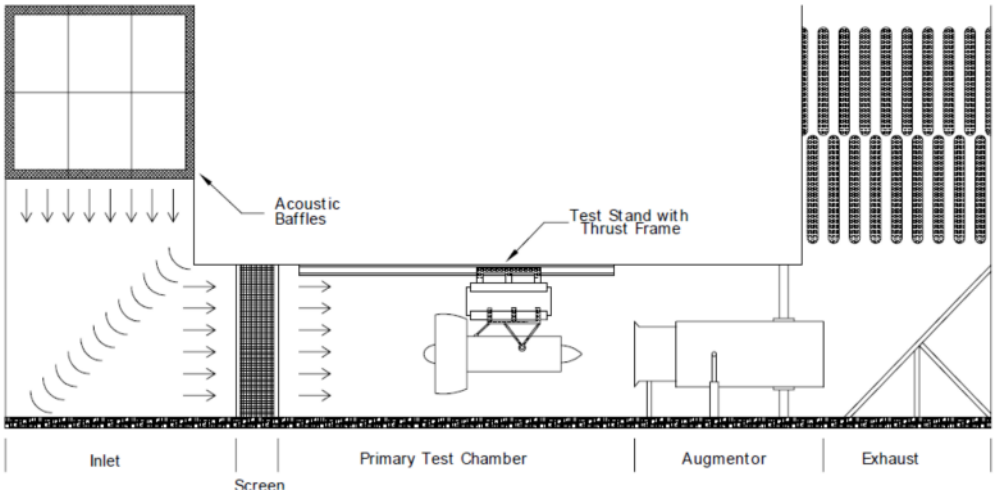

Figure 2.5 General design for an engine test cell with vertical intake (Federal Aviation Administration, 2002)

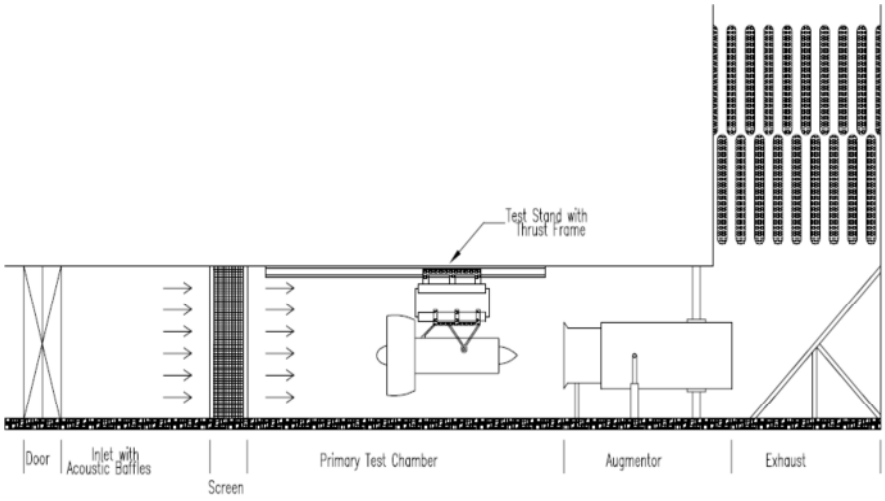

Figure 2.6 General design for an engine test cell with horizontal intake (Federal Aviation Administration, 2002)

Within the constraints of the site, to avoid wind shear effects in the intake region the orientation of the test cell should be such that the intake is aligned with the prevailing wind direction. This will minimize but not eliminate the problem. The vertical intake has been chosen for the new test bed currently being used by the manufacturer because recent advances in the design of flow splitters and straighteners have substantially reduced the adverse effects.

Wind effects and pressure losses across the inlet section could affect the engine performance and possibly damage engine components (SAE, 1976). The drop in total pressure across the inlet system could result in lower pressure inside the cell. An excessive depression in cell pressure could affect the air flow stability around the engine and accuracy of measurements, and might possibly cause structural problems. Jacques (Jacques, 1984) has recommended limiting the depression in cell pressure to a maximum of 150 mm H_2O. At this limit the engine will be working in conditions close to those of free air, with minimum corrections necessary during measurements and their correlations. At 150mm H_2O the test chamber structural load is highly unlikely to be a problem.

2.3.2. Debris Guard

To prevent large foreign objects such as leaves, from being drawn into the inlet, protective screens are usually incorporated at the entrance to the inlet. This problem is more important with horizontal inlets. Sizing of screens is a compromise: too small a mesh will produce an unacceptably high pressure loss, whilst too large a mesh will allow potentially damaging objects to pass into the test cell.

2.3.3. Flow Straighter

A vertical intake necessarily includes turning vanes to redirect vertical airflow to horizontal airflow into the test chamber, see Figure 2.5. These turning vanes always leave a wake in the airflow. These wakes are regions of lower pressure which not only contribute to the overall depression in cell pressure but also cause an increase in the overall turbulence level of the air entering the engine. The design of these vanes to minimise these adverse effects is a significant part of inlet design.

2.3.4. Sound Absorption

The silencer baffles are required to reduce engine noise emitted from the intake to acceptable levels add considerably to aerodynamic losses in the inlet region, because the restricted width of the channels necessary to produce sound attenuation introduces additional friction to the airflow.

The intake is acoustically lined in one to three rows of splitters. The needed noise attenuation quality is dependent on the thickness of the splitters and the distance

between them. The larger distance and thickness are used to attenuate low frequency noise whereas high frequency noise is best attenuated by small distance and thickness. Generally the dimensions of the silencer depend upon:

- The required total air mass flow
- The maximum cell depression
- The detailed design of the splitters.

Typically, sound absorbing material, when added to the inlet stack of a vertical inlet system, see Figure 2.5, is applied in and around the topmost section. The material used will usually be added in the form of a "sandwich" with sound absorbing fibrous material contained within two metal plates, one or both being perforated. These will usually be in the form of aerodynamic wedges in the flow and as a layer around the inside of the inlet duct. A similar arrangement will be applied to the inlet splitter panels in a horizontal intake.

2.3.5. Secondary Air Intake

Some test cells use two separate inlet systems, see Figure 2.7. One intake is for engine air flow and test chamber ventilation. The other intake supplies additional air for cooling the exhaust system. The same general principles and design criteria requirements apply to any second inlet as to a primary inlet. The major difference is that as the secondary inlet does not flow through the engine it does not have to be so aerodynamically clean. Noise attenuation is just as important as for the primary inlet but much less sophisticated flow straightening and splitting is necessary.

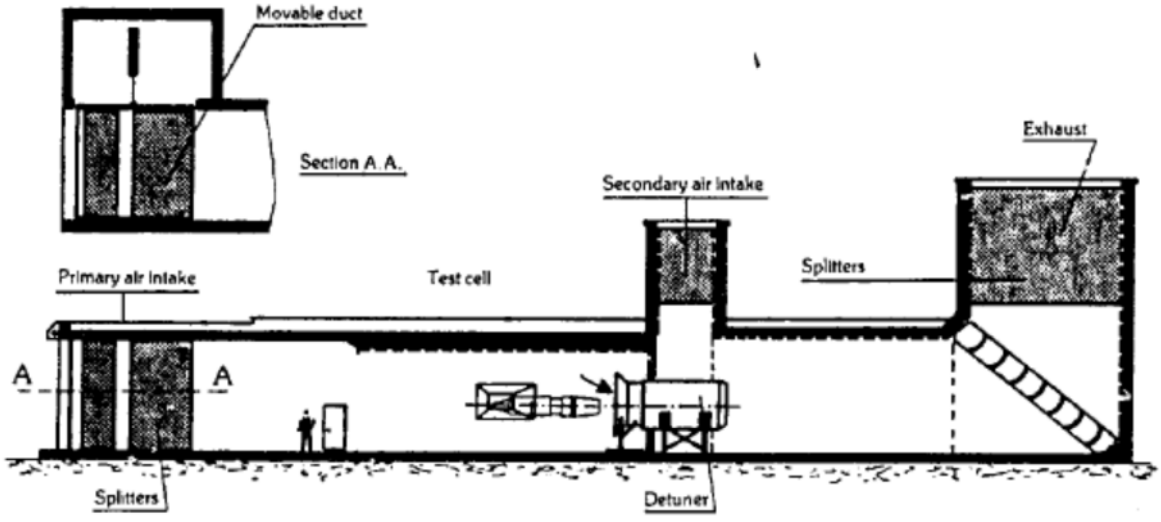

Figure 2.7 Engine Test Cell with two air intakes (Jacques, 1984)

A secondary air intake is rarely horizontal, it is usually positioned vertically above the engine, with its airflow directed into the augmentor or exhaust collector, see Figure 2.7. The need for a second inlet system is determined by the cooling requirements of the system and the maximum airflow permitted through the test chamber given the physical size of the chamber and of the engine power rating. Horizontal secondary intakes are often to the side or rearward facing, drawing in air from a different direction than any primary horizontal intake.

Over hot gas re-ingestion with a secondary intake is not of a great concern as the air supplied in this way does not pass through the engine. However it is still undesirable as it reduces the cooling effect if the gas is at a temperature higher than ambient.

It will be preferable to avoid a second inlet at the feasibility stage of the test cell construction or conversion due to the design complication described above. Nevertheless, given often very large change in mass flow rate between low and high engine power settings, the need for additional cooling in the test cell may demand a secondary inlet system. However, if a test cell has two intakes there are very real dangers of significant distortion in the flow patterns. Very careful monitoring of both air flow patterns and their interaction is necessary to ensure air from the secondary intake is not drawn forward into the engine intake. Alternatively, a secondary inlet allows a smaller test chamber to be used for larger engines than would otherwise be the case, so the expense of providing a secondary air inlet may prove to be cost effective. Adding a secondary inlet to an existing test cell is an option that could be preferred to constructing a new one, and make it possible for the upgraded cell to test engines of a new (more powerful) type.

Often a second intake is only used for high engine power settings or just for reheat running for engines with reheat, with the shutters on the intakes remaining closed for low power testing because at low power settings, sufficient air is drawn into the test chamber through main front air inlet to maintain adequate cell ventilation and through chamber air velocities to prevent hot exhaust gas recirculation into the engine inlet

Losses occurring in the intake region increase the cell pressure depression which should be kept to a minimum not only because of the structural load caused on the test

chamber walls but more importantly, because of the correction factor which must be applied to the measured engine performance parameters to normalise them to an open air test bed at sea level. These losses, and in practice there will always be some, cause a very slight temperature rise of the air stream. Test bed thrust correction factors (TCFs) are discussed in detail in section 2.12.

Cell pressure depression due to losses in the inlet system could be reduced if the width of the inlet stack was increased, this would decrease the speed of the air flow and reduce TCF. This would have the beneficial effects that reduction of the air speed through the sound absorbing regions would reduce noise regeneration and make the attenuation more effective. However the extra cost of larger intakes usually limits the optimum size of the design solution.

The quality of the airflow that the inlet system deliver to the engine intake is critical because of its effect on measured engine performance, this is even more true with new engines of higher by-pass ratio and lower fan pressure rise which require even less distortion in inlet flows.

Figure 2.8 Modern test chamber (Cenco.com)

2.4. TEST CHAMBER

The engine is positioned in the test chamber. Figure 2.8 shows a picture of a modern test chamber. Uniform and aerodynamically clean air enters the test chamber from the inlet plenum and it leaves the test chamber through the exhaust system, see Figure 2.4. In between, a proportion of the air will be drawn into the engine through a bellmouth air duct, and the remaining air will flow around the outside of the engine and leave the test chamber via the exhaust system. The engine exhaust gases emerge from the propulsion nozzle at high velocities and enter the exhaust region. The high velocity of the exhaust gases creates an ejector effect which entrains the secondary airflow passing around the engine and takes it out via the exhaust.

A perfect test chamber would contain nothing to cause airflow distortion. It would have frictionless surfaces and contain idealised air flows with no viscous effects and no vortex formation or exhaust gas re-ingestion. Frictionless flow is not possible, but careful design can prevent ingestion of exhaust gases and minimise vortex formation.

Rudnitski in an AGARD report (Rudnitski, 1990) discusses test chamber limitations on the size of engine to be tested. A significant part of his report was based on a relationship drawn from (SAE, 1976) between cross-sectional area of the test chamber, mass flow of air through the engine, and the air flow entrainment ratio (ratio of mass flow rate of secondary air past the engine to mass flow rate of primary air entering the engine).

Any thrust correction required will depend strongly on the secondary air speeds through the test chamber. To minimise the correction to be applied to measured values, these secondary air speeds should be kept as low as possible. Rudnitski (Rudnitski, 1990) concluded that test cell air velocities of less 10 m/s are necessary for an acceptably low correction factor.

Secondary air velocities cause uneven static pressure distributions along the length of the engine surfaces which give rise to unbalanced forces on the test frame and therefore on the measured thrust. The biggest effect is in the region of the engine nozzle exhaust because here the air velocities are highest as the air is drawn into the augmentor, see

Figure 2.5 and Figure 2.6. The higher these velocities the larger the required thrust correction. These problems are enhanced when the augmentor is positioned too close to the engine nozzle. The detailed effects and relationships are discussed later.

One consequence of high air velocities in the test cell is to lower the static pressure in the region in front of the augmentor nozzle into which the engine is exhausting. This is the same effect as flying the engine at a higher altitude than the actual altitude of the test plant, which means that the engine is with a forward speed.

2.4.1. Airmeter

In sea level test cells accurate measurement of air flow rate into the engine is usually achieved by attaching an air flow meter directly in front of the engine inlet as part of the test frame. The air flow meter will normally have a bellmouth measurement section with a protective debris guard. Only in altitude cells is the airmeter built into the air supply system and attached to the inlet duct work. In such circumstances a sliding joint is used to allow calculation of a thrust correction due to the unequal pressures on it; static pressure measurements are made locally.

2.4.2. TEST FRAME

The test frame supports the engine in the test chamber. To ensure the transmission paths for the thrust forces generated by the test engine during simulation follow as near as possible those experienced in flight, the test frame uses the same mountings that secure the engine into an aircraft.

As mentioned above, the test frame will have a small degree of axial movement so that the thrust generated by the engine can be measured by strain gauges. A hydraulic system is usually used to support the bearings and allow the desired axial movement. Frequent thrust calibrations ensure that the system is moving freely and not binding or sticking. The thrust frame will have an instrumentation panel mounted on it: for any flow, pressure, temperature or vibration signals that need monitoring.

2.5. Exhaust System

The exhaust system of a test cell has great effect on engine performance of a gas turbine because the exhaust system controls back pressure on the engine, and secondary airflow through the test chamber. The exhaust system is also important to reduce the noise emitted into the atmosphere from the test cell. The exhaust system typically consists of an augmentor or a detuner pipe, a diffuser section, a boot section, and an exhaust stack.

Adequate and efficient cooling is the most important single design criterion of the exhaust system. Emission temperature of a modern jet engine will be in the region of between 400ºC to 700ºC, possibly as high as 1800^{o}C if reheat is used. Acoustic absorbents used in exhaust systems have an upper temperature limit of around 400ºC (Jacques, 1984), so it is necessary to introduce a significant degree of cooling either using water cooling or by having a large secondary air flow.

The velocity of the gases in the exhaust, and thus the quantity of the secondary air flow, is controlled by the size of the augmentor tube. If the airflow through the test chamber is too low it could result in recirculation of exhaust gases, resulting in overheating and possible re-ingestion of combustion products by the engine, causing possible engine surge. A certain quantity of secondary air is required to reduce the mean flow velocity in the exhaust stack in order that the noise generated when the gases exhaust into the atmosphere is not too high. Too large a secondary air flow will generate a large static pressure gradient between engine inlet and nozzle exhaust; this will require a large TCF, which is undesirable. It is sensible to avoid both extremes of secondary air flow.

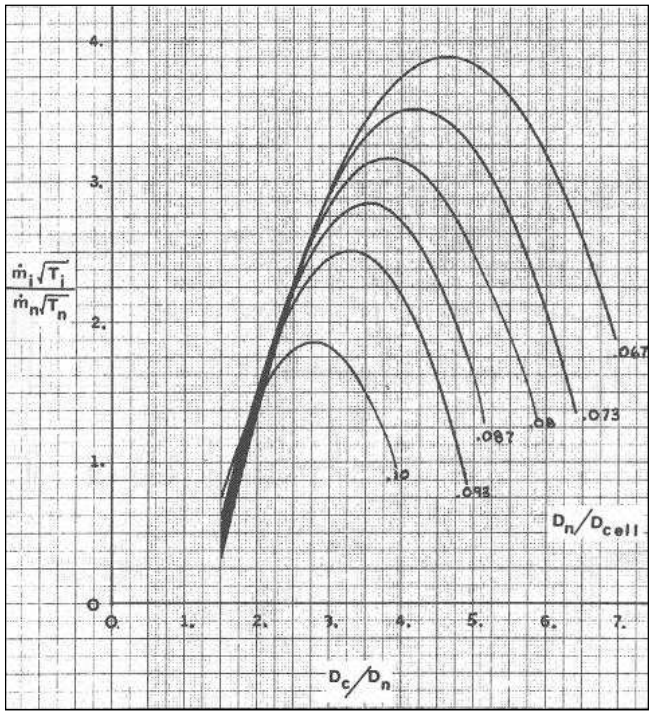

Figure 2.9 Nozzle and collector size effect on entrainment ratio (Hastings, 1983)

Hastings (Hastings, 1983) has shown that varying the ratio of engine nozzle diameter (D_n) to augmentor collector diameter (Dc) has a strong effect on secondary air flow, see Figure 2.9. He found that as the ratio of diameters decreased, the mass of air flowing around the engine to the mass of air flowing through it, also reduced. Hastings explained this as due to the smaller area available for secondary flow in the augmentor tube. Hastings tested 1/12 scale models, and Figure 2.9 shows some of his results. There is almost a linear variation between the entrainment ratio (in the vertical axis) with the diameter ratio (in the horizontal axis) before it drops off. Here spacing between nozzle tube and collector, and nozzle pressure ratio were held constant, and for a given engine nozzle and test cell of constant size, the collector diameter was varied. The entrainment ratio generally has the shape of an inverted parabola, rising to a maximum value, which is different for each nozzle to cell size ratio, before dropping again.

Kodres and Murphy (Kodres and G. L. Murphy, 1998) developed a CFD analysis, that considered three different detuner cross-sections: circular, square and rectangular. The square detuner showed the best aero-thermo-dynamics performance avoiding recirculation at the inlet and producing a lower surface temperature with an entrainment ratio a bit smaller than that of the circular detuner. However cross-sectional area of the

square detuner was about 27% greater than that of the circular detuner (diameter equal to the side of the square shape - R^2 vs $\pi R^2/4$). Noise, structural and cost considerations were not included and acknowledging these limitations it was concluded that maintenance costs could be reduced by changing from a round to an equivalent square detuner without any decrease in aero-thermal performance.

In a test cell, the linear distance between the engine nozzle and the augmentor tube, see Figure 2.5 and Figure 2.6, has a significant but smaller influence on secondary airflow but a substantial effect on static pressure ratio across the engine and thus on the TCF. As the distance increases, the blocking effect of the engine on the collector is reduced and there is an increase in the cell to engine airflow entrainment ratio on flow through the augmentor tube. Rudnitski (Rudnitski, 1984) and Sapp and Netzer (Sapp and Netzer, 1978) have also reported that with further increase in distance a second effect becomes dominant and the secondary airflow decreases. This effect is simply due to the spreading of the exhaust plume outside the augmentor tube leading to a reduction in the momentum flow into the augmentor tube.

Ideally the static pressure around the nozzle and the static pressure around the engine should be the same. In practice the distance gap is set and used for that engine and test plant configuration. The distance must be kept constant as any change will invalidate the TCF and thrust measurements.

Jacques (Jacques, 1984) gives a good explanation of the complex air flows that occur between nozzle and exhaust collector. Jacques recommends a minimum separation of engine nozzle and entry to collector of one engine nozzle diameter.

The relative positioning of gas turbine nozzle and collector tube entry must be correct because the initial portion of the collector is convergent so the secondary flow induced into the collector is accelerating and thus at a lowered pressure which feed back to influence the flow through the engine nozzle. This is expressed as friction and pressure forces, both of which act in the opposite sense to the measured engine thrust.

Having too small a separation distance of detuner and engine nozzle can cause feedback pumping within the test chamber. This is the phenomenon of very small cyclic variations in fuel and airflow growing with time. In an open test facility such small variations would decay naturally, but in an enclosed cell variations in engine exhaust jet

affect the secondary entrained airflow which feed into the engine inlet pressure. When the engine nozzle-augmentor entry separation is too short or the test chamber has a small cross-sectional area, pumping becomes so powerful that stable engine operation is impossible.

Having a large nozzle to exhauster distance increases noise produced in the test chamber. Rudnitski (Rudnitski, 1984) has suggested that as the high velocity engine exhaust mixes with the much lower velocity secondary airflow, the resulting shear forces generate flow instabilities such as vortices and eddies which dissipate their energy as noise. Increasing the separation increases the area of this shear layer area with more noise generation.

2.5.1. Exhaust Diffuser Section

The purposes of the exhaust diffuser sections are to recover as much static pressure as possible and to lower the exhaust stream velocity. This latter reduces the level of noise generated when the exhaust gases are ejected into the atmosphere. Site and cost constraints often limit the size of the diffuser fitted to a test cell, and often mean the diffuser design had to use an included angle greater than the optimum value of 7º for maximum pressure recovery. In such systems pressure recovery is achieved due to blockage effects of, e.g. bends in the exhaust duct, silencer baffles and cooling water injection rings. Such methods are very inefficient and not usually reliable or desirable.

2.5.2. Exhaust Boot Section

The boot section is that part of the exhaust system which turns horizontal flow into vertical flow for ejection into the atmosphere. The boot section thus has large forces exerted on it by the very hot and corrosive gas stream. Turning vanes are also used, to improve the transition in flow and to assimilate the forces into the structure in a more controlled manner.

The general conditions in the boot section are such that it is here that most corrosion and wear and tear takes place so inspection and maintenance access is essential. The forces exerted by the hot gas flows cause fatigue, especially of the turning vanes which are welded to the structure. An alternative to turning vanes is a perforated blast tube.

This is a tube sealed at its far end, with many holes along its length. The exhaust flow enters the open end and exits through the holes. Fatigue is also a major problem with the sound absorbing material which usually consists of a double sheet of metal.

2.5.3. Exhauster Cooling

The high temperatures of the exhaust gases necessitate cooling of the exhauster region of a test cell, particularly for military engines with reheat. There are two basic methods of exhauster cooling in use today: water cooling or air cooling. With water cooling, water droplets are sprayed into the exhauster where they evaporate into steam, absorbing heat energy and reducing gas temperature. The major advantage of water cooling is the relatively large value of the latent heat of evaporation which substantially reduces the quantity of secondary airflow required. In the latter case cooling is through the dilution effects of secondary airflow entering the exhauster ductwork with the engine efflux gases.

Jacques (Jacques, 1984)has calculated the mass of secondary airflow and water necessary to provide adequate cooling and has concluded that water cooling systems are only necessary for engines with reheat systems (military engines and some supersonic civil aircraft engines such as the Olympus 593 as used with Concorde). Jacques takes 400ºC as a guideline for the upper permissible limit for a fully mixed exhaust jet. This limit is derived from consideration of the properties of the acoustic panelling used in the exhaust duct (Jacques, 1984).

Assuming much the same value for the specific heat of air and engine exhaust gases it is a simple matter to calculate the relative mass flow rate of cooler air required in an air cooled system. For an engine exhaust temperature of 1760ºC, the typical flow of secondary cooling air is calculated to be at least 5.3:1 (5.3 is a high value because the initial 1760^{o}C is a high value). The calculated figure is given as a minimum value because the calculations assume complete mixing of the exhaust gases and secondary cooling airflow. This is an over-simplification because in real exhauster systems only partial mixing would be achieved. Thus the peak gas temperatures would be greater than the 400^{o}C upper limit unless extra cooling air was provided, increasing the dilution ratio to more than 5.3:1.

To reduce secondary cooling airflow required (which has to flow through the inlet plenum), there are two options: use water cooling or construct a secondary air inlet into the test chamber, downstream of the engine inlet to supply cooling air for the exhauster. The latter has already been discussed earlier in this section.

Using the same engine exhaust temperature of 1760ºC Jacques (Jacques, 1984)analysed the equivalent water cooled exhaust system. Using water cooling the entrainment ratio can be substantially reduced which means a smaller test cell can be used for a given engine and this is the major advantage of water cooled exhaust systems. However, against an air cooled system (even one using two air intakes) water cooling normally appears unattractive because of the complexity and cost of the extra services required and the additional long term maintenance expenses.

2.5.4. Exhaust Stack

The exhaust stack acts as a large chimney at the end of the exhaust ductwork, expelling diluted and cooled combustion gases into the atmosphere. The stack must be positioned so that gases leaving the exhaust stack are not drawn back into the test cell through the air intake.

The position of the exhaust stack must allow for prevailing winds and must not be upwind of the intake. Vertical intake stacks are at much higher risk of re-ingestion than horizontal intake and particular care must be exercised in determining its position. The requirement to have the exhaust stack downwind of the intake with reference to the prevailing direction is in contrary to the aim discussed above of not having a horizontal air intake facing into the prevailing wind direction in order to avoid too great a degree of inlet flow variation and distortion.

Exhaust stack of modern gas turbine test cells will normally be lined with acoustic absorbent material to reduce engine noise emissions. The cross-sectional area of the stack determines the velocity of the exhaust gases and a compromise must be reached between having as low a velocity as possible to minimize aerodynamic noise generation pollution within the silencer while having a sufficiently high velocity to carry the exhaust gases into the atmosphere avoiding local pollution and allowing dilution and dispersal of the flue gases. However, Jaques (Jacques, 1984) has prescribed the

maximum exhaust stack flue velocity to be limited at 30- 40 m/s to avoid excessive noise generation. Accordingly, this would determine the cross-sectional area of the stack.

2.6. Vortex Formation

With test cell of gas turbines, vortices can lift debris from the ground which may enter intake and cause compressor blade damage or vibrations which reduce the compressor surge margin. The inlet vortices that are form under certain conditions are can then ingested into the gas turbine engine. This can result in an engine surge event and prevent useful testing from being conducted. In some cases this can even result in compressor blade damage. Thus one aim of test chamber design is to avoid vortex formation as vortex ingestion into a running engine causes unstable engine operation, incorrect measurements and can cause engine compressor damage if the airflow distortions become severe enough

The wider the range of engines used in a given test cell the greater the probability of flow distortion, because inlet design and cell entrainment ratios suitable for one engine may lead to ingestion and vortex formation and ingestion with another of significantly different size. The test cell airflow will accelerate as it approaches the mouth of the inlet duct to the engine, but the cross-section of the airflow entering the engine at high power will have smaller cross sectional area than of the test cell. This accelerating flow and enlarging of the duct area result in flow separation at the test bed walls with potential vortex formation. All instrumentation and equipment used in the test cell will have some effect on the air flow as it passes, but with good design this should be a minimal effect.

Rodert and Garrett (Rodert and F. B. Garrett, 1955) reported a study of vortex formation with an axial flow jet engine mounted on a cargo airplane wing. A flat, horizontal platform was positioned beneath the engine, this could be moved vertically up and down and provided a surface on which vortices could form. With the engine at full power and a “wind” blowing from the rear with a velocity between 5.4 m/s and 7.6 m/s vortices were seen to form. The height of the engine above the platform was 2 m. With the engine running at 80% power and with a side “wind”, vortices were first observed when the “wind” speed was about 2 m/s. Again with the engine running at 80% power and with a head “wind”, vortices were observed when the “wind” speed

was between about 4.5 m/s to 6.7 m/s; here the floor was 135 cm below the inlet. It was found that even with engine power was decreased to just 30%, with low head "winds" of 0.5 to 0.7 m/s low energy vortices did form. They concluded that vortex formation depends on engine speed, its height above the floor and wind speed (air flow velocity), and that vortices can form independent of ambient wind direction. Air is drawn into the inlet from all directions and a region is produced beneath the engine where the different velocity components cancel, creating a stagnation streamline which is the only streamline along which a vortex may form and originates at the stagnation point which is absolutely fundamental for vortex formation**.**

Freuler and Dickman (Freuler and Dickman, 1982) tested the aerodynamic performance for a jet engine test cell and found that projections into the fluid flow at the inlet of the cell will distort the flow, possibly cause distortion of the fan air flow and so enhance vortex formation. This latter may cause core engine stalling and prevent useful tests. Engine ingested vortices can also be formed if the test cell entrainment ratio is inadequate.

Ho (Wei Hua, 2009) in his CFD modelling of vortex formation, focused on the formation of single cored vortices in engine inlets in a headwind. His results demonstrated that to avoid the formation of vortices a cell by-pass ratio (CBR) of more than 90% was necessary. Ho described CBR as:

$$CBR = 100\%\left(\frac{m^{\bullet}_{cell} - m^{\bullet}_{engine}}{m^{\bullet}_{engine}}\right) \qquad \textbf{2.1)}$$

Where; $m^{\bullet}_{cell}$ is the air mass flow rate at the cell intake and

$m^{\bullet}_{engine}$ is the air mass flow rate through the engine (both fan and core).

This work confirmed the commonly accepted industry view that to avoid vortex formation, a test cell must have a CBR of more than 80%. Test cells are now designed with CBRs of up to 100%, and even exceeding 200%.

Kromor and Dietrich (Kromer and Dietrich, 1985) have studied airflow patterns in test cells and have generated a computer model to predict vortex formation and other

potential problems. They have compared the results obtained from this model with experimental results they obtained at the General Electric Company. They have come to much the same conclusion as Ho (Wei Hua, 2009): that if the air flow in a test cell has a velocity ratio less than 0.5 (ratio of secondary airflow velocity within the cell to inlet velocity at front of cell) then vortex formation is likely.

The problem is worse at low entrainment ratios which is ratio of secondary airflow moves around the engine to the engine throat airflow because under this condition the point at which flow separates from the cell walls is further upstream, making vortex ingestion into the engine intake more likely. This problem can be reduced or even eliminated if diffusion along the test chamber walls by decreasing the cross-sectional area and accelerating the air flow up to the plane of the bellmouth intake.

Uniform air flow entering the test cell with a sufficiently large entrainment ratio will provide undistorted air flow into the engine inlet and prevent formation of intake vortices. Nakayama and Jones, (Nakayama and Jones, 1996) described vortex formation in terms of engine centreline height (H_c) and the engine throat diameter (D_i) as:

$$\frac{A_0}{A_1} = 24\frac{H_c}{D_i} - 17 \qquad \textbf{2.2)}$$

Freuler and Dickman (Freuler and Dickman, 1982) ran test cell modelling of a 1/17 scale plexiglass test cell models for 26x26, 20x26, and 20x20 square foot, see Figure 2.10. Figure 2.10 shows vortex formation as a function of test cell by-pass ratio and velocity ratio. It can be seen at once that no vortices are present for a velocity ratio greater than about 0.5, nor for test cell entrainment ratios of more than about 0.75 for the three cross-sectional ducts used. It is significant that, according to Nakayama and Jones (Nakayama and Jones, 1996), for no inlet vortices to be formed in a test cell with a front cell velocity distortion factor greater than 0.2 (which is considered low), the minimum entrainment ratio must be greater than 0.75.

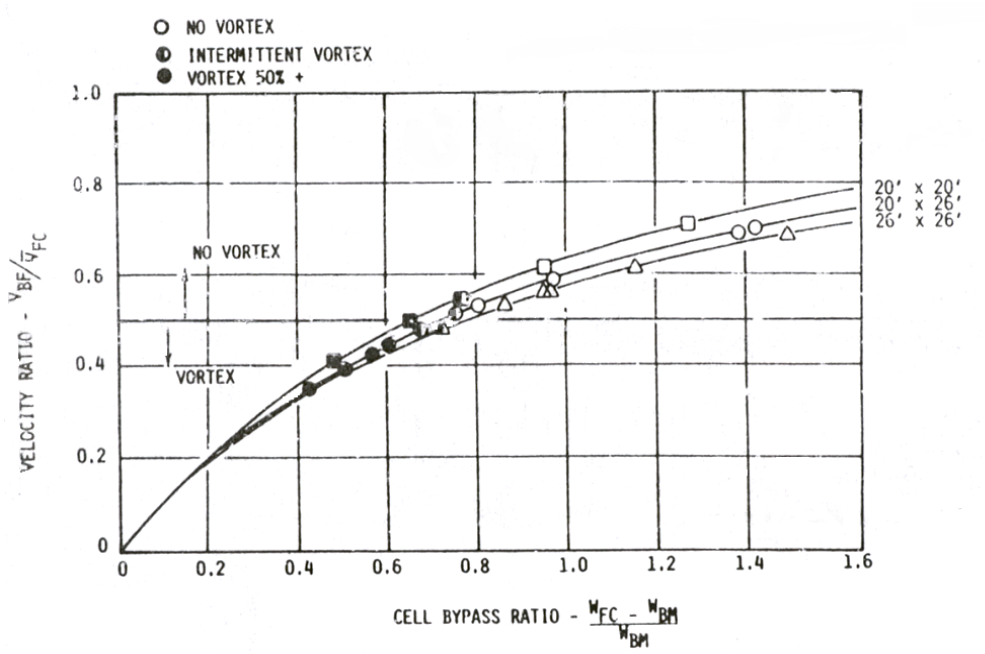

Figure 2.10 Vortex formation as a function of velocity ratio versus cell by-pass Ratio (Freuler and Dickman, 1982)

Freuler and Dickman (Freuler and Dickman, 1982) found that the 26x26 test model showed acceptable cell aerodynamics with an entrainment ratio greater than 1 and without intake vortices being formed under a velocity distortion level substantially less than current engine test cells where levels of 0.5 or higher are common .

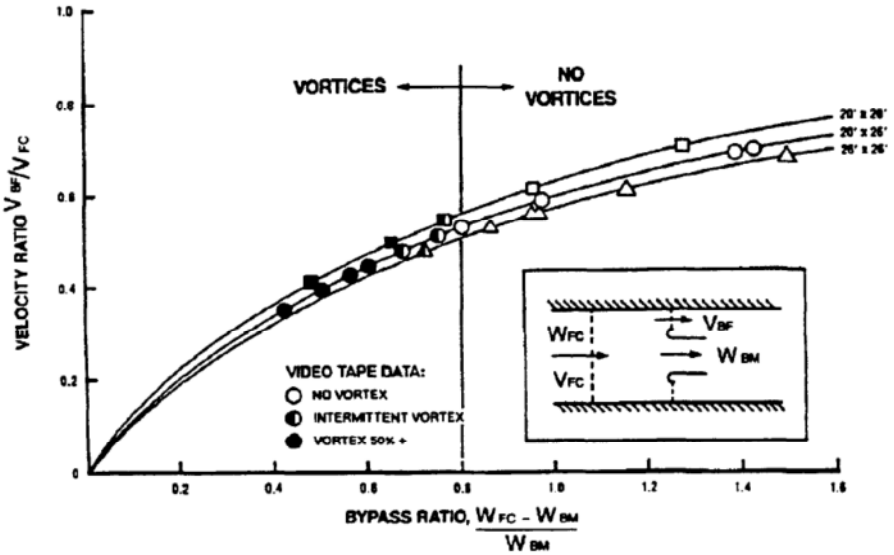

Figure 2.11 Bellmouth-ingested vortex formation (Freuler and Dickman, 1982)

By an experimental analysis involving scale models of large turbofan Freuler (Freuler, 1993) used flow visualization techniques to determine V_{BF}/ V_{FC}, as a function of

entrainment ratio. The results are shown in Figure 2.11 where it can be seen that vortex formation and ingestion take place at velocity ratios of 0.5 or less. Figure 2.11 also have a schematic which defines the used velocity notations.

2.7. Flow Distortion

Factors affecting the probability of flow distortion: e.g. when using a test cell designed for one engine with a different engine; projections into the flow causing distortion in the flow into the engine fan face; and the separation between down-stream air-straighteners, inside the cell inlet stack and the engine inlet, have all been found to influence the quality of the air flow and have been mentioned above (Jacques, 1984).

Karamanlis (Karamanlis et al., 1986) has defined a velocity distortion factor, V_0 as:

$$V_o = \frac{V_{max} - V_{min}}{V_{avg}} \qquad \textbf{2.3)}$$

where, V_{max}: maximum velocity at cell front,
V_{min}: minimum velocity at cell front, and
V_{avg}: average velocity at cell front.

Air velocity in the test cell affects the static pressure along the length of the engine. Velocity of the secondary flow, if high enough, can produce a change in the static pressure which require the use of a TCF. It has been suggested that this velocity should not exceed 10 m/s, but its value will be affected by cell aspect ratios and entrainment (SAE, 1976).

Jaques (Jacques, 1984) has made public the rule used by the General Electric Company to assess the acceptability of flow distortions down-stream of the cell inlet: The recommended difference between maximum value and any fluctuation should be 25 mm H_2O or less; a difference of greater than 50 mm H_2O from the average value is unacceptable.

Civilian aircraft commonly use thrust reversers on landing. These devices minimise landing distances and reduce runway lengths. Thrust reversers are mechanical devices which are used to re-direct engine thrust forward to assist braking. However, when used

in a test cell they become a source of major flow distortion; directing a large proportion of the engine exhaust gases towards the engine intake. But hot gas re-ingestion must be avoided so large deflector plates are used to deflect the gases back down the test cell. Thermocouples are usually fitted to the debris guard on the engine bellmouth because a temperature rise is taken as proof of hot exhaust gases being re-ingested into the engine.

Freuler (Freuler, 1993) suggested internal structural modification to the cell to improve the flow quality. He had found that the shape of the monorail which extended down from the ceiling in the front region of the cell, and carried the engine, could cause flow instability around the bellmouth. It was found that close to the monorail there was separation and some consequent recirculation. Aero-dynamics fairings were suggested as solution.

Temperature fluctuation at the compressor entry can seriously affect engine performance and make it very difficult to obtain meaningful correlations between the different parameters being measured and so should be avoided. Temperature distortion due to flow recirculation can also occur in the test bay, as will be explained later.

2.8. Wall-Flow Separation

Separation of the flow from the walls impacts negatively on the quality of the flow inside the cell and engine performance. Wall separation takes place as the air, which initially flows through a larger cross-sectional area than that of the engine, accelerates into the bellmouth to enter the engine.

Due to the geometry difficulty and complexity of the test cell, Kromer and Dietrich (Kromer-Oehler et al., 1984) used a computational approach for the test cell flow quality. The model introduced the test cell inlet flow distortion as non axial velocity and assumed that only a static distortion is applied where the inlet pressure loss is ignored.

The pressure coefficient with respect to the normalized axial station as seen in Figure 2.12 . The position of the highlighted area of the engine bellmouth is represented by the solid line which is normal to the horizontal axis. The predicted position of the separation area is represented by the dashed line whereas the experimental data is

represented by rounds. The pressure coefficient is negative far upstream the bellmouth at the entry of the test cell due to the wall contraction. The flow shows a diffusion in the pre-entry stream tube just upstream the bellmouth where a suction in expected. Vortex formation takes place when the flow separation is upstream the highlighted area on the bellmouth.

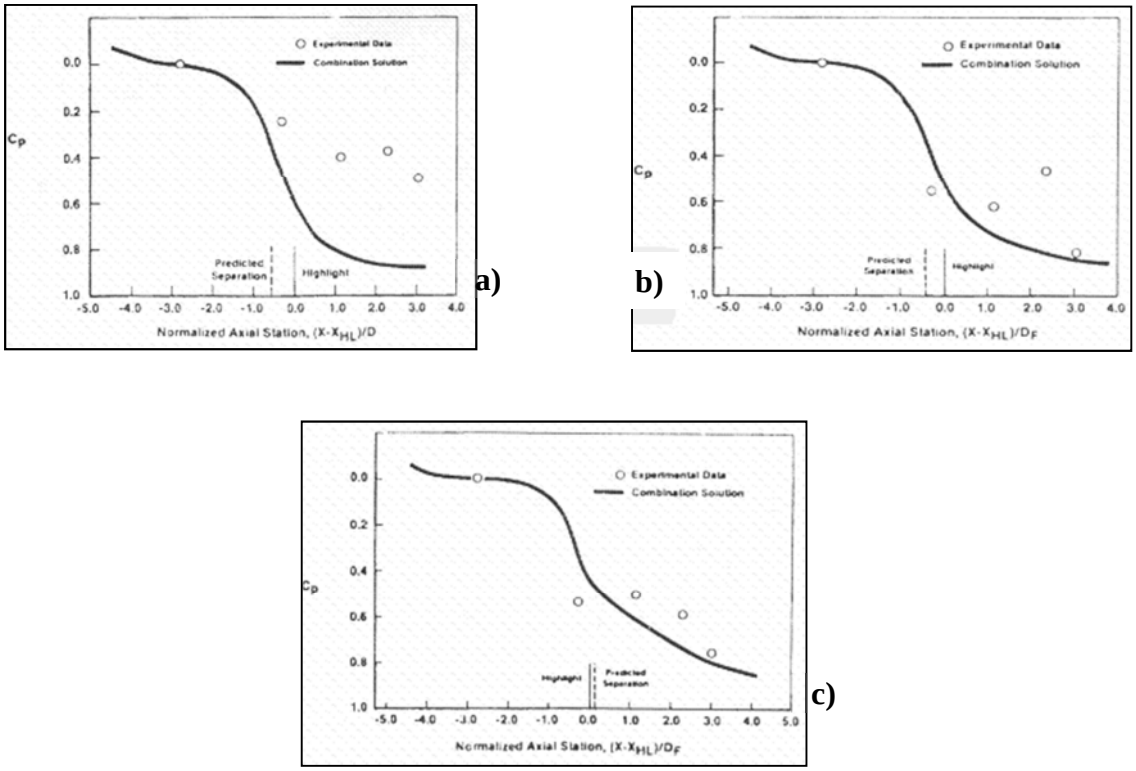

Figure 2.12 Axial variation of C_p on the sidewall of the test cell of a) μ=0.72, b) μ=0.86, and c) μ=1.15 (Kromer-Oehler et al., 1984)

Kromer and Dietrich, (Kromer-Oehler et al., 1984) claimed that the flow separation from the walls can occur at any entrainment ratio. Figure 2.12 shows the location of the wall-flow separation in a test cell for 3 different by-pass ratios. With increase in entrainment ratio, the position at which separation occurs moves downstream. Vortex formation could be prevented if the separation point occurs downstream the highlight.

The airflow in the test chamber, as it approaches the plane of the bellmouth of the engine inlet duct, is accelerating because the flow entering the engine has a cross sectional area smaller than that of the inlet ducting. This acceleration can cause flow to separate from the test cell walls, floor or ceiling with the potential for vortex formation. The position at which the cell wall boundary layer separation occurs will depend on the entertainment ratio of the test cell secondary air flow and as this ratio increases, i.e. a

greater proportion of the total air flow passes along the outside of the engine, the position of separation moves downstream towards the nozzle exit. With a sufficiently high value of the entrainment ratio, the separation point will move downstream past the bellmouth entry, so that any vortices generated by separation can not be ingested into the engine.

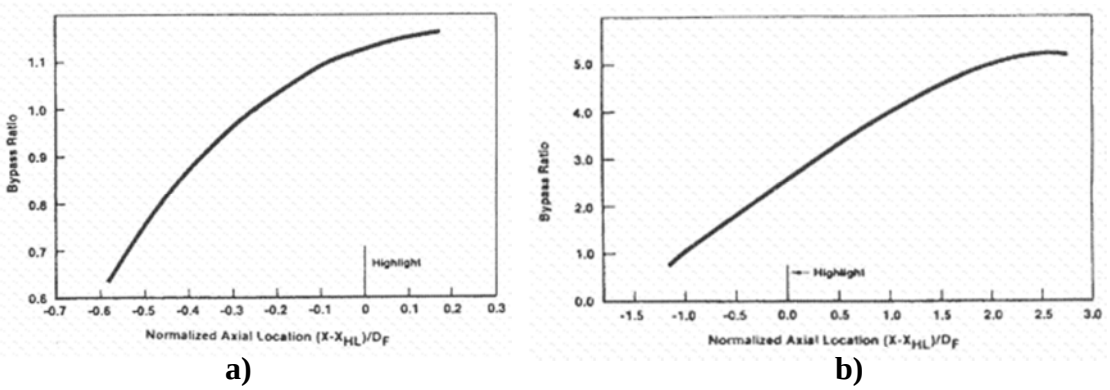

Figure 2.13 Predicted wall separation a) large turbofan and b) small engine

(Kromer-Oehler et al., 1984)

Figure 2.13 compares the predicted location of the flow separation for a small engine and a large turbofan with cell entrainment ratio. These curves are the location of the predicted flow separation as function of the cell entrainment ratio. The vortex formation can be avoided only if the separation occur downstream the bellmouth highlight section. It can be seen that separation occurs for by-pass ratio < 2.6 for the small engine and by-pass ration < 1.1 for the large engine. Thus, for bypass ratios larger than these and entrainment ratios > 0.75, there is little likelihood of vortex formation and ingestion(Kromer-Oehler et al., 1984).

2.9. Recirculation

External recirculation is where hot gases from the exhaust stack enter the intake and are re-ingested. The likelihood of this happening should be minimised at the design stage. Horizontal intakes reduce recirculation but it is occasionally unavoidable if the wind is strong enough.

Internal recirculation takes place when excess back pressure occurs in the detuner or the exhaust stack. Back pressure can be caused due to the presence of exhaust system components such as, bars or rods, diffusers, and water injection rings. At the design

stage these components should be positioned to allow a free flow of air to minimise pressure loss.

Hot gas recirculation can affect flow measurements made inside the cell and the re-ingestion can alter the engine performance. Such recirculation can be seriously disadvantageous even without re-ingestion; it can generate temperature gradients in the flow up-stream of the engine the performance of which is badly affected by such temperature distortions (Rudnitski, 1990).

Jacques (Jacques, 1984) has pointed out that internal recirculation of hot air will affect the structure of the test cell, its instrumentation and wiring. There will be a consequential effect on thrust measurements. Placing an obstruction in the flow path – e.g. the cradle holding the engine - can cause some recirculation and produce flow instabilities into the engine inlet. If the secondary mass flow rate is so small that the pressure at the rear of the engine is greater than that at the front, hot gas re-ingestion is likely to occur. In some cases this might cause compressor surge so it is necessary to ensure adequate secondary air flow.

The thrust reversers used when testing high by-pass engines can induce exhaust gas recirculation. Flow distortion can be avoided if catchers are used to turn the reversed flow back into the detuner so that measurements remain reliable.

The design of the test cell should be such as to eliminate or minimize any projections into the flow entering the engine, or any aspect which affects airflow in the vicinity of the engine, to ensure that there is no air recirculation.

Because flow recirculation can affect the pressure distribution along the engine it can also affect thrust determination.

2.10. Cell Depression

The static pressure measured in the test cell will obviously be less than that measured outdoors, this difference is the cell depression. SAE (SAE E-33, 1985) define cell depression as the difference between the ambient pressure and the static pressure in the

test cell chamber. Most designs result in a cell depression of about 50 to 100 mm H_20, and Jacques (Jacques, 1984) has recommended a maximum limit of 150 mm H_2O.

The cell depression is a measure of the total pressure loss along the path of the incoming air flow. Excessive cell depression can, occasionally, be a cause of structural problems, it is much more likely that it would affect the stability of the air flow around the engine and the accuracy of measurements. The Jacques (Jacques, 1984) limit of 150 mm of H_2O is primarily to allow the engine to work in conditions close to free air and to minimise any corrections necessary to measurements.

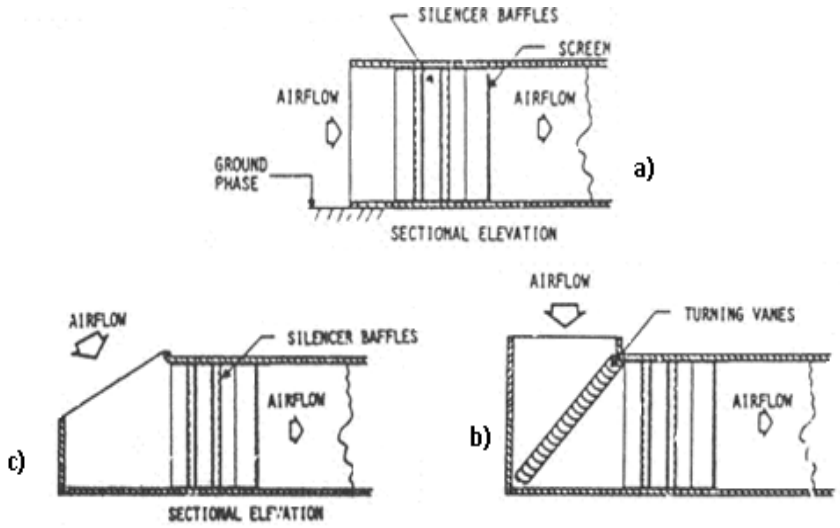

Figure 2.14 Inlet plenum: a) horizontal, b) vertical, c)vertical truncated (Freuler and Dickman, 1982)

Freuler (Freuler and Dickman, 1982) studied three scale model test cells with different inlet plenum configurations subject to different crosswinds: horizontal straight, vertical 90º with turning vanes and a vertical truncated version, see Figure 2.14.

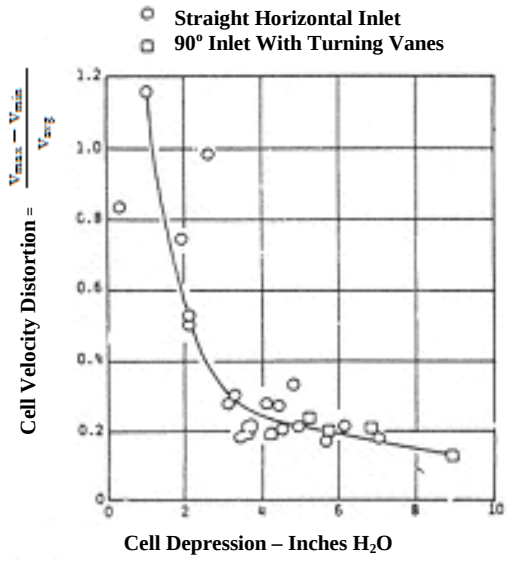

Figure 2.15 Cell depression for different cell inlet configurations

(Freuler and Dickman, 1982)

As would be expected the study found that a horizontal inlet without flow screen or baffles gave the lowest cell depression, but simultaneously produced the highest flow distortion. The results of the study are shown in Figure 2.15 and it can be seen that more uniform flow (lower flow distortion) is produced by higher loss flow screens, but these produce a higher cell depression. Figure 2.15 also shows that low inlet flow distortion of 0.2 or less results when the selected flow screens or baffles produce a cell depression of more than 75 mm inches of water. Thus, in practice a compromise between cell depression and flow distortion is required.

2.11. Entrainment Ratio and Ejector Pump Effect

The exhaust system of the test cell includes a detuner which collects engine exhaust gases and secondary air and ejects them to atmosphere as shown in Figure 2.16. High energy exhaust gases flow at high velocity while the secondary airflow has low energy and velocity. The mixing and interaction between these two airflows at the entrance to the detuner produce an ejector pump effect which is both important and quite complex. However, the ejector effect will have an effect on the pressure at the engine inlet possibly altering its performance (Jacques, 1984).

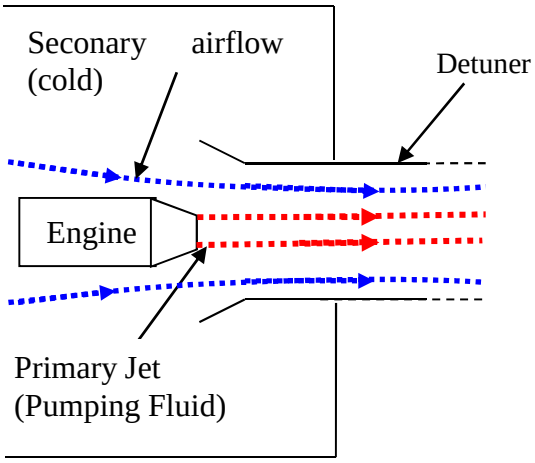

Figure 2.16 Jet pump action between the engine and detuner

The mixing of the two streams reduces the temperature and velocity of the primary flow which are critical factors in the reduction of both cell cost and noise pollution. The noise of a jet of air is directly related to the velocity of the jet hence reducing the velocity of the jet will reduce noise pollution generated by the test cell. The reduction of exhaust jet temperature reduces the need for complex designs and use of heat resistant materials in the exhaust system, thus reducing cost (and size) of the test cell.

The better mixed the primary and secondary flows when exhausting to atmosphere, the lower will be peak exhaust temperature and noise. To achieve a fully mixed flow in a simple cylindrical detuner would require an excessively long detuner, and thus a 'blast basket' is used to enhance mixing and reduce length. A blast basket is simply a cylinder with thousands of holes drilled into it, see Figure 2.17. Blast baskets also redirect the flow from horizontal to vertical ejection through a stack. The final exhausted mass flow is fully mixed, low velocity, low temperature flow. Large test facilities use vertical exhaust stacks to reduce the size of the facility and to reduce the noise and thermal pollution around the building.

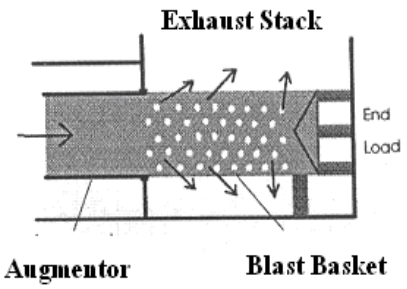

Figure 2.17 Schematic of a blast basket (Anas, 1995)

The energy density of the primary flow decreases and that of the secondary flow increases until they balance, and at this point the fluids are fully mixed. The increase in energy of the secondary flow is later converted to an increase in static pressure using a diffuser. An important consequence of this pumping effect is possible oscillations in engine in fuel and air flows.

There will be a low pressure region at the entry to the detuner just at the engine nozzle. This low pressure region causes secondary air to be entrained into the test cell: a small mass flow of high energy gases induces a larger quantity of slower moving secondary air. The entrainment ratio is defined as the secondary to primary air mass flow as in the following equation:

$$\mu = \frac{W_s}{W_p} \qquad \textbf{2.4)}$$

where μ is the entrainment ratio

W_s : is the secondary air mass flow, and

W_p : is the primary air mass flow

Walsh and Fletcher (Walsh and Fletcher, 1998) mention that the entrainment ratio may be calculated from measured temperatures and a simple enthalpy balance using:

$$\mu = \frac{W_{air}}{W_{gas}} \approx \frac{H_{gas} - H_{mix}}{H_{mix} - H_{air}} \qquad \textbf{2.5)}$$

where H is enthalpy based on temperature and fuel air and temperatures must be measured values.

Although the secondary flow is essential it interacts with the engine and its supporting equipment causing some thrust measurement error. It also distorts to some extent most of the flow phenomena in the cell through flow recirculation, vortex formation and cell depression. The secondary flow entering the cell is responsible for uncertainty in measurement, for thrust correction factors, for noise emission and possibly for stability of the engine, but it is essential for cooling the engine and exhaust system and reducing emission noise.

The entrainment ratio is influenced by the separation of engine nozzle and detuner, ratio of the diameters of the nozzle and detuner and primary flow pressure and temperature. These effects are discussed in the following sections.

2.11.1. Effect of Engine-Detuner Separation Distance

Studies of the effect of the separation of a real engine nozzle and detuner is both complicated and very expensive. Thus most of the relevant research work in the literature is on scaled-down test facilities.

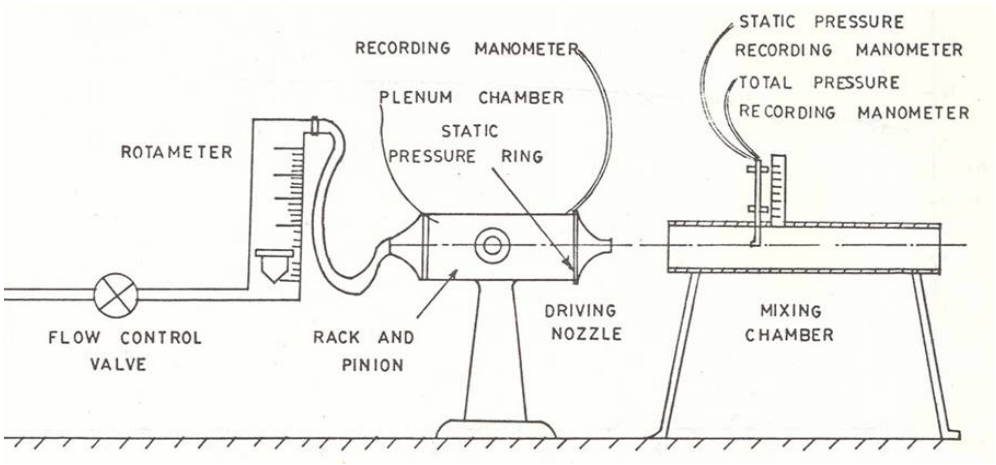

Figure 2.18 : Experimental arrangement used by Vyas and Kar (Vyas and Kar, 1975)

Vyas and Kar (Vyas and Kar, 1975) have conducted an experimental study to investigate the effect of driving nozzle to detuner distances and the nozzle to detuner area ratios as well as other parameters. Their experimental arrangement is shown in Figure 2.18. The detuner diameter was 38 mm and the nozzle diameters were 2 mm, 3 mm, 4 mm and 5 mm. These experiments found that the entrainment ratio decreases with the nozzle-mixing pipe (detuner) distance. This appears to contradict the results of others, as described later. The first observation is that the nozzles being tested had very small diameters compared to the detuner, so the blockage area is very small at the inlet of the detuner, and doesn't affect the ejector performance.

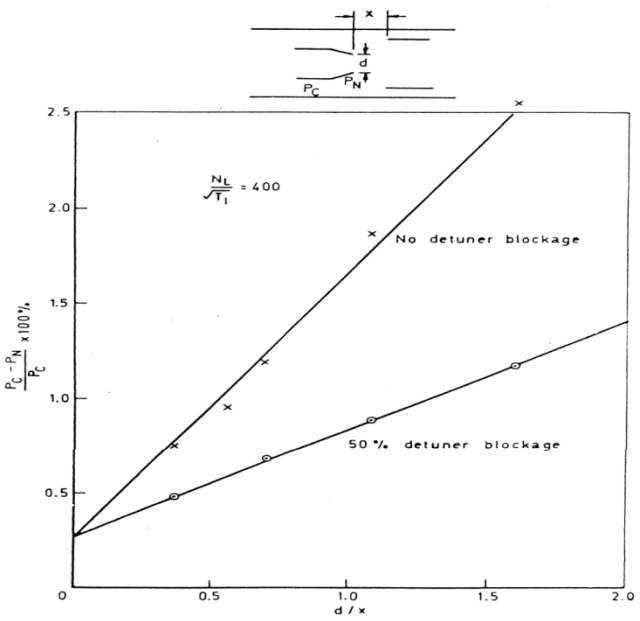

Figure 2.19 Effect of detuner gap and blockage on nozzle depression (Ashwood, 1984)

(The vertical axis is the % depression around the engine nozzle and d/x on the horizontal axis is the ratio of nozzle diameter to engine to detuner distance)

Ashwood (Ashwood, 1984) investigated the effect of the blockage area of the engine nozzle on the ejector performance and consequently on the amount entrained air mass flow. Figure 2.19 shows the effect of the blockage area at the entrance of the detuner. It shows the percentage depression of pressure around the engine nozzle with change in the horizontal separation of engine and detuner. The depression is key factor controlling the amount of induced secondary airflow into the test cell. It shows that the depression without blockage area is much higher than with 50% blockage area.

This result shows the relation between the engine-detuner distance on the pressure distribution around the engine and in the test cell. The closer the engine to the detuner the higher the pressure depression around the nozzle.

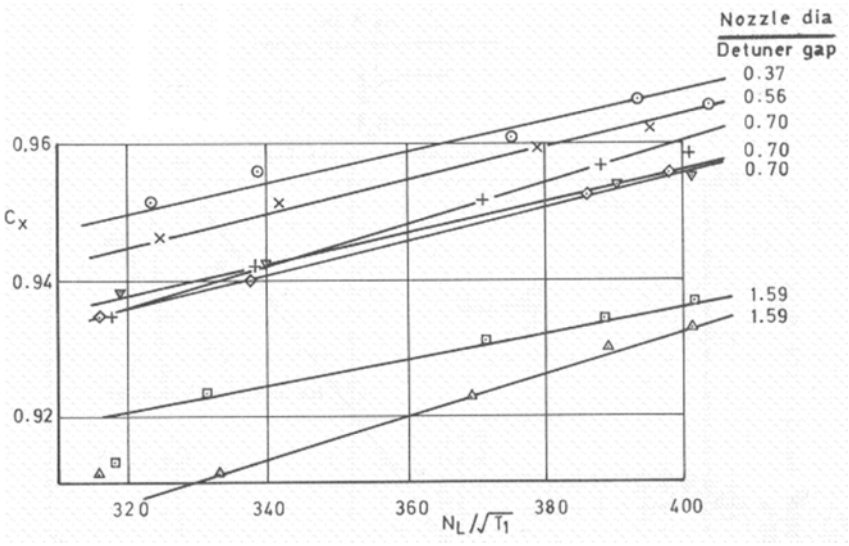

Figure 2.20 Engine-Detuner gap effect on the Measured Thrust (Ashwood, 1984)

(C_x on the vertical axes is the ratio of measured to calculated thrust, and horizontal axis represents the engine non-dimensional rotational speed)

Ashwood (Ashwood, 1984) also conducted experimental work to study the effect of the separation of engine and detuner on the measured thrust. Figure 2.20 shows the ratio of measured to calculated thrust over a wide range of engine non-dimensional rotational speed. The engine-detuner separation was changed for a fixed engine nozzle diameter and the results are shown in Figure 2.20. The difference between the measured and calculated thrust decreased as the engine to detuner distance increased. The results proved the effect of the engine and detuner separation distance on the thrust measurements.

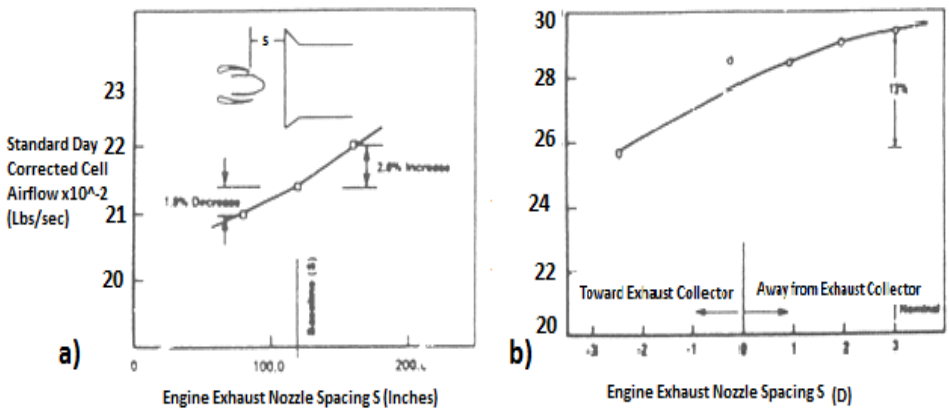

Figure 2.21 Effect of the Engine-Detuner Distance on the Entrainment Ratio for a) Large Turbofan, and b) Military Engines (Karamanlis et al., 1986)

Karamanlis et al., (Karamanlis et al., 1986) conducted a series of model and full-scale experiments at the GE Strother turbofan/turbojet test facility. They used two ejector powered engine simulator EPES units to simulate commercial and military engines. The engine simulator utilizes the ejector action of a high pressure air jet submerged in the model to pump the flow captured by the inlet under appropriate conditions, representative of a turbine engine exhaust. The objective of the work was to determine the amount of cooling air required to cool down the hot section of the military engine and to show that a single test cell configuration will satisfy both the commercial and the military gas turbine engine/test cell performance requirements.

Figure 2.21 shows the effect of moving the engine with respect to exhaust collector entry for both the commercial and the military gas turbine. The large turbofan on the left of Figure 2.21 shows that moving the engine 101cm (40inches) closer to the exhaust collector, the cell airflow is decreased by 1.8% and by moving the engine 101cm away from the exhaust collector, the cell airflow increases by 2.6%. The effects on the military engine are shown on the Figure 2.21(b). By moving the engine nozzle inside the exhaust collector, pumping can be reduced to 12%. This may be necessary in some cases to avoid noise problems.

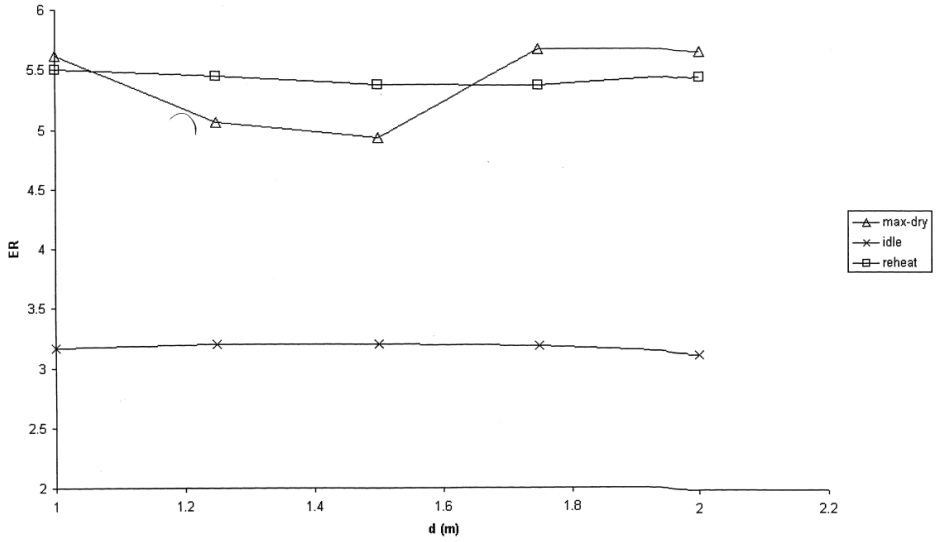

Figure 2.22 Entrainment variation with engine-detuner distance d (m) (Franco, 2000)

A 2-D CFD simulation was conducted by Franco (Franco, 2000) at Cranfield University. Different engine power settings (idle, max-dry and reheat) and different engine-detuner distances were investigated. Figure 2.22 shows that for an initial

separation of 1d (d is engine nozzle diameter), entrainment ratio does not change for either idle and reheat engine conditions with further increase in engine-detuner separation. However, for max-dry conditions the entrainment ratio decreases with further engine-detuner separation and then starts to increase.

Gullia (Gullia et al., 2005) conducted a comparison between experimental results and computational analysis for the entrainment ratio over with the engine nozzle position from detuner entry as shown in Figure 2.23. although the magnitude of the two results were different the general trends were the same. The entrainment ratio increased as the engine moved away from the detuner for about four engine nozzle diameters then remained constant.

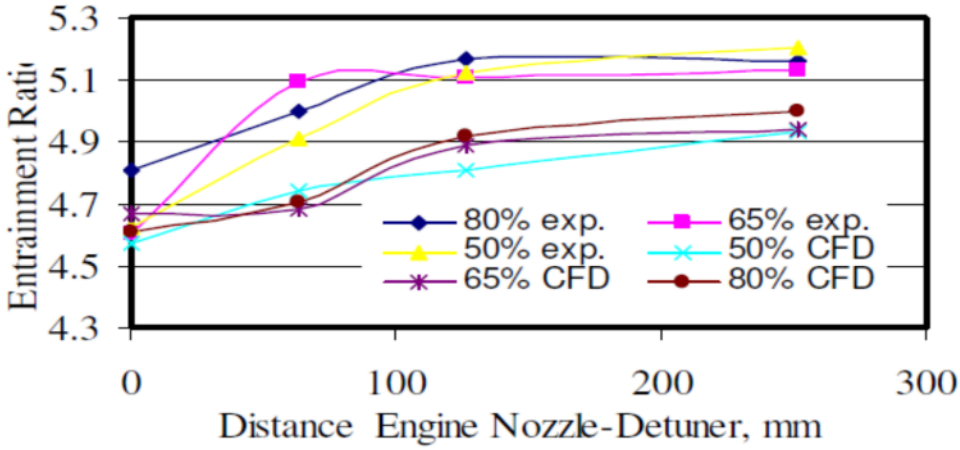

Figure 2.23 Experimental and CFD comparison (Gullia et al., 2005)

In summary these results are mutually compatible: increasing the engine and detuner separation distance gives an initial increase in entrainment and then a levelling off .

2.11.2. Effect of Detuner:Nozzle Diameter Ratio

The ratio of detuner to engine nozzle diameter ratio influences the entrainment ratio. This ratio defines the area available for the secondary airflow to be induced into the detuner.

Walsh and Fletcher, (Walsh and Fletcher, 1998) gave key guidelines for the design of an indoor test cell to avoid undesirable flow phenomena and to minimise measured thrust deficiency. One of these guidelines is to have a detuner diameter of around three times the engine nozzle diameter (area ratio 9:1). Increasing this ratio should increase

the entrained flow. Hastings (Hastings, 1983) conducted an interesting study using 1/12 scale models on the effect of varying the diameter ratio. The results show that the entrainment ratio decreases as the diameter ratio decreases. Hastings considered this as an effect of having a smaller area available at the detuner for secondary airflow. Vyas and Kar, (Vyas and Kar, 1975) in their experimental work also studied the influence of detuner to engine nozzle area ratio and found that by increasing the diameter ratio of detuner to the nozzle, the entrainment ratio increases.

Using the available experimental data Vyas and Kar (Vyas and Kar, 1975) found an empirical relationship as follows for the entrainment factor :

$$\mu = 0.22\frac{D_{\det}}{D_{nozzle}} + 10.7 \qquad \textbf{2.6)}$$

However, Vyas and Kar (Vyas and Kar, 1975) did observe flow reversals in the initial region of the detuner as the detuner to nozzle diameter ratio increases. This flow reversal prevented any more secondary airflow to flow through the detuner. Therefore the secondary airflow through the detuner consequently decreases.

Similar trend for the entrainment ratio was derived numerically by Franco (Franco, 2000) using 2-D CFD analysis. The idle engine power condition gave the relationship:

$$\mu = 0.9304\frac{D_{\det}}{D_{nozzle}} + 1.1892 \qquad \textbf{2.7)}$$

Another interesting study by Choi and Soh, (choi and W. Y. Soh, 1990) used a time-iterative full Navier-Stokes analysis of the flow field of a two-dimensional ejector nozzle system. They also performed a parametric study for two controlling parameters, duct to nozzle area ratio and nozzle pressure ratio. The results show that there is an optimum area ratio for efficient pumping of secondary flow for a range of nozzle pressure ratios. At high area ratios, a free nozzle stream flow passes directly through the mixing duct without giving adequate pumping. At low area ratios, the jet boundary blocks the incoming flow.

Figure 2.24 shows the pumping characteristic of the ejector nozzle system for various area ratios and nozzle pressure ratios. Computations were made for nozzle area ratios (AR= $A_{secondary}/A_{primary}$) of between 1 and 12, and for Nozzle Pressure Ratios (NPRs) of 2.5, 3.5, and 4.5. The pumping characteristic is expressed in terms of entrained mass

flow per unit area (secondary flow) (W_s/A_s). This parameter is a better indicator of pumping than the secondary to primary mass flow ratio (W_s/W_p) when a free stream is present. The pumping characteristic is quite low and approaches a certain asymptotic value at high area ratios. This is because at high area ratios the pumping is negligible and most of the mass flow in the secondary passage is due to free stream flow. But as the area ratio decreases, pumping effectiveness increases and reaches a peak value, depending on nozzle pressure ratio.

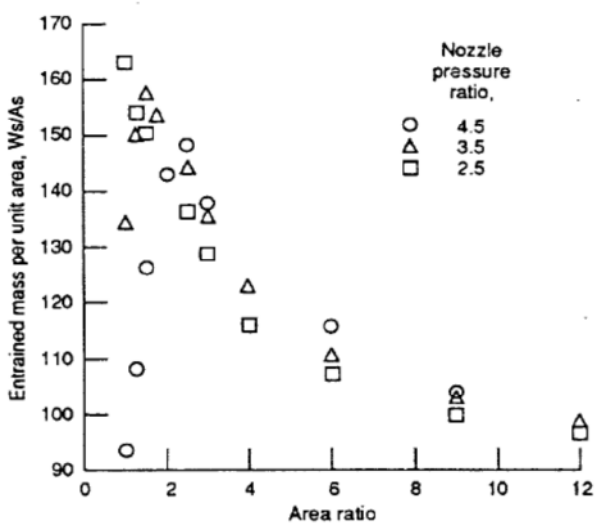

Figure 2.24 Pumping characteristics of ejector nozzle at various area and nozzle pressure ratios. (choi and W. Y. Soh, 1990)

2.11.3. Effect of High Temperatures and Pressures

Test cells are intended to test different size engines at different running pressures and temperatures. Quinn, (Quinn, 1976) found that test cell experiments performed at low pressure and ambient temperatures had profound shortcomings. The differences in pressures and temperatures are found to affect the performance of the ejector pump between the engine nozzle and detuner, and the amount of secondary airflow.

Quinn, (Quinn, 1976) conducted experimental work and produced interesting results. The plots in Figure 2.25 summarise the interplay between primary state variables and length where θ is the primary temperature ratio (primary temperature over ambient), π is the primary pressure ratio (primary pressure over ambient), and ψ is augmentation

ratio ($\theta^{-1/2}W_{secondary}/W_{primry}$). Curves drawn through cold data, θ = 1.0, have been included for clarity.

Increasing length of the mixing duct up to around its diameters rapidly improves performance by providing more time for the primary stream to transfer its energy to the entrained stream. Heating the primary fluids, if it has any effect at all, has a slightly favourable effect on performance because larger viscosities reduce the skewness of the flow in the same length of mixing duct.

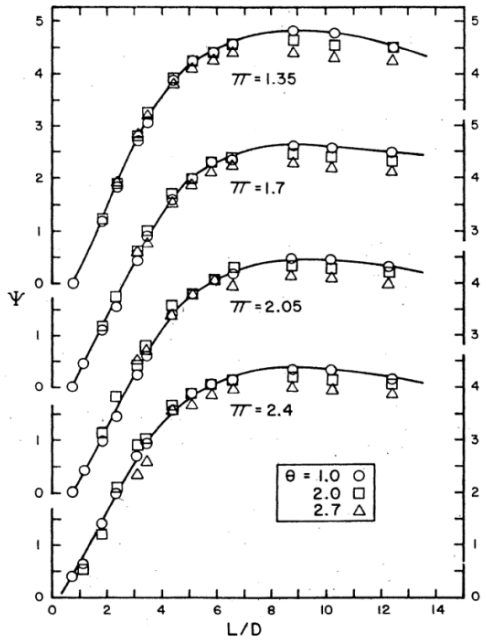

Figure 2.25 Augmentation performance on mixing duct length for parametric levels of the primary temperature and pressure ratios (Quinn, 1976)

The theoretical analysis suggests that increasing the temperature of the primary fluid reduces the performance of the ejector. The cause lies in the higher velocities of the heated primary jet and, thus, in higher ejector impact losses. Unfortunately, present analyses argue only from the thermodynamics point of view and largely ignore the dynamic role played by the heart of the ejector process, turbulent mixing.

2.12. Thrust Correction Factors

An indoor gas turbine engine test facility is by design, a wind tunnel. As discussed above the enclosure effect is created by secondary ambient airflow as a result of the ejector pump action of the engine exhaust jet plume entering the test facility exhaust

collector (detuner). This secondary entrained/by-pass airflow is up to five times greater than the initial airflow required by the engine/intake. In this case, the test facility would have an entrainment ratio of 5:1 (Parfitt and M. Bristow, 2006). This wind tunnel effect is necessary to assist the expulsion of all the undesirable hot gases from the test cell, to enable meaningful engine performance measurements in a repeatable, stable and consistent aerodynamic environment with non-turbulent ambient airflow. This will help eliminate any potential instability, hot gas re-ingestion or vortex formation. Also, any exposed elements of the test facility instrumentation/measurement systems can be cooled with ambient airflow to avoid overheating.

However, this wind tunnel effect creates a drag force acting upon the engine and its support structure, in an opposite direction to the test facility thrust measuring load cells. Therefore, it is necessary to account for this thrust drag debit (typically between 1-8%) with some form of calibration, to enable measured net thrust to be corrected to a set of reference datum conditions that e.g. include still air, to obtain a corrected gross thrust (Parfitt and M. Bristow, 2006).

Traditionally, this calibration has been carried out as a direct empirical back-to-back engine performance comparison between the indoor test facility and an outdoor free-field test facility with an assumed infinite atmosphere of still air. Unfortunately, due to the small number of occasions on which ideal weather conditions exist, and other issues such as pollution and noise, engine testing on outdoor facilities is now limited, time consuming and costly, and with inconsistent results. Also, the recent generation of large civil engines has outgrown the currently available “industry standard” outdoor test facilities, with claims of ground effects and micro-climates being confirmed using investigative instrumentation and CFD modelling. Parfitt, et.al., (Parfitt and M. Bristow, 2006) estimate a measurement uncertainty of approx. ±0.5% (random) with an additional –0.5% to -1.0% (systematic) in gross thrust in these circumstances.

Thus alternatives to the free field method have been developed and are being used. Such methods are the Rolls Royce First Principles Anemometer Method and the ITP (Industria de Turbo Propulsores) facility thrust correction factor described below.

Aerodynamic thrust corrections result from flow-induced forces within the test cell and may be divided into three: Inlet momentum drag, Structural drag on the engine and thrust stand, and Static pressure drag along the engine (SAE, 1976).

2.12.1. Inlet Momentum Drag

The most significant aerodynamic correction component of the thrust measurement is the inlet momentum, also known as the intrinsic inlet momentum, which produces a force on the engine as a result of drawing air into the test cell. For static engine testing, the magnitude of this force may be substantial; 1 to 10% of the measured thrust are typical (SAE, 1976). Since this force is, in effect, a drag term, it must be added to the measured thrust of the engine. The inlet momentum is a function of the airflow and the approach velocity in front of the engine, which is significantly affected by the amount of the cell airflow and the geometry of the test cell.

2.12.2. Structural Drag

Structural drag is generated by the cell bypass airflow scrubbing the exposed surfaces area of the engine casing, and “pushing against” the exposed structure which supports the engine on the thrust measurement stand (SAE, 1976). Cradle drag is obviously part of this factor.

2.12.3. Static Pressure Drag

Local acceleration of cell bypass airflow results in static pressure gradients along projected surfaces of the engine, particularly the bellmouth and exhaust nozzle. These pressure gradients generate horizontal forces which affect the measured thrust of the engine. Static pressure drag is sometimes broken down into bellmouth drag and boat tail drag. The magnitude of the static pressure drag is very sensitive to the cell exhaust geometry and engine to exhaust system spacing (SAE, 1976).

2.13. The Rolls Royce First Principles Method

The Rolls Royce first principles method has been developed to derive the aerodynamic thrust correction for an indoor test facility “in situ”, using arrays of anemometers and static pressure measurements in an extensive aerodynamic survey. This stand-alone method can be used in isolation or with reference to any other source, effectively relating an indoor test facility to free field using first principles. Parfit and Bristow

(Parfitt and M. Bristow, 2006) discussed the derivation of the thrust correction factor used.

The gross thrust equation gives all correction factor for the indoor test cell based on the thrust accounting system shown in Figure 2.26 and Figure 2.27:

Gross thrust = Net thrust + Inlet momentum drag + Cradle drag - Pre-entry stream tube force – External bellmouth scroll buoyancy + Engine and nozzle buoyancy forces (base drag) + Friction drag

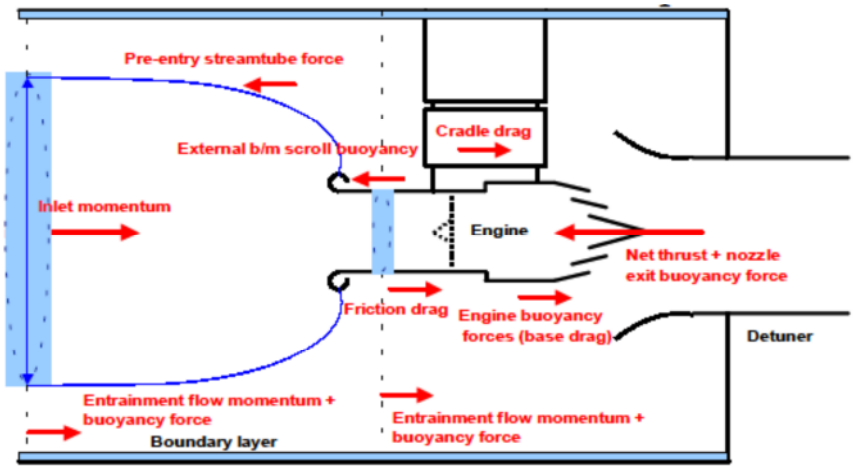

Figure 2.26 Illustratation of a full control volume thrust momentum box (Parfitt and M. Bristow, 2006)

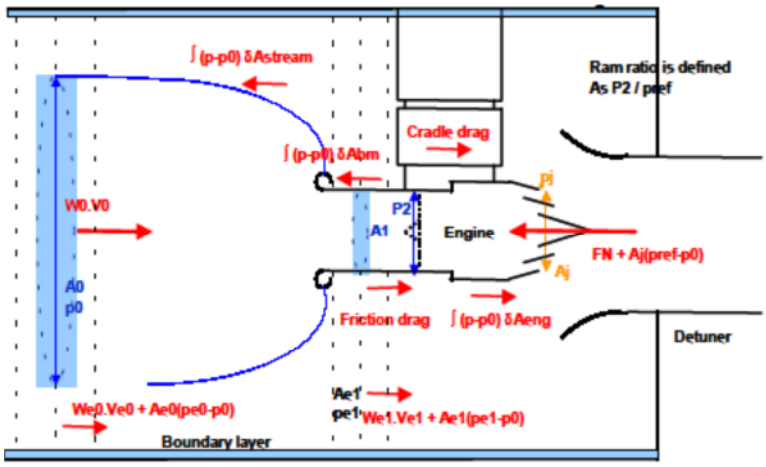

Figure 2.27 illustratation of a full control volume thrust momentum box in equation (Parfitt and M. Bristow, 2006)

2.13.1. Intake Momentum Drag

Intake or inlet momentum drag is calculated from measuring the mean airflow approach velocity ahead of the engine “stream tube” using 5-9 shrouded anemometers positioned

in cruciform formation, axially positioned 2-3 airmeter throat diameters upstream of the front face of the intake bellmouth flare (see Figure 2.28). This enables a basic area weighted averaging calculation of airflow velocity that is considered acceptable for most applications. Thus:

$$\text{Intake Momentum Drag} = \frac{(W_1 x V_0)}{1000} \quad \text{kN} \qquad \textbf{(2.8)}$$

Where:-

W_1 *=Observed engine inlet air mass flow - kg/s*

V_0 *=Mean velocity of 5 or 9 anemometers - m/s*

Measuring the airflow approach velocity over these anemometers also indicates the quality of the airflow profile to help the aerodynamic stability survey. Typically, the inlet momentum term is by far the largest term and will account for between 70%-90% of the total thrust correction.

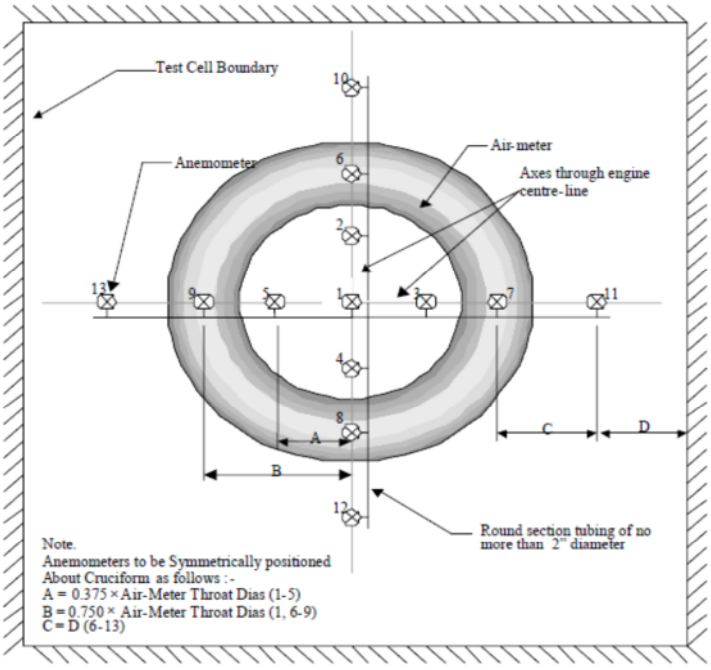

Figure 2.28 Anemometer positions (Parfitt and M. Bristow, 2006)

The radial positions specified on Figure 2.28 ensure that at least 1.5 x air-meter throat diameters of approaching stream tube is captured for measurement. The 4 additional anemometers (numbered 10-13 in Figure 2.28) are used for overall aerodynamic stability surveys but not for these specific inlet momentum drag calculations. In the case of engines with an air-meter throat diameter less than 1.5 meters, 5 anemometers are likely to suffice with the 0.375 throat diameter radius position anemometers (2, 3, 4 and 5) not

being required. This method enables the calculation of a basic area weighted average of airflow velocity that is considered acceptable for many applications. Any variation in the airflow approach velocity profile greater than ±15% from the mean when using 5 or 9 anemometers, is considered unacceptable.

2.13.2. Cradle Drag

This is found by calculating the pressure loading of entrained cell airflow acting upon the frontal blockage areas of all moving parts of the test facility thrust cradle and attached obstructions. This pressure loading is calculated by measuring the airflow velocities adjacent to these frontal blockage areas (approx. 100 mm from the anemometer centre line to blockage component edge). It is recommended for measuring the airflow velocities to use up to 10 shrouded anemometers evenly spread around the thrust cradle and attached obstructions.

$$\mathrm{Pr}\,essureLoading(\Delta p) = P_0\left(1-\left(\frac{1}{1+(6.0449x10^{-6}\,xV_{cell}^2)}\right)\right) \qquad \textbf{(2.9)}$$

Where:-

P_0 *= Cell static pressure – kPa*

V_{cell}*=Mean velocity of up to 10 anemometers – m/s*

The constant contained in Equation **(**2.9) fixes the cell static temperature at an ISA (International Standard Atmosphere) day value in conjunction with the speed of sound. Therefore there is no need to measure and calculate local cell static temperatures in the traditional equation ($\frac{1}{2}\rho V^2$). The measurement uncertainty associated with this has been approximated as ±0.01% thrust change for an ambient temperature change of ±20 K on EJ200 and is considered negligible. Typically, the cradle drag term is likely to account for between 5-25% of the total thrust correction.

$$The\quad cradle\quad drag\quad (KN) = \Delta p\quad A_{cradle}\quad C_{Dcradle} \qquad \textbf{(2.10)}$$

Where:-

Δp *= Pressure loading as Equation* **(**2.9) *– kPa*

A_{CRAD} *= Measured total frontal blockage area –* m^2

Cd_{CRAD} *= Calculated mean blockage area, Cd –* m^2

2.13.3. Base Drag (Detuner Suction)

Base drag is found by measuring the mean static pressure depression that results from accelerating entrained airflow velocities as they flow over the convergent exhaust nozzle into the detuner (see Figure 2.29). A suction force will be created as a result of the ejector. This force can be calculated using Δp × area change, where Δp is the mean of the measured static pressure from at least three equal axial planes (front, mid, rear) along the outer skin of the conical section of the exhaust nozzle, with the final position being measured by at least 4 circumferential sensors (see Figure 2.29).

$$Base \quad Drag = (P_0 - P_{7.5}) \quad (A_7 - A_8) \quad KN \tag{2.11}$$

Where:-

P_0 = *Cell static pressure (as Equation* **(**2.9*) – kPa*

$P_{7.5}$ = *Mean converging nozzle static pressure – kPa*

A_7 = *External front converging nozzle area* – m^2

A_8 = *External rear converging nozzle area* – m^2

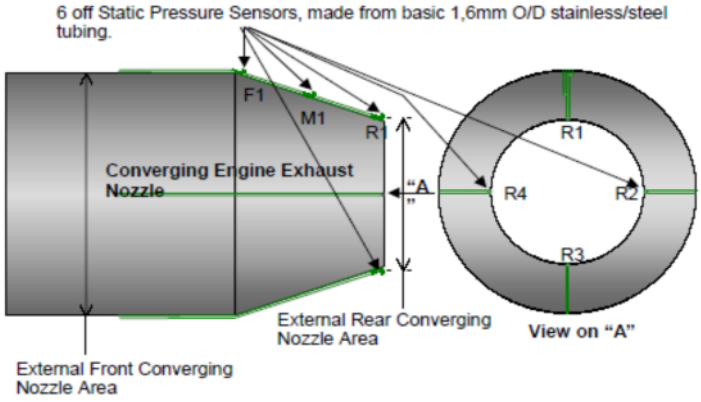

Figure 2.29 Nozzle static pressure configuration (Parfitt and M. Bristow, 2006)

2.13.4. Pre-entry Streamtube Force

This term represents the force acting on the pre-entry stream tube (including rear bellmouth scroll buoyancy force). It is not directly measurable and can be derived from CFD or estimated by applying the momentum theorem in potential flow for the secondary mass flow in Figure **2.27**. Therefore it can be represented as follows

Pre-entry Streamtube Force $\int (P - P_0)\partial A$ **= Entrainment momentum (1) + Entrainment buoyancy force – Entrainment momentum (0) =** $W_{e1}.V_{e1} + A_{e1}(p_{e1}-p_{e0}) - W_{e0}.V_{e0}$.

2.13.5. Engine and Nozzle Exit Buoyancy Forces

The buoyancy forces acting on the engine due to the reduction in cross-sectional area (front to rear) is the potential force $P_0(A_1\text{-}A_8)$. The bellmouth buoyancy term can be derived also using CFD or the 1D calculation.

Nozzle exit buoyancy force can be quantified from CFD and/or measured static pressure where $P_{ref}=p_j*(p_0/p_j)$. It has been found with reservations the net result defined on Trent 900 in its master test facility was between –0.2% and -0.3% of thrust relative to the basic first principles method.

$$Eng\ buyancyforce=\int(P-P_0)\partial A_{eng}+\int(P-P_0)\partial A_{bell}+Nozzleexit\ buoyancyA_j(P_{ref}-P_0) \quad \textbf{(2.12)}$$

2.14. ITP Method

The ITP test facility has been used to derive another quantitative method describing the thrust correction factor (Rios and Martin, 1998). The method defines proper system interfaces and analyses all the components acting on the metric assembly. It is slightly different from that obtained using the Rolls Royce First Principles Method because of different accounting systems. The thrust correction factors have been derived from applying a momentum balance to the control volume of the engine on its cradle inside the test cell (see Figure 2.30). The momentum equation which represents the balance of forces exerted on the engine is as in Equation (2.13).

$$WV_s+(P_s-P_0)A_s=F_m+WV_0+F_{cradle}+F_{(vxe\text{-}s(exterior)}-\int_o^e(P-P_o)dA-\int_{e(exterior)}^s(P-P_o)dA \quad \textbf{(2.13)}$$

Some of the terms in Equation (2.13) have already been described in the section referring to the Rolls Royce method. The accounting system in the left of Figure 2.30 which starts from station (0) and ends at (f) is used to derive the pre-entry force. It includes the forces acting on the bellmouth and could be represented in the equation:

$$(P_f-P_0)A_f+\int_0^e(P-P_0)dA+\int_{e(ext)}^f(P-P_0)dA=-W_sV_0+-W_sV_f \quad \textbf{(2.14)}$$

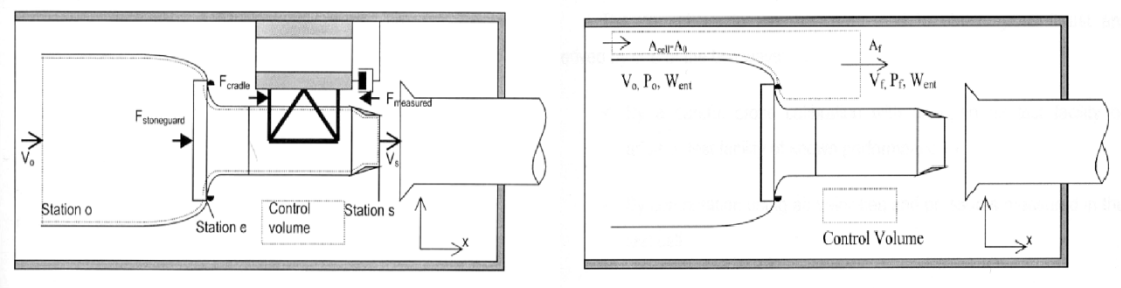

Figure 2.30 ITP control volume box (Rios and Martin, 1998)

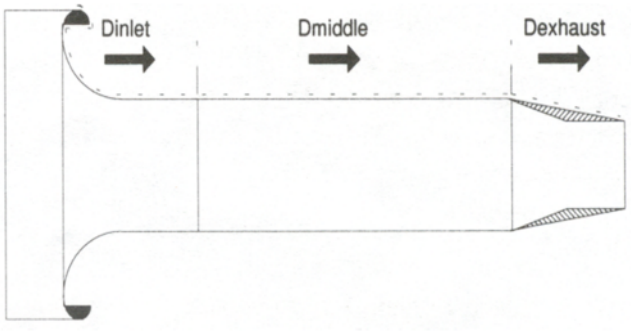

Figure 2.31 Engine external pressure drag (Rios and Martin, 1998)

The main assumption is that the viscous forces can be neglected and the flow is uniform in that part of the test cell around the engine.

2.14.1. External pressure drag

$$External\ \ pressure\ \ drag = \int_{e\,(exterior)}^{s} (P - P_0)\, dA \qquad \textbf{(2.15)}$$

The above term which appears in Equation **(**2.13) is the external viscous drag which is the viscous drag force due to secondary flow around the engine. This drag is divided into three; the front, the middle, and the rear (base drag) D_b (see Figure 2.31).

Concerning the drag at the front of the engine: by keeping the secondary air flow low the pressure difference (P - P_o) will be approximately zero, and the front component of the external pressure drag can usually be neglected. The middle body drag is also neglected since its value is small.

However, the drag at the rear of the engine cannot be neglected because the aft body of the engine is very close to the detuner where the entrained air starts accelerating to pass through the annular gap. The acceleration effect of the secondary flow causes a depression for the local static pressure at the nozzle exit. This depression at that region

causes a drag force to act on the rear of the engine which is the base drag. This force is defined in Equation **(**2.16).

$$D_b = \int (P - P_0)\partial A = (P_0 - P_{nozzle})(A_{engine} - A_9) \quad \textbf{(2.16)}$$

Where:

P_0 = Cell static pressure

P_{nozzle} = Static pressure on the external nozzle surface

A_{engine} = Engine cross-section

A_9= Cross-sectional area at engine nozzle plane

An engine with an afterburner was tested in the ITP test facility. (Rios and Martin, 1998) used the continuity equation assuming no pressure losses between sections (0) and (f). The pre-entry force and the bellmouth force correction factor were found to be less than 10% of the inlet momentum drag. Figure 2.32 shows the trend of the correction factor relative to the engine corrected mass flow. All correction factors except the cradle drag decrease with the engine mass flow. This is because the engine with afterburner works with a bigger nozzle throat and this increase the blockage of the detuner area. Thus less mass flow is pumped into the cell.

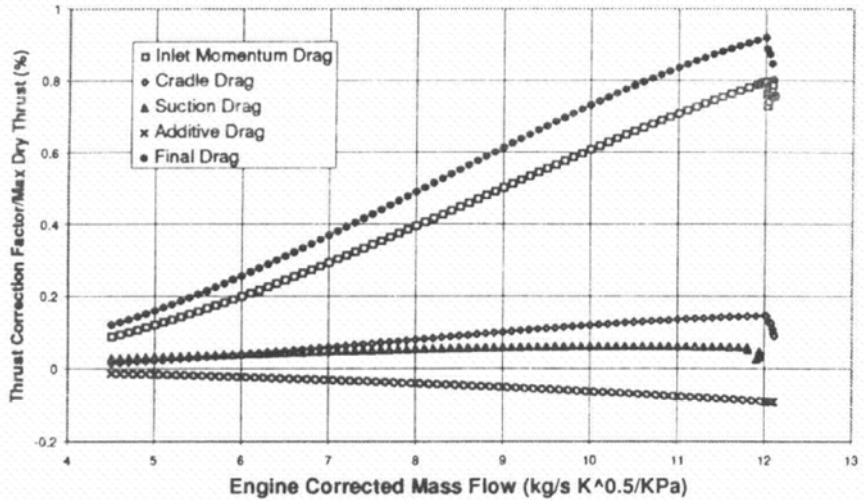

Figure 2.32 ITP Thrust Correction Factor (Rios and Martin, 1998)

2.15. Thrust Correction Equations

As discussed above, the testing of the new generation of large gas turbines in the open air, in “free-air” conditions, to establish ground level thrust performance is undesirable, and it has become increasingly important to establish an accurate thrust correction factor to account for the difference between load cell measurements and the true gross thrust of the engine. The correction factor arises as a result of the limited size of the test cell and consequent the air flow velocities within the cell due to engine mass flow and secondary flow entrainment.

The presence of secondary flow within the cell gives rise to several forces acting on the engine. Existing methods refer to high aspect ratios (area ratio of the cell/engine) and take into account the following drag forces: inlet momentum drag, cradle drag and base drag. Inlet momentum drag is equal to the product of the engine mass flow and approach flow velocity (WV_0). Cradle drag is due to secondary flow around the cradle (F_{cradle}). Base drag is the result of the low pressure region at the inlet of the detuner and which appears as a force which attempts to suck the engine backwards ($F_{suction}$). The forces are illustrated in Figure 2.33.

The thrust measured (F_m) refers to the measurements on load cells located on the cradle. Inlet momentum can be computed using anemometers located at a suitable plane upstream of the engine. Cradle drag can be calculated using manometers positioned at the cradle. Suction or base drag is computed by monitoring the static pressure at the engine exhaust nozzle.

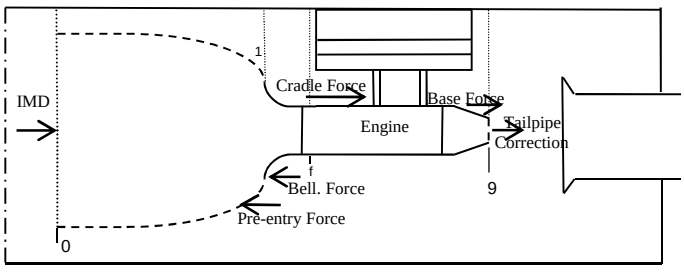

Figure 2.33 thrust correction factors (Gullia, February 2006)

The gross thrust of the engine (F_g) can be computed using Equation (2.17) which applies to high aspect ratios only [Rios et al. 1998].

$$F_g = F_m + W.V_0 + F_{cradle} + F_{suction} \qquad \textbf{2.17)}$$

Detailed analysis by Gullia (Gullia, February 2006) has shown that additional forces may need to be included, especially if the aspect ratio of the test cell is reduced. Gullia's work was focused on the development of thrust correction equations for indoor test facilities; he related the forces acting on the forebody of the engine to cell entrainment ratio and cell aspect ratio, and demonstrated that forces neglected in Equation (2.17) have a significant effect when either the entrainment ratio increases or the aspect ratio of the cell reduces as shown in Figure 2.34. The engine comprises a bell-mouth and carcass and there is also the engine cradle. These components comprise what is known as the metric assembly (see Figure 2.33).

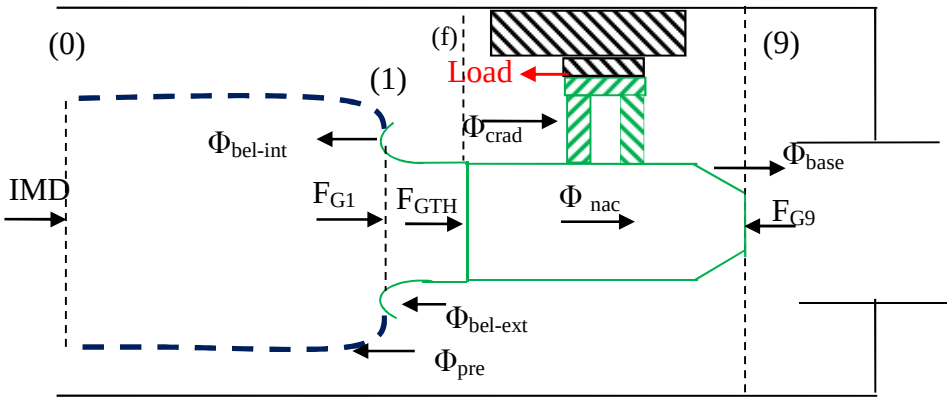

Figure 2.34 Forces acting on the metric assembly (Gullia, February 2006)

Figure 2.33 and Figure 2.34 represent an engine in a classic indoor sea-level test bed facility. The metric-assembly is in green and the non-metric components are in black. Figure 2.34 contains interfaces (0), (1) and (9) which will be used in the derivation of the thrust correction equation.

The accounting system is the system chosen to evaluate the thrust delivered by the engine. The load measured (L) is the reaction of all the forces acting on the selected accounting system as shown in Equation 2.18. The thrust correction factors relate to the measured force acting and can be due to the engine metric assembly or on one of the stream surfaces belonging to that system.

$$L = \sum_{i=1}^{n}\sum_{j=1}^{m} (\phi_{Gi} + F_{Gj})_{accounting-system} \qquad \textbf{2.18)}$$

Where ϕ_{Gi} is the axial direction force element, and F_{Gj} is the absolute force .

The fundamental equation which has been used for the derivation of all the thrust correction equations is:

$$L = F_{G9} - F_{G1} - \phi_{Gmetric} \quad \textbf{2.19)}$$

Where,

$$\phi_{Gmetric} = \phi_{Gcarcase} + \phi_{Gcradle\ metric} + \phi_{Gbell\ ext} \quad \textbf{2.20)}$$

$$L = F_N - D'_{metric} + (F_{G9'} - F_{G0})_{ext\ pot} - \phi_{Gbase} \quad \textbf{(2.21)}$$

Where the metric drag D'_{metric} is the simple sum of the individual drags due to the cradle, bellmouth and carcase.

$$D'_{metric} = D_{cradle\,metric} + D_{bell\,ext} + D'_{carcase} \quad \textbf{2.22)}$$

The stream gauge force difference between stations (0_{ext}) and (9_{ext}) is represented as equation (2.23)

$$\Delta F_{09ext\ pot} = -\{\mu^2\left[(b-c)^2 + 1 - 2b - 2c\right] + 2\mu\left[(b-c)^2 - b + c\right] + \\ + (b-c)^2\} \times \frac{W_p}{2\rho A_{cell0}} \quad \textbf{(2.23)}$$

Where,

$$b = \frac{A_{cell9}}{A_{cell0}} \quad \textbf{(2.24)}$$

$$c = \frac{A_{nozzle}}{A_{cell0}} \quad \textbf{(2.25)}$$

$$L = F_N + \phi_{Gpre} - \phi_{Gbell\,ext} - D_{carcase} - D_{cradle} + (F_{G9} - F_{Gf})_{ext\,pot} \quad \textbf{2.26)}$$

$$L = F_{G9} - F_{Gth} - \phi_{bell} - D_{carcase} - D_{cradle} + (F_{G9} - F_{Gf})_{ext\,pot} \quad \textbf{2.27)}$$

In summary, Gullia (Gullia, February 2006) defined three different thrust correction equations: (2.21), 2.26), and 2.27), using alternative force accounting systems. Aerodynamic principles have been applied for the derivation of one-dimensional

relationships for the calculation of each thrust correction factor using generic engine-cell performance and dimensions.

3. Experimental Work

The experimental work of this research has been carried out in the test facility available in Cranfield University. Cranfield University has invested in research studies evaluating the performance of gas turbines in test beds. Cranfield University has designed and constructed a small test bed facility for testing a micro jet engine. The test cell provides experimental data for the support of indoor testing research analysis. The test cell has been designed and built with the ability to change the cell cross section area as well as the distance between the engine nozzle and the detuner. This feature of the test cell gives the ability to accomplish many parametric studies.

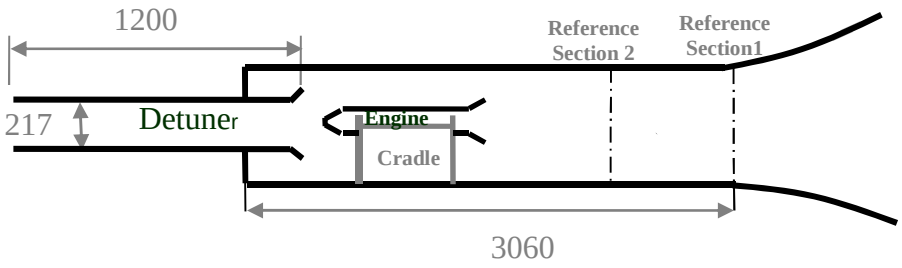

Figure 3.1 Cranfield test cell lay-out (mm)

The general layout of Cranfield test cell is shown in Figure 3.1. The test cell has a rectangular shape with a horizontal intake. The bellmouth has been designed and manufactured by Rolls Royce to maintain a smooth and uniform airflow. Model test cells have two types of power simulators either the turbine powered simulator (TPS) and the ejector powered simulator (EPS) (SAE, 1976). The test cell was designed for testing a small gas turbine engine which is manufactured by AMT Netherlands. The engine is usually used for radio controlled airplanes. Rolls Royce has designed and manufactured a thrust measurement rig (TMR) to hold the engine in the test cell (see Figure 3.2).

The TMR which has two main components, the thrust measurement device (TMD) and the engine airmeter can be used for indoor and outdoor testing. The TMD has a moving part which is connected to the fixed structure via an interface. The thrust is measured by two load cells, one in each side of the engine. The engine and the TMD are allowed to move freely axially. Gonzalez (Gonzalez Galinez, 2003) conducted an experimental work and found out the drag coefficient for the TMD is 1.79 and the blockage frontal area is 0.005856. The test cell has a detuner pipe which takes the exhaust and the

secondary airflows directly to atmosphere. The advantage of this simple exhaust system is the ability of moving the detuner forward and backward with respect to the engine nozzle.

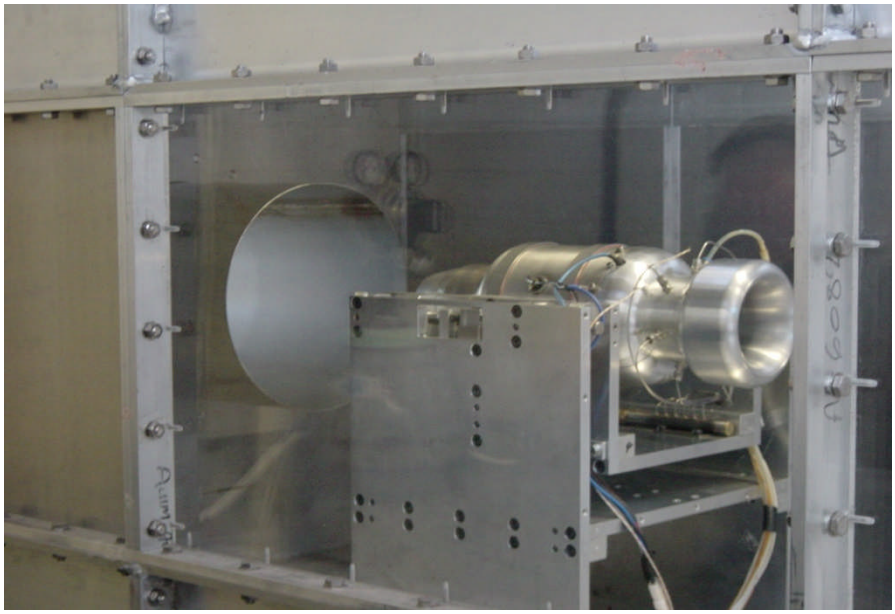

Figure 3.2 Engine on Cradle

3.1. Test Cell Bellmouth Calibration

Gas turbine test facilities have two types of intake system, horizontal or vertical. The main function of the intake is to maintain a smooth and uniform flow to the test cell. The Cranfield University which is enclosed inside a test house to prevent any cross wind disturbances and has a horizontal type and its purpose is to provide a uniform flow profile. The 700mm x 700mm special inlet designed by Rolls Royce has an initial converging section that rapidly taper into the test cell **(**see Figure 3.3**)**. Accurate knowledge of air mass flow rate and velocity is very important for experimental purposes so the cell intake has to be calibrated. It was calibrated some years ago but only for one engine power setting. As it would be expensive and time-consuming to design different intake geometries for each new application, the aim here is to cover a wider range of Mach numbers for different engine power settings. For these investigations the Bellmouth will be adapted to provide smooth transition into smaller cross-sections of 550mmx 550mm and 470mm x 400mm.

Figure 3.3 Bellmouth on test facility

Consider a conventional velocity profile for laminar flow in a circular pipe, the velocity at the walls is zero and progressively increases towards the centreline according to a parabolic law. For turbulent flow in a circular pipe the flow profile is as shown in Figure 3.4. For a pipe of radius R, the velocity, V, at a distance r from the centre line of the pipe can be approximated quite well by the power law:

$$V = u_{\max}\left(1 - r/R\right)^{F} \qquad \textbf{3.1)}$$

Where F depends on the friction factor but is usually in the range 0.12 to 0.16 (Mott, 2005).

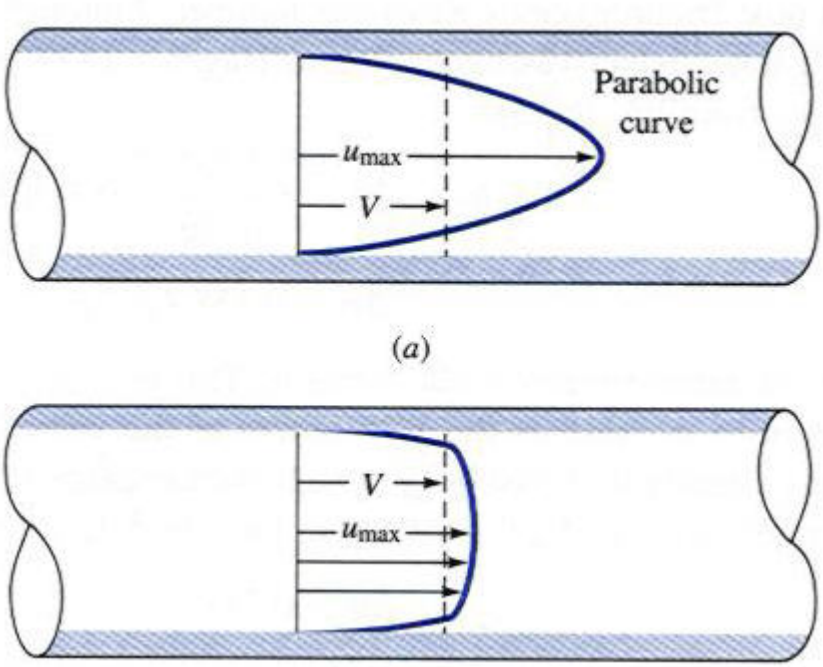

Figure 3.4 Velocity profile for (a) laminar and (b) turbulent flow in bellmouth with circular cross-section (Mott, 2005)

Essentially, the velocity profile is fairly uniform across the pipe except in the areas close to the wall. If the duct is square and not circular then these edge areas become even more important. The calibration is to find a correction factor, K, to the theoretical equation that allows for these areas. A reference cross-section upstream of the engine was selected where the measurements would take place, see Figure 3.5. This plane was 1m inside the bellmouth to allow the flow pattern to develop. For improved accuracy in the air flow measurements, the cross-section was divided into smaller areas. The local velocity at each of these small areas was measured using the difference between total and static pressures. Knowing the velocity distribution across the reference cross-section the total mass entering the test cell can be quickly computed.

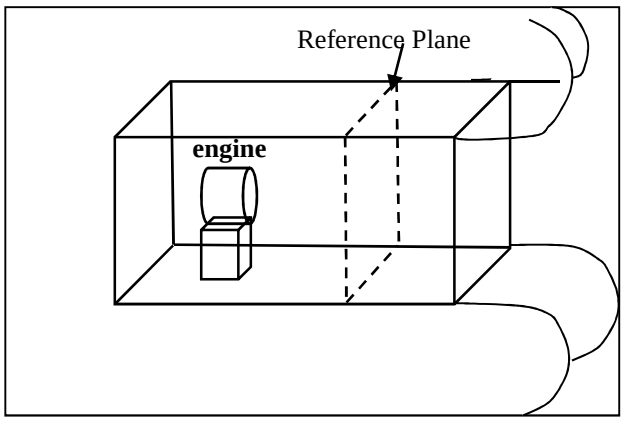

Figure 3.5 Relative positions of engine, bellmouth and reference measurement plane

During the tests, to enhance the generation of a turbulent layer, a “trip” was placed in the bellmouth. This was simply a wire 1 mm diameter around the bellmouth as seen in Figure 3.3.

Total pressure (P) is measured by a Pitot-static tube placed at the centre of the cross-section, see Figure 3.6. Both the reference pressure and reference velocity were determined using this Pitot tube. Static pressure is the average of the static pressure (p) measured at tappings at the four sides at the reference cross-section.

On each edge of the reference plane there were 7 static pressure probes, so that a total of 28 static pressure probes were spaced equidistant around the outside of the plane, see Figure 3.7. There was also a traversing Pitot-static tube which could move (traverse) around the cell. Specially built pressure rakes were fabricated, which measured total pressure at the locations in which they were positioned. All of the pressure probes, whether measuring static or total pressure, were linked directly to a pressure transducer. The pressure transducer displayed the local difference between total and static pressure in the regions of interest. This information was vital to determine the local velocities in the said regions. Figure 3.7 shows a schematic of the approximate positions for the pressure probes. The blue lines show the positions of the total pressure rakes. The green lines show the vertical traverse of the Pitot-static tube. The red spot is the reference position of the Pitot-static tube; and static pressure measurements were made at equidistant positions on the sides of the reference cross-section.

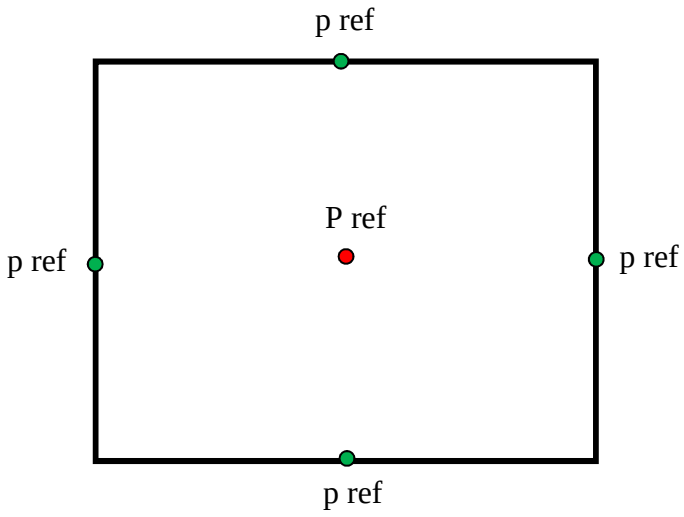

Figure 3.6 General schematic for measurement points in reference plane

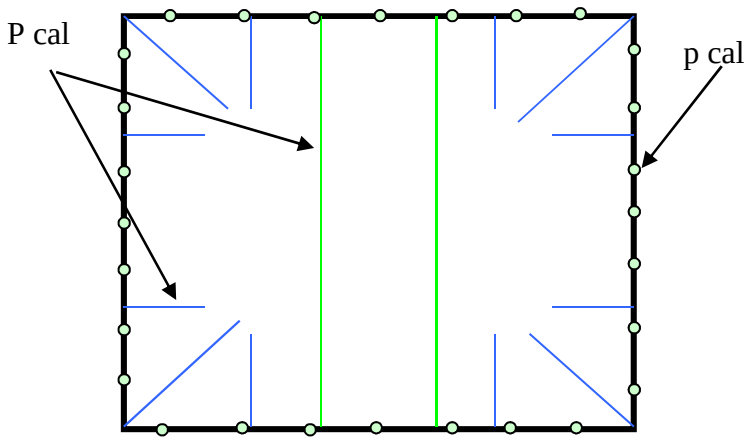

Figure 3.7 Schematic of the positions and lines of traverse of the pressure probes

Thus, for mapping the air flow velocity the reference plane has been split into 33 smaller areas, and by measuring the local value of (P-p) it was possible by assuming the flow to be incompressible (low velocity inside the cell) to find the local velocity for each area:

$$V_{local} = \left[2(P - p)_{local} / \rho\right]^{0.5} \quad \textbf{3.2)}$$

Knowing the local velocity, the local area over which this velocity applied, and the temperature of the airflow it was possible to find the local mass flow rate. The density of the air was calculated according to:

$$\rho = p_{reference} / Rt \quad \textbf{3.3)}$$

Where:

$$p_{reference} = P_{atm} + (P_{TH} - P_{atm}) + (P_{cell} - P_{TH}) \quad \textbf{3.4)}$$

$p_{reference}$= average static pressure in duct, (Pa)

P_{atm} = atmospheric pressure, (Pa),

P_{TH} = total pressure in the test house (Pa),

P_{cell} = total pressure in the test house (Pa),

R = gas constant= 287.04 J□kg^{-1}□K^{-1}, and

t = air static temperature (K).

Once the local velocity, area and density were known, the local mass flow was found using:

$$W_{local} = A_{local} \quad \rho_{local} \quad V_{local} \qquad \textbf{3.5)}$$

The average density over course of the four days was:

$$\rho_{average} = \left(\left(\frac{p}{RT} \right)_1 + ... + \left(\frac{p}{RT} \right)_n \right) \Big/ n \qquad \textbf{3.6)}$$

With this data, K could be found as:

$$K = \frac{\sum V_{local} \quad A_{local} \quad \rho_{local}}{\rho_{average} \quad A_{total} \quad V_{ref}} \qquad \textbf{3.7)}$$

This is a correction factor to allow cell mass flow to be accurately calculated from the Pitot-static measurements at the reference measurement. Table A. 1, Table A. 2, Table A. 3, and Table A. 4 in Appendix A show the flow measurements.

3.2. AMT OLYMPUS MICRO ENGINE

The micro gas turbine engine which is used in Cranfield University test facility is made by AMT Netherlands. The engine has a single radial compressor, an axial turbine and the combustion chamber is of the annular type. The engine is protected by means of a microprocessor controller (ECU) that is fully automatic and needs no adjustment. Engine throttle is controlled via the ECU which regulates the performance of the turbine such as rotational speed and exhaust temperature. The engine specifications are listed in Table 3.1.

The engine uses a propane- start which is the most common starting method. This method uses propane gas injected in to the turbine, and ignited by a standard glow plug to begin the starting process. The propane heats the turbine combustion chamber and gets the compressor spinning to a pre-determined RPM. Once ignited and running on propane, the engine will then automatically begin injecting kerosene in to the turbine. Once the start-up process is complete, the engine will continue to run on kerosene. The Olympus also uses the fuel for lubrication, so the fuel must be premixed with 4.5 % Aeroshell 500 turbine oil before use.

The engine airmeter is 61.42 mm diameter which is within the recommended figure by AMT Netherlands. Rolls-Royce designed the engine airmeter to measure the static pressure at the front of the engine during any run. This is achieved using six static pressure tappings located on a single measuring plane around the circumference of the intake airmeter. Measuring the difference between the static pressure and in the test house gives the depression at the engine throat.

Diameter [mm]	130 mm
Length [mm]	270 mm
Weight [gr]	2400
Thrust @ max rpm [N]	190
Thrust @ min rpm [N]	7
Pressure Ratio @ max rpm	4:1
Mass Flow @ max rpm [gr /sec]	400
Maximum RPM	110,000
Exhaust Temperature ^{0}C	650
Max Exhaust Temperature ^{0}C	700
Fuel Consumption gr/min @ max rpm	550

Table 3.1 AMT Olympus gas turbine specifications

The mass flow passing through the airmeter cross section can be calculated. The static temperature is worked out by measuring the total temperature at the top of the airmeter by using the compressible flow relationship so the density can be calculated by using the ideal gas equations. The Mach number is calculated by assuming the total pressure at the engine throat is constant from the reference plane.

The length of the parallel section of the intake airmeter is sufficient to ensure that the static pressure is uniform at the measuring plane. Therefore the only correction required is for any increase in the boundary layer.

The airmeter has a flow coefficient (Cd) due to the flow distortion. The factor of the actual air massflow over the ideal air mass flow and is represented as a function of the pressure ratio P/Ps or Mach number (see 3.8).

$$C_{d\,(airmeter)} = \frac{Actual.Mass.Flow}{Ideal.Mass.Flow} \qquad \textbf{3.8)}$$

Gonzalez (Gonzalez Galinez, 2003) has used three methods to calculate the flow coefficient. The first method was suggested by the manufacturer and the second was derived by Lahti and Hamed and a 2-D CFD model. Figure 3.8 shows the results for the three methods (Gonzalez Galinez, 2003). The design point which represents the engine full power mass flow as given by the manufacturer. It is represented on the figure by the dotted line. for the accuracy of the measurements the calibration of the airmeter must meet the standard coefficient value within ± 0.25%.

The Mach number of 0.4 was considered to be the maximum for comparing the three methods. The three methods have a difference of around 0.02 to 0.08% and a deviation between 0.16-0.18% which is within the recommended standard value. The observation was that CFD tool wasn't able to converge for Mach numbers below 0.2. The tool which has been used is the one that has been developed by the airmeter manufacturer; Rolls Royce.

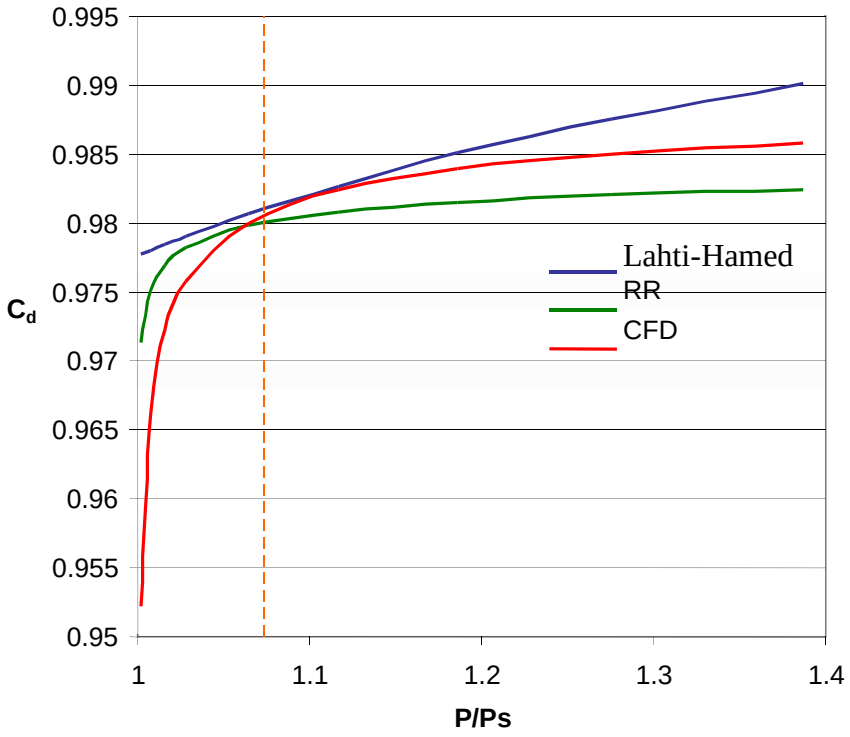

Figure 3.8 Engine inlet flow coefficients (Gonzalez Galinez, 2003)

3.3. Experimental Tests

The aim of this task is to investigate the effect of the test cell cross-section on the thrust correction factor and flow behavior inside the cell. Three different test cell cross-sections have been tested (700mm x 700mm, 550mm x 550mm and 400mm x 470mm). For each test cell cross-section four engine power settings were tested at four engine-detuner distances, as shown in Table 3.2 Test run data.

The first configuration is 700x700 cross-section test cell in the shape of rectangular parallelepiped. The initial step is to define the separation distance from engine nozzle to entrance to the detuner. The first case is where the engine nozzle and the detuner entry are in the same plane, d=0. After that the experiment begins and the engine is tested for four power settings, 65%, 75%, 85%, and 95%. This is then repeated for the three separation distances; d, 2d, and 3d, where d is the nozzle diameter. The same set of experiments is then repeated for the other two test cell configurations. Indoor and outdoor test runs are required for the same four power settings.

Configuration	Length of transition piece (mm)	Transition piece cross-section (mm)	Engine- detuner distance (nozzle diameters)	Power setting (%)
1	No	700x700 to 700x700	0,1,2,3	65, 75, 85, 95
2	1333	700x700 to 550x550	0,1,2,3	65, 75, 85, 95
3	2000	700x700 to 400x470	0,1,2,3	65, 75, 85, 95

Table 3.2 Test run data

The test cell bellmouth which was designed and manufactured by Rolls Royce, see Figure 3.9, has a 700x700 mm^2 cross-section which fits onto the first test cell.. The bellmouth is expensive and it would also be time-consuming to design a new bellmouth for each of the two smaller test cell configurations. Instead, it is more convenient to use the same bellmouth for the other configurations and to design transition pieces. These transition pieces are shown in Figure 3.10 and Figure 3.11 and are positioned between the bellmouth and the particular test cell. Both are tapered parallelepipeds designed with an inclined angle of less than 8^o. the inclined angle was kept small to avoid any flow separation effects. This gives the Cranfield University test cell the advantage of the simplicity by which the cross-section can be changed.

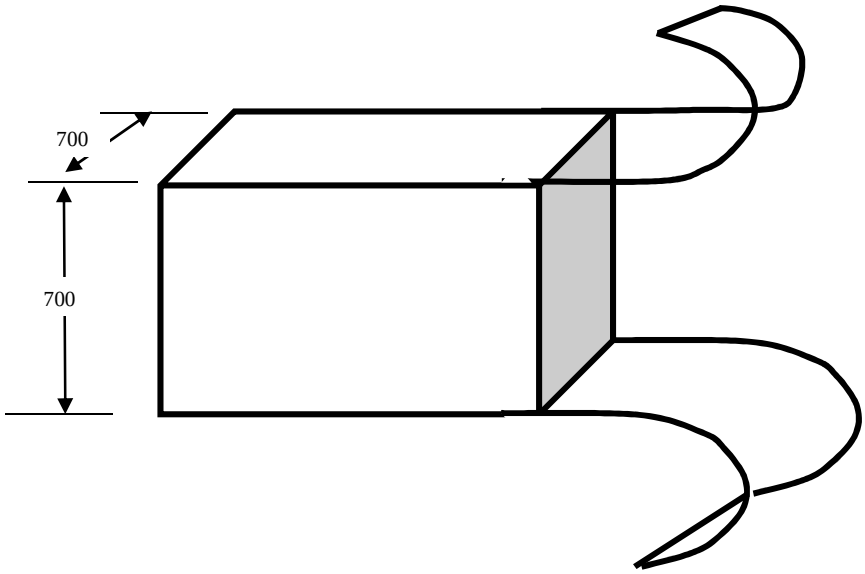

Figure 3.9 Test cell bellmouth (lengths in mm)

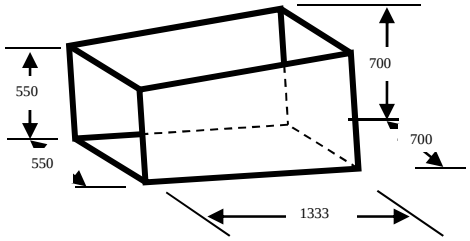

Figure 3.10 Configuration 2 transition piece (lengths in mm)

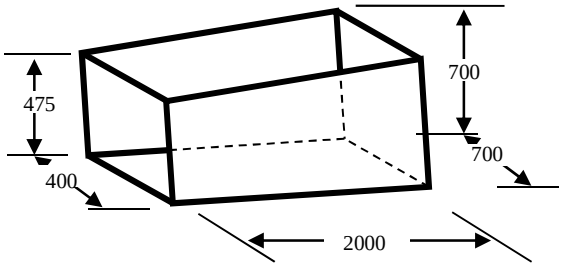

Figure 3.11 Configuration 3 transition piece (lengths in mm)

3.4. Instrumentation and Measurements

This section describes the instrumentation used in the experiments which were the experiments have been conducted over different days with different ambient conditions. In each experiment there was a mixture of measurements; engine thrust, flow velocities inside the test cell, pressures at a number of points in and around the test cell, and temperatures at the inlet and exit of the test cell, engine, and detuner, as well as all relevant engine data which was mostly delivered by the engine ECU. The ambient conditions and the test house pressure and temperature were also recorded.

It is essential to normalize the data results to standard day conditions; pressure of 101.325 kPa and temperature of 15 ºC. Thus the local absolute atmospheric pressure (P_{amb}) was recorded for each test run using a barometer positioned outside the test

house, and ambient temperature (T_{amb}) recorded using a mercury in glass thermometer inside the test house. All the results were normalized according to British Standards using Equations 3.9, 3.103.10, and 3.11 (BS 3135:1989) and where $W_{normalised}$ is corrected engine mass flow.

$$W_{normalized} = \frac{W \cdot 101325 \cdot \sqrt{T_{amb}}}{P_{amb} \cdot \sqrt{288}} \quad \textbf{3.9)}$$

$$Thrust_{normalized} = \frac{Thrust \cdot 101325}{P_{amb}} \quad \textbf{3.10)}$$

$$rpm_{normalized} = \frac{rpm \cdot \sqrt{288}}{\sqrt{T_{amb}}} \quad \textbf{3.11)}$$

The test house total pressure is measured before and after any experiment by a differential manometer. This measured the pressure difference between the inside and outside the test house. The manometer is placed in a corner of the test house where there was no detectable air flow. It was essential for accurate and repeatable measurements that all the transducer used were calibrated over their working range.

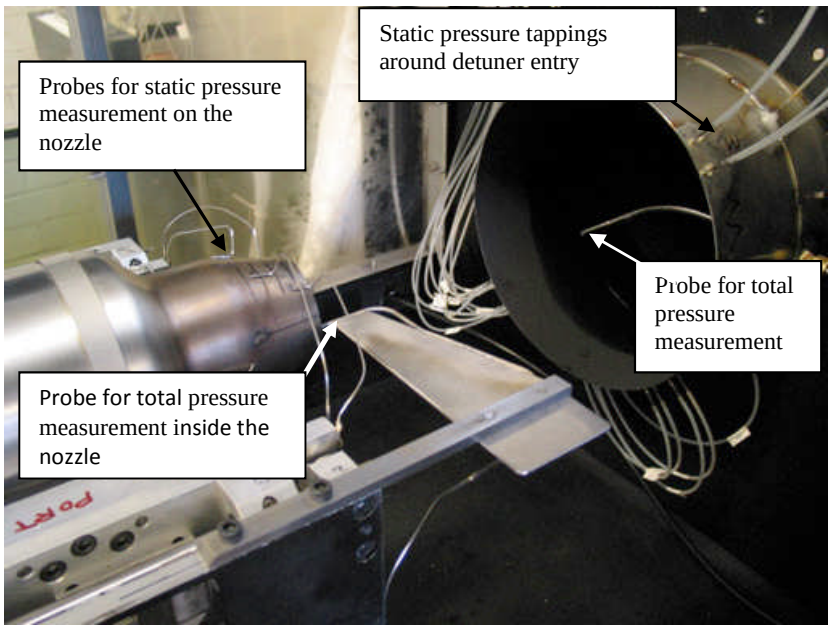

Figure 3.12 Instrumentation around the engine nozzle and detuner

Static pressure measurements were taken in many areas in and out of the test cell. Figure 3.12 shows the measurement points of interest and the instrumentation positioned at the engine nozzle and detuner entry. There are four static pressure probes on the engine nozzle to measure pressure depression in that region. The four probes were positioned at 8 mm, 18 mm, 28 mm and 38 mm upstream of the nozzle exit plane on the outer surface of the nozzle. Obviously no probe can be positioned at the nozzle exit plane due to the local high temperature. A probe to measure total pressure inside the nozzle was positioned to the side of the nozzle at the turbine exit to protect it from the high temperature.

Static and total pressure measurements were made at the detuner entry, see Figure 3.12. In the middle of the entry plane there was a probe to measure total pressure which was recorded using a differential manometer. Figure 3.12 also shows some of the thirty co-planer static pressure measurement tappings around the detuner entry used to estimate the depression at that region.

Static pressure tapping location from detuner entry (mm)	Number of tappings
3	4
7	4
12	4
18	4
25	2
33	2
42	2
52	2
67	2
97	4

Table 3.3 Static pressure tapping locations on the detuner

(the location is distance in mm along the detuner from the entry plane)

Table 3.3 gives the location of all thirty probes. Each of the set of readings was measured by a differential transducer connected via a Scanivalve pressure

scanner/switch for pressure measurement sequentially using a single pressure transducer and transmission to a computer which stored and averaged them.

The transducers give relative not absolute pressure readings, and equation (2.17 has to be used. The first term *(P_{atm})* is measured directly by the external barometer. The second term ($P_{TH} - P_{atm}$) is measured directly by a manometer. The average of the four pressure readings up-stream of the test cell-just after test cell bellmouth, is the difference in pressure between these four points and the test house ($p_{cell} - P_{TH}$). This is the last term in the equation.

$$p_{ref} = P_{atm} + (P_{TH} - P_{atm}) + (p_{cell} - P_{TH}) \qquad \textbf{3.12)}$$

The internal temperature is measured in many locations inside the test cell and test house. The engine nozzle temperature needed for engine cycle calculation was directly recorded by the engine ECU. A thermocouple was installed in the nozzle for comparison purposes. The fuel temperature was measured for the fuel flow measurements. The temperature was also measured at the top of the engine nozzle to detect any possible hot air recirculation.

Thermocouples were of K type: Nickel/Aluminium or Nickel/Chromium alloys. These thermocouples have a wide temperature range and their accuracy is based on the specification of the alloys used. According to BS EN 60584.2:1993 the accuracy is:
Temperature range -40 to +333 ºC: +/- 2.5 ºC.
Temperature range 333 to 1200 ºC: +/- 0.0075 (t ºC).

Engine ECU gives real-time readings for two performance parameters, engine rotational speed and exhaust temperature.

Figure 3.13 shows the nine locations of the velocity measurements. These measurements were used for calculating the cradle drag. Other velocity measurements were taken at the reference section 2 for the intake momentum drag calculations. The instrument used was a hot wire anemometer with 1 m/s accuracy if positioned within an angle of ± 15º to the flow direction. This anemometer was appropriate for the low velocity laminar flow found in the test cell.

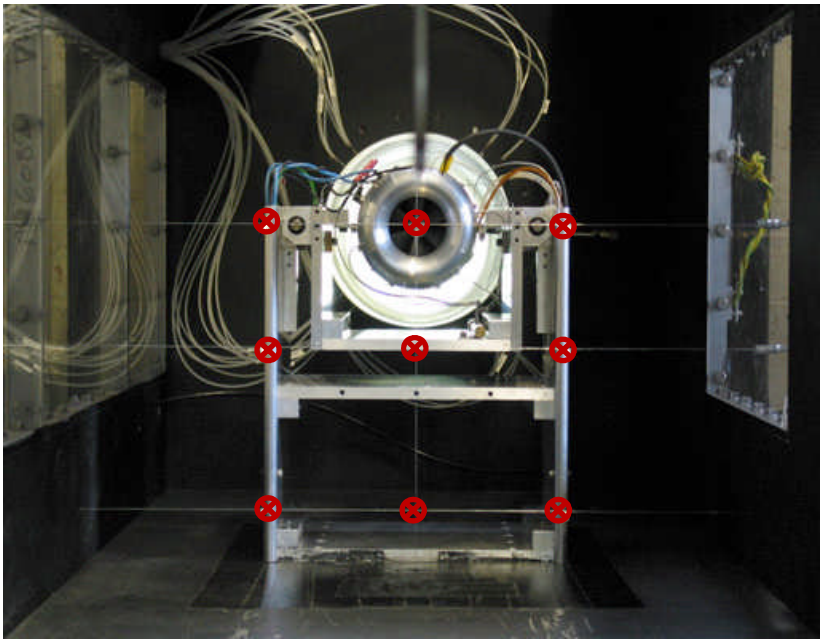

Figure 3.13 Velocity measurement points in front of cradle

The velocities inside the test cell were investigated in a number of positions around the engine to study the flow pattern around the engine. Figure 3.14 shows all the points and their locations inside the test cell, where A is 20 cm and B is 30 cm. This helps for a better understanding of the flow behavior and allows comparison of experimental results to the CFD model. The instruments used was the one mentioned above, a thermal anemometer.

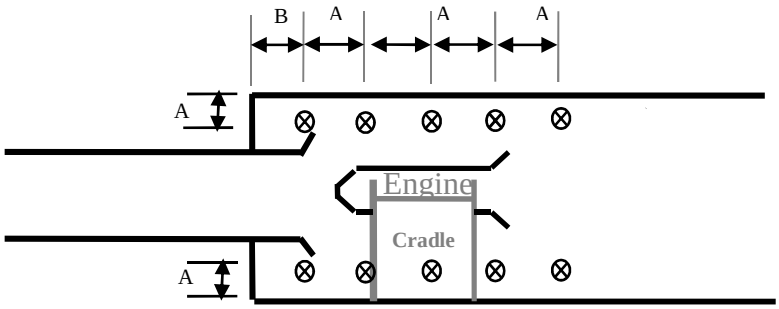

Figure 3.14 velocity measurements inside the test cell

Table 3.4 summarizes all the instruments used, parameters and measurements taken with their locations.

Parameter	Instrument	Location
P_{atm}	Barometer	External
T_{amb}	Thermometer	Test house
$P_{atm} - P_{TH}$	Pressure Transducer	Test house
$(P-p)_{ref}$	Pressure Transducer - Pitot tube - four static probes	Reference
$(P_{TH}-p_{ref})$	Pressure Transducer - Four static probes	Reference
$(P_{TH}-p_{eng})$	Pressure Transducer - Engine air meter	Engine throat
Thrust	Load cells - two	TMD
T_{cell}	Thermocouple	Cell roof
v_{ref}	Thermal anemometer	Reference 2
v_{cradle}	Thermal anemometer	Cradle
RPM	Engine control unit	ECU
Fuel flow	Engine control unit	Scale-meter
p_{nozzle}	Pressure Transducer - Static probes	Nozzle ext
P_{nozzle}	Digital Manometer - Pitot tube	Nozzle surf
$p_{detuner}$	Digital Manometer	Accom. Reg.
$P_{detuenr}$	Digital Manometer	Accom. Reg
T_{nozzle}	Thermocouple	Nozzle
T_{fuel}	Thermocouple	Fuel tank

Table 3.4 : Summary of measurements and instrumentations

3.5. Results

The secondary air flow in the test cell affects the thrust measurements. Figure 3.15 to Figure 3.17 show the test cell mass flow with engine mass flow for all four configurations and all four power settings. The figures show a monotonic relationship between the secondary air mass flow through the test cell and the engine mass flow. The effect of the nozzle-detuner separation distance was such that for a given engine mass flow, an increase in the nozzle-detuner separation increased the test cell secondary air mass flow rate. All the test cell configurations gave similar trend lines except for the 550x550 configuration with a nozzle-detuner separation of 3 nozzle diameters.

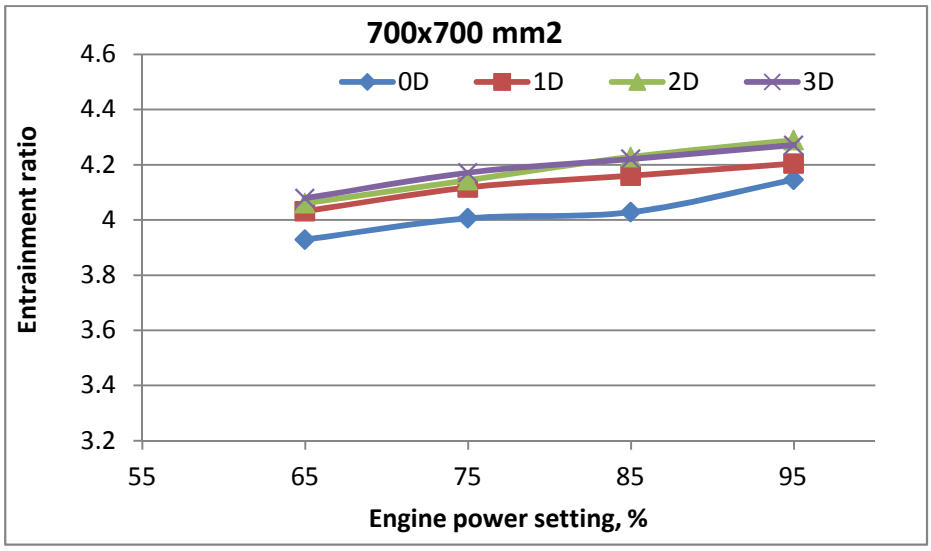

Figure 3.15 Test cell total air mass flow

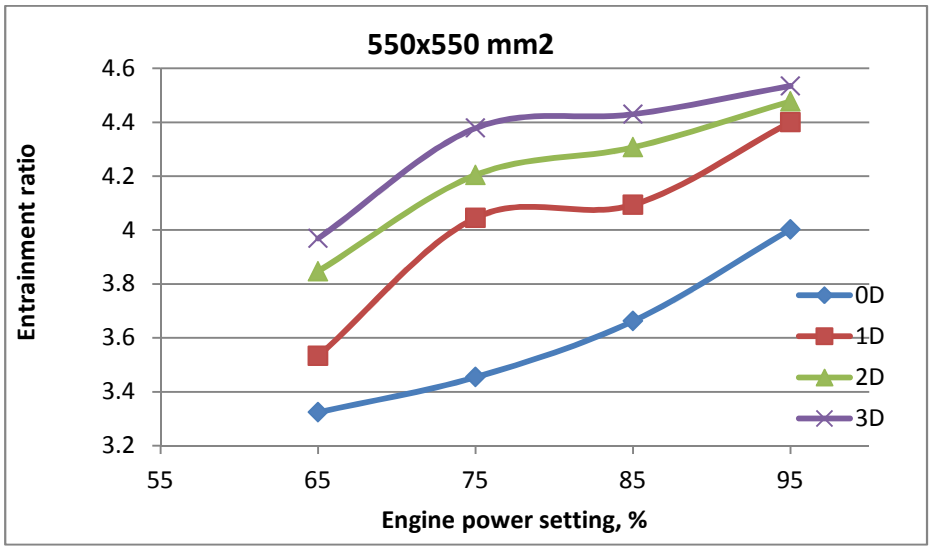

Figure 3.16 Test cell total air mass flow

The magnitude of secondary flow is driven by the low static pressure in the region of the detuner entry. Consequently the static pressure at the detuner entry will decrease hence more secondary air flow will entrained. Whilst this static pressure was not measured, the lower its value the higher is the entrainment ratio for all detuner to engine distances. Figure 3.16 clearly shows that increasing the engine power setting will increase the primary air flow, reduce its static pressure and enhance the entrainment ratio.

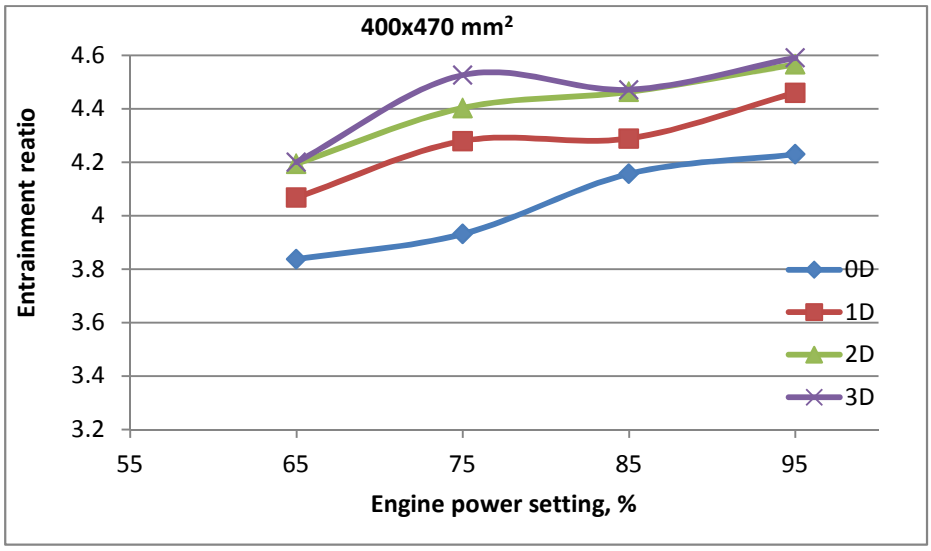

Figure 3.17 Test cell total air mass flow

Figure 3.17 shows the same increase in trend lines with respect to power settings. Decreasing the test cell diameter leads to an increase in velocity of the secondary air flow therefore the static pressure difference between the detuner entry and upstream the test cell will increase. Hence entrainment of secondary air flow simultaneously increases. This time the increment in entrainment ratio is more because of the more losses that secondary flow experience due to the decrease in test cell size

3.5.1. Effect of Nozzle - Detuner Separation Distance on Entrainment Ratio

The effect of engine nozzle - detuner separation distance on the entrainment ratio for each test cell are shown in Figure 3.18 to Figure 3.20 The entrainment ratio increases with nozzle - detuner separation distance, initially relatively rapidly up to a certain distance and then the effect decreases. This effect is explained as due to the presence of the engine blocking the area available for secondary air to be induced. For a given nozzle to detuner separation distance the entrainment ratio increases with engine power setting. Decreasing the distance between engine nozzle to detuner leads to an increase in velocity of the secondary air flow therefore the static pressure difference between the detuner entry and upstream the test cell will increase. Hence entrainment of secondary air flow simultaneously increases.

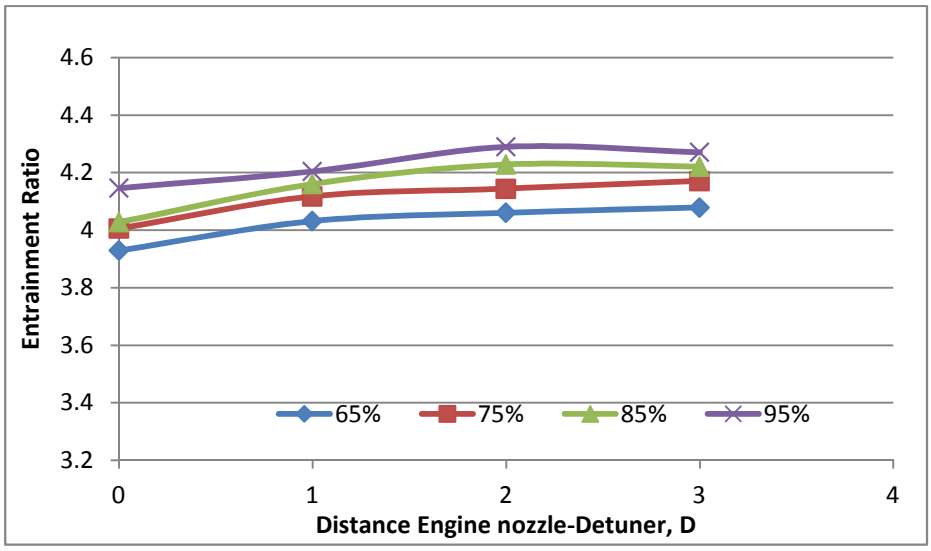

Figure 3.18 Entrainment ratio with nozzle - detuner separation distance variation (700x700)

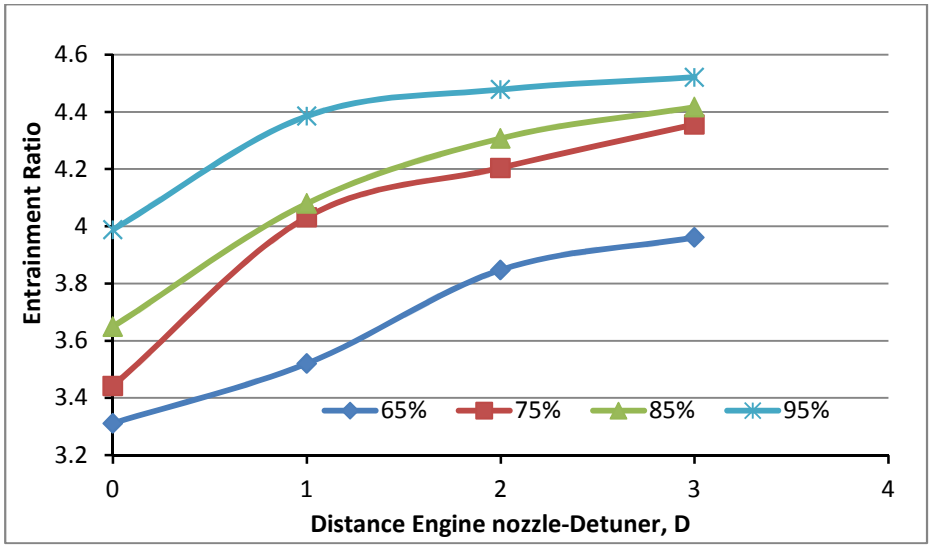

Figure 3.19 Entrainment ratio with nozzle - detuner separation distance (550x550)

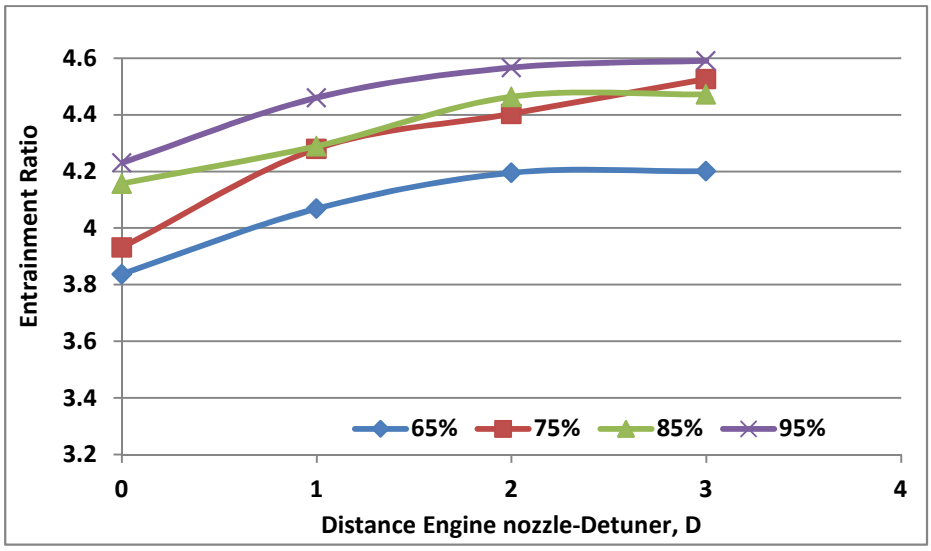

Figure 3.20 Entrainment ratio with nozzle - detuner separation distance (400x470)

3.5.2. Thrust correction factor

The load cells thrust measurement, intake momentum drag and cradle drag were calculated. Intake momentum drag was estimated by measuring the engine air flow approach velocity at reference 2. The Rolls-Royce First Principle approach was used to compute the cradle drag. The flow velocity near the frontal blockage areas of the cradle's moving part was measured, see Figure 3.13. The cradle drag was computed by using Equation (2.10) after calculating the pressure load using Equation (2.9).

However, Instrumentation limitations due to installation difficulties and cost prevent the estimation of some correction factors such as the bellmouth force where there is a need to define the stagnation point on the bellmouth surface. Also the drag coefficient of the external part of the bellmouth was not considered in the determination because it needed a lengthy and expensive experimental set up.

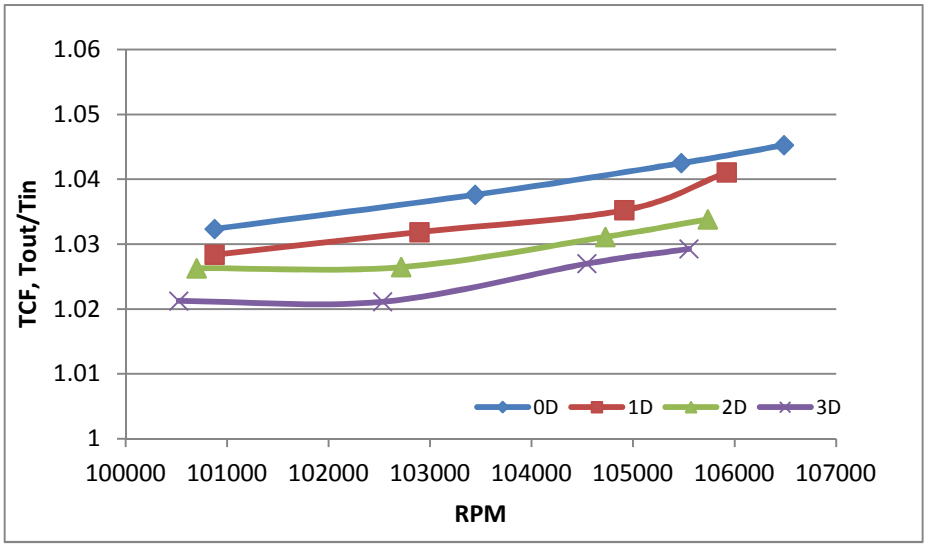

Figure 3.21 Thrust correction factor as a function of RPM (Test Cell: 700x700)

The thrust was measured by the two load cells and the engine rotational speed was given by the engine ECU. The tests were conducted over several days and measured data was corrected to ISA day condition before any comparisons were made. An outdoor test was conducted to do back to back thrust analyses. For the purpose of comparing the experimental to computational results the thrust ratio of the outdoor to the indoor is known to be the thrust correction factor. Two sets of measurements were taken: one set indoors and one set outdoors, and that the thrust correction factor was the ratio of those two measurements. The TCF of 700x700 test cell is shown in Figure 3.21, which shows that the TCF increases more or less linearly with engine speed. The thrust correction factor decreases with nozzle - detuner separation distance. The two other configurations give similar trend lines with different gradients as shown in Figure 3.22 and Figure 3.23.

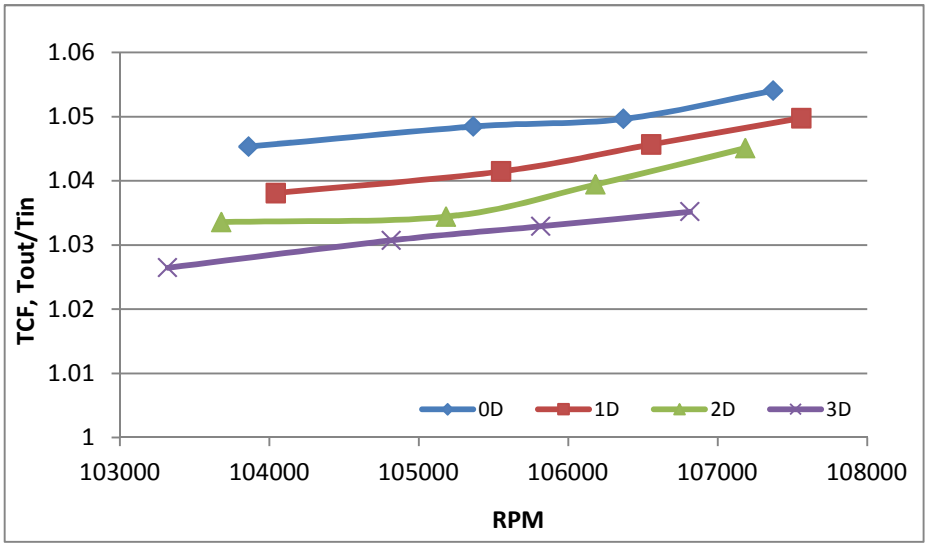

Figure 3.22 Thrust correction factor as a function of RPM (Test Cell: 550x550)

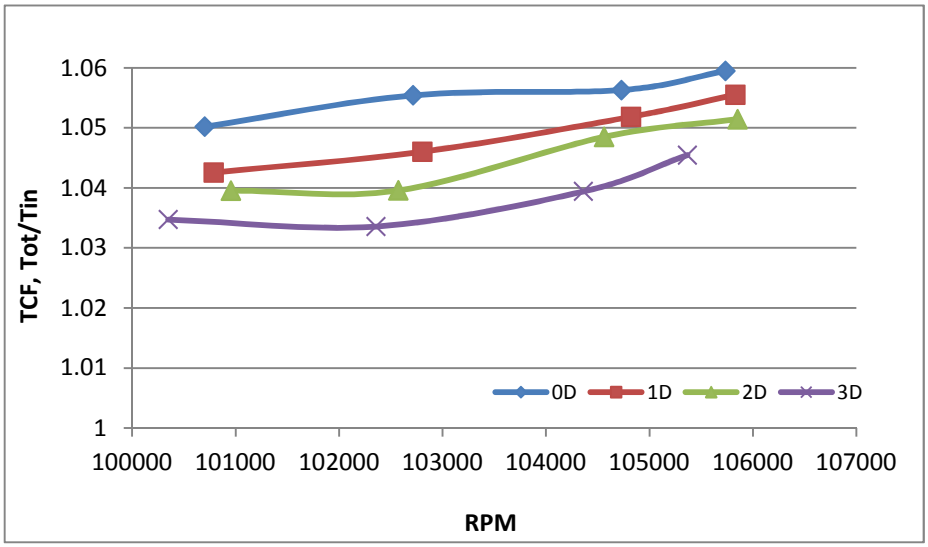

Figure 3.23 Thrust correction factor as a function of RPM (Test Cell: 400x470)

Comparison of Figure 3.21 to Figure 3.23 shows that the magnitude of the TCF was different for each of the three configurations. Therefore a correction for the effect of test cell size on the measured TCF is possible. Figure 3.24 to Figure 3.27 show the effect of changing test cell cross-section area on the TCF for the four nozzle - detuner separation distances used. In all four figures, configuration 400x470 has the highest thrust correction factor and the TCF decreases as the test cell cross-sectional area increases. A possible explanation could be that because the TCF includes the intake momentum drag, increasing the test cell secondary air flow velocity by reducing the cross-sectional area of the detuner for the same engine mass flow will tend to increase

the intake momentum drag. Similarly increasing the test cell cross-sectional area infinitely leads to freer air conditions and the TCF decreases.

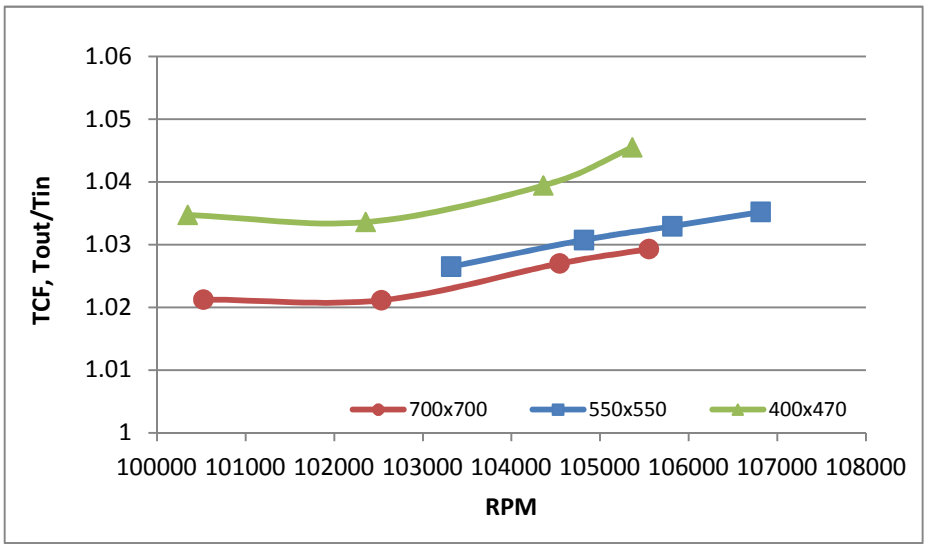

Figure 3.24 Thrust correction factor (nozzle-detuner separation distance: 3d)

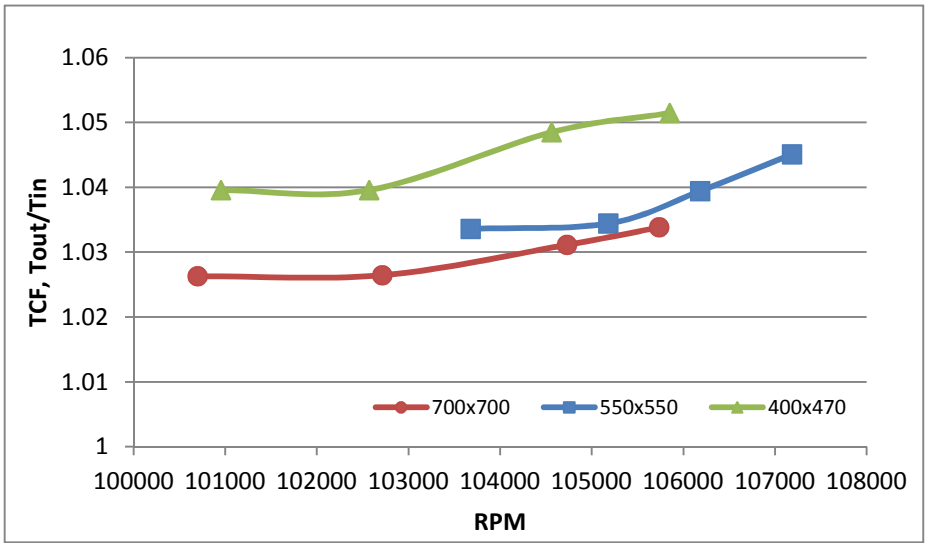

Figure 3.25 Thrust correction factor (nozzle-detuner separation distance: 2d)

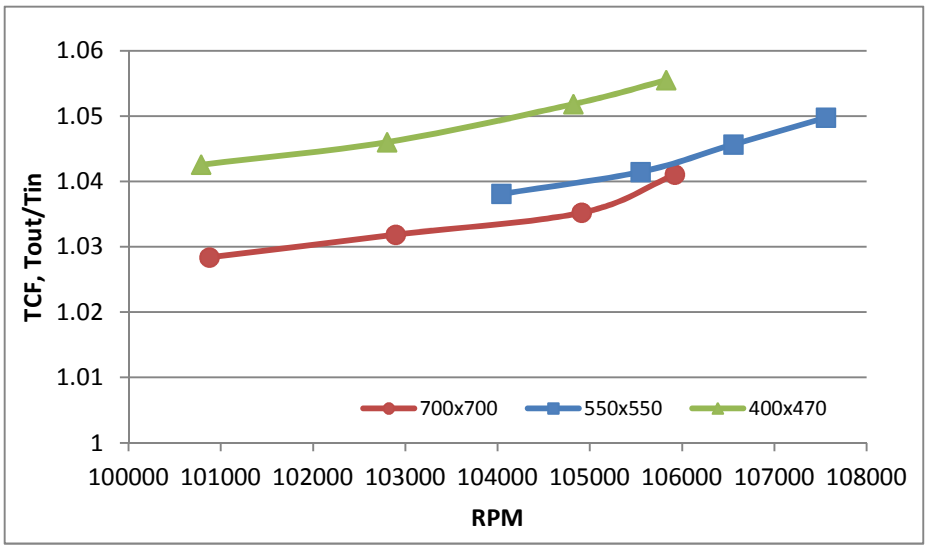

Figure 3.26 Thrust correction factor (nozzle-detuner separation distance: 1d)

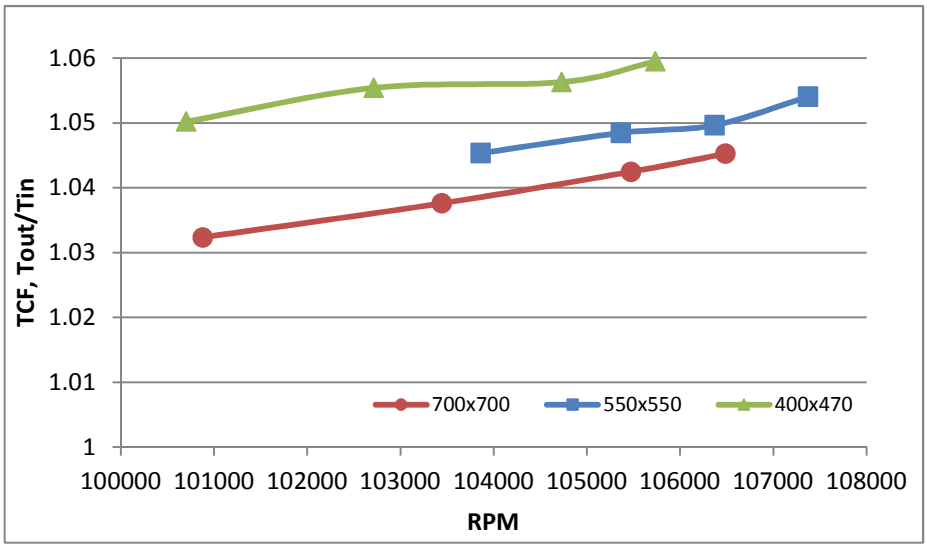

Figure 3.27 Thrust correction factor (nozzle-detuner separation distance: 0d)

The separation distance between the engine nozzle and the detuner influences the amount of the secondary air entering the test cell as well as the air flow velocity patterns inside the test cell. Figure 3.28 to Figure 3.31 show the effect of the engine to detuner separation distance on the TCF for the four engine power settings. As would be expected from the results presented above, the TCF decreases with the engine nozzle - detuner separation distance for each engine power setting.

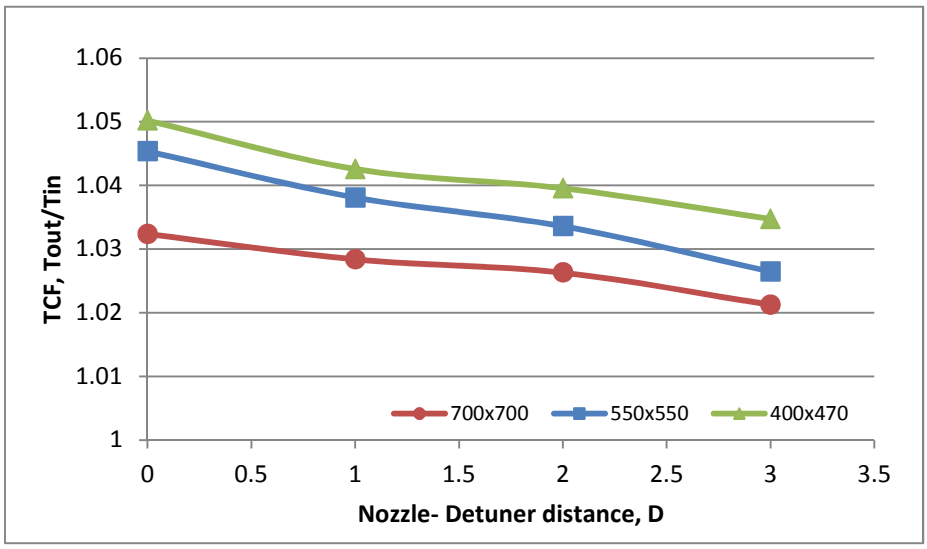

Figure 3.28 Thrust correction factor as a function of nozzle-detuner separation distance (engine power setting: 65%)

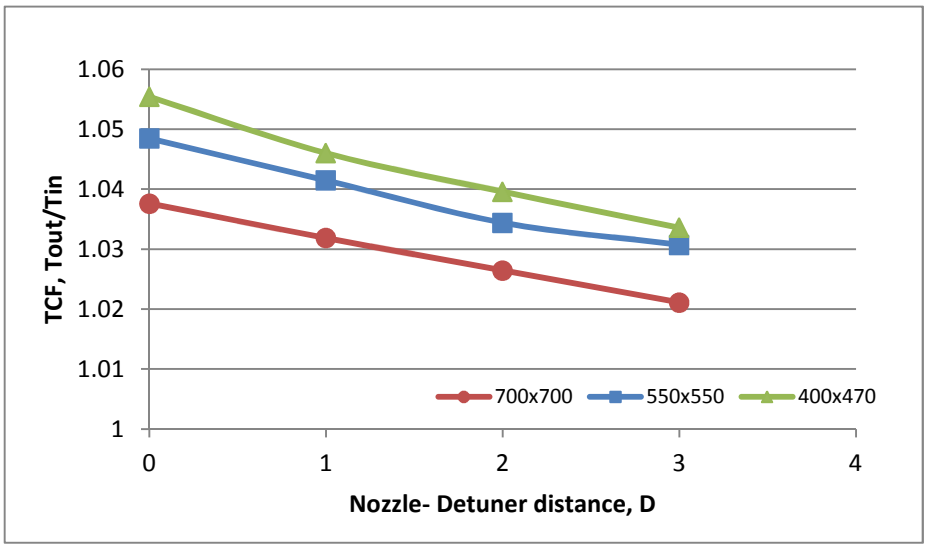

Figure 3.29 Thrust correction factor as a function of nozzle-detuner separation distance (engine power setting: 75%)

In summary the thrust correction factor decreases with the position of engine nozzle to detuner. However it increases as the engine test cell dimensions decrease. Figure 3.27 to Figure 3.29 show that only a little effect of engine power setting on thrust correction and trends are similar for all test cells.

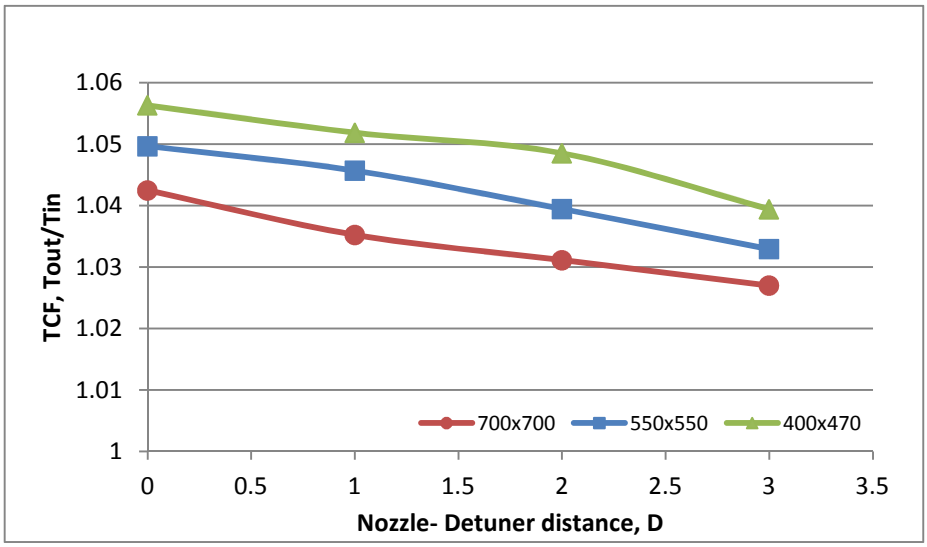

Figure 3.30 Thrust correction factor as a function of nozzle-detuner separation distance (engine power setting: 85%)

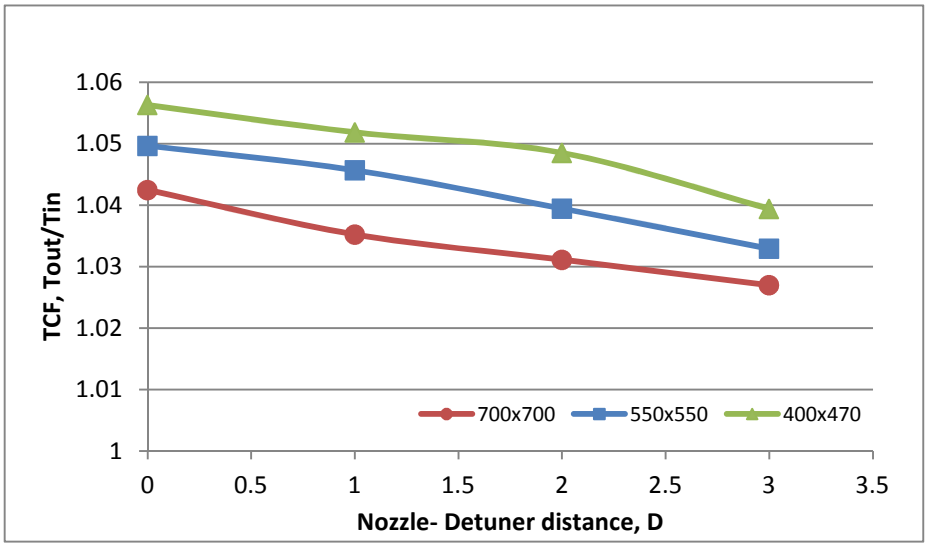

Figure 3.31 Thrust correction factor as a function of nozzle-detuner separation distance (engine power setting: 95%)

It was possible to determine only the intake momentum drag, cradle drag and base drag correction factors due to instrumentation limitations. However, intake momentum drag is the largest thrust correction factor, as reported in the published literature. The intake momentum drag is the product of the engine approach velocity and the engine throat mass flow. The average of the velocity measurements at the four points at reference 2 gives the mean approach velocity and the engine throat velocity is computed using the measured static pressure depression and the theory of compressible flow.

Figure 3.32 shows the calculated intake momentum drag for the four engine power settings for different nozzle - detuner separation distances. For a given engine power setting the intake momentum drag increases with nozzle - detuner separation distance. This could be related to the increase in the cell total air mass flow and the secondary air velocity.

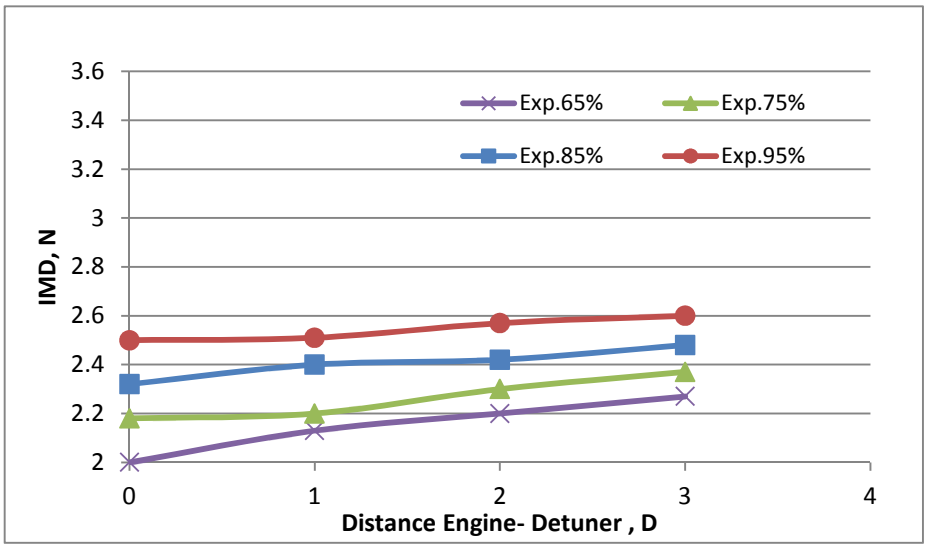

Figure 3.32 Intake momentum drag for 700x700 test cell as a function of nozzle-detuner separation distance

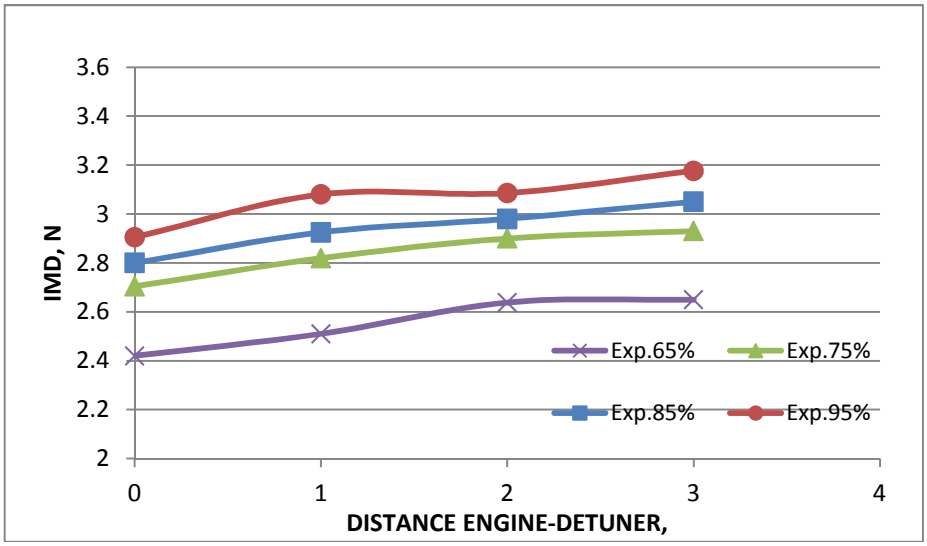

Figure 3.33 Intake momentum drag for 550x550 test cell as a function of nozzle-detuner separation distance

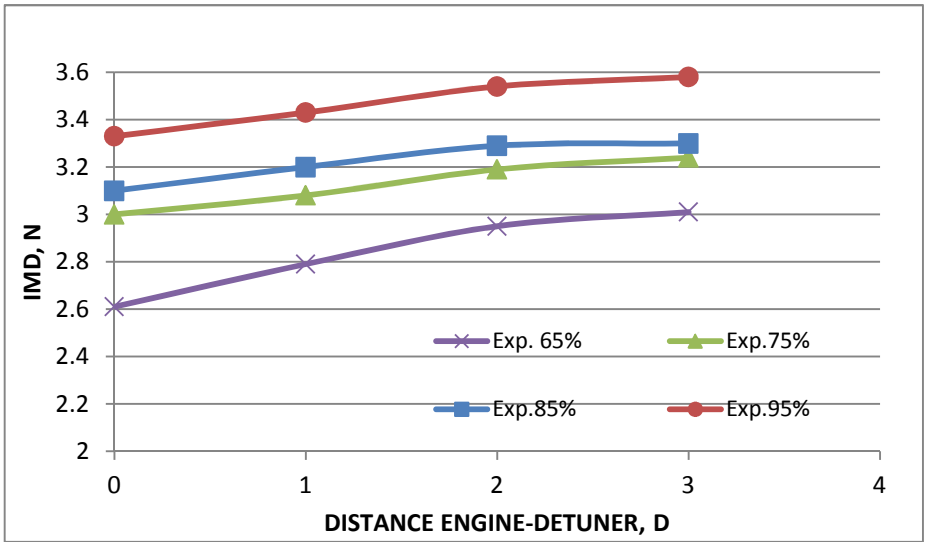

Figure 3.34 Intake momentum drag for 400x470 test cell as a function of nozzle-detuner separation distance

The intake momentum drag has been found to be the largest thrust correction factor. It increases with the engine-detuner gap. This is related to the entrainment ratio since increasing the gap causes the total mass flow going through the cell to increase. In addition, for the same cell dimension, the free stream velocity increases. It was shown hat the intake momentum drag follows the entrainment ratio trend. It increase with engine power setting. Since decreasing test cell size increases the flow velocity. Intake momentum drag increases as the test cell size decreases.

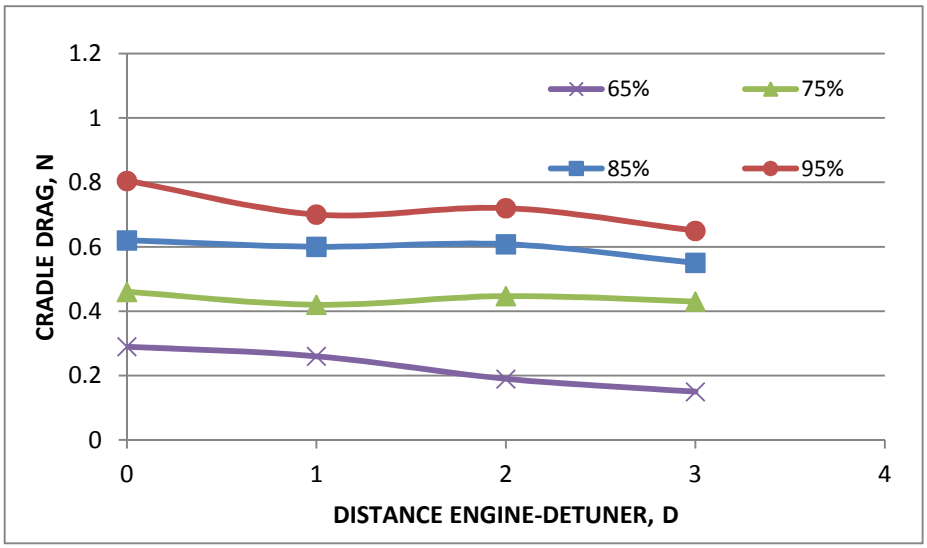

Figure 3.35 Cradle drag as a function of nozzle-detuner separation distance (Test cell: 700x700)

The Rolls-Royce First Principle approach has been used to compute the cradle drag. The airflow velocity near the frontal blockage areas of the moving part of cradle is measured, see Figure 3.13. The pressure load is computed by using Equation (2.9) and the cradle drag is computed using Equation (2.10).

The velocity in front of the cradle is taken as the velocity average of the nine points shown in Figure 3.13. The density is computed assuming ideal gas and knowing that the cradle drag coefficient (Cd) is 1.79. Figure 3.35 to Figure 3.37 show the computed cradle drag with nozzle-detuner separation distance for the test cells. The cradle drag generally decreases with distance between nozzle and detuner, but with some variations (see 65% power 500x500 and 95% power 400x470). The general trend can be related to the increase of ejector pump effect as the nozzle-detuner separation decreases. The ejector pump effect will affect the velocity profile around the cradle and consequently the cradle drag. It should also be noted that the cradle drag increases with engine power settings.

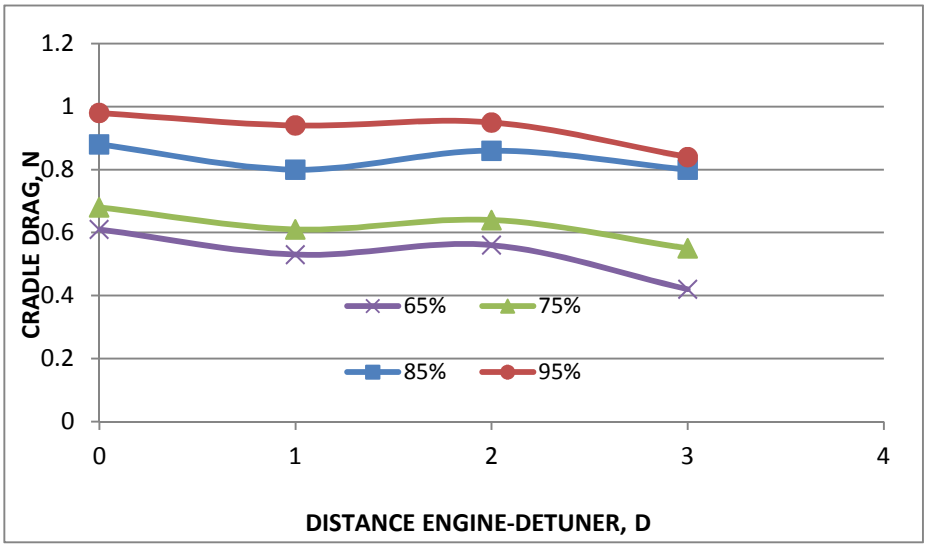

Figure 3.36 Cradle drag as a function of nozzle-detuner separation distance (Test cell: 550x550)

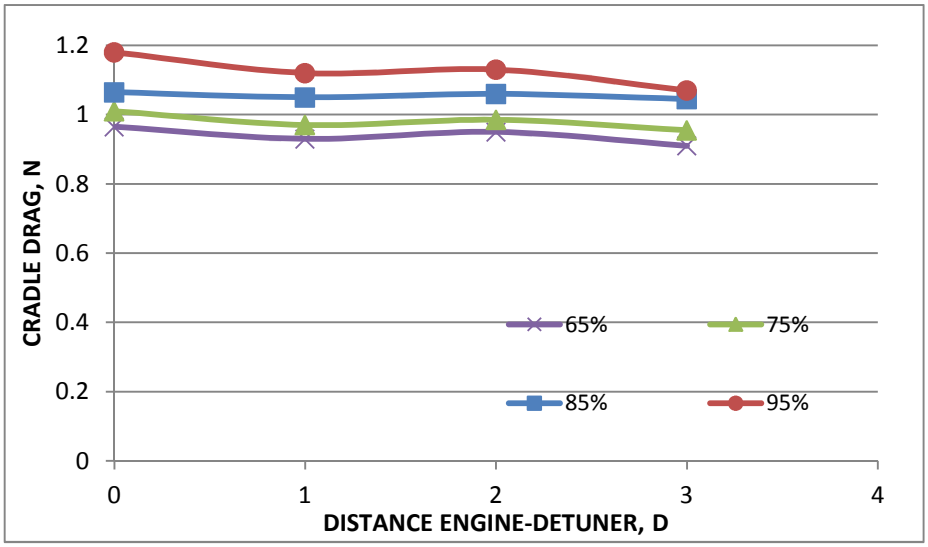

Figure 3.37 Cradle drag as a function of nozzle-detuner separation distance (Test cell: 400x470)

Cradle drag is caused by the secondary cell flow impinging on the floating part of the cradle and on all those obstructions attached on it. The cradle drag increases as the gap engine-detuner decreases. For small distances between the engine nozzle and detuner the ejector pump effect influences the velocity around the cradle. Indeed, the secondary flow entering the detuner experiences an acceleration which can be felt also by the flow around the cradle if the exhaust collector is close to the engine stand. Results show also that there is a detuner position which gives rise to a minimum cradle drag. This is probably due to a balance between the entrainment flow and the ejector pump effect which accelerates the flow around the cradle.

The static pressure around the engine nozzle was measured by four static pressure probes in order to estimate the base force acting on the engine after-body. From such measurements are the depression generated around the engine after-body can be estimated. As mentioned before that the high temperature at the nozzle exit plane does not allow the probes to be set there. Therefore, they have been located at 8 mm, 18 mm, 28 mm and 38 mm downstream of the nozzle exit plane, see Figure 3.12.

The base drag was estimated using equation **(**2.11). Figure 3.38 to Figure 3.40 show the base drag in each test cell. It should be noted that the base drag magnitude increases as the test cell cross section decreases due to the increase in the depression region around the engine nozzle. The base drag increases with the engine power setting. The

depression around the engine nozzle decreases with the engine to detuner distance and consequently the base drag decreases.

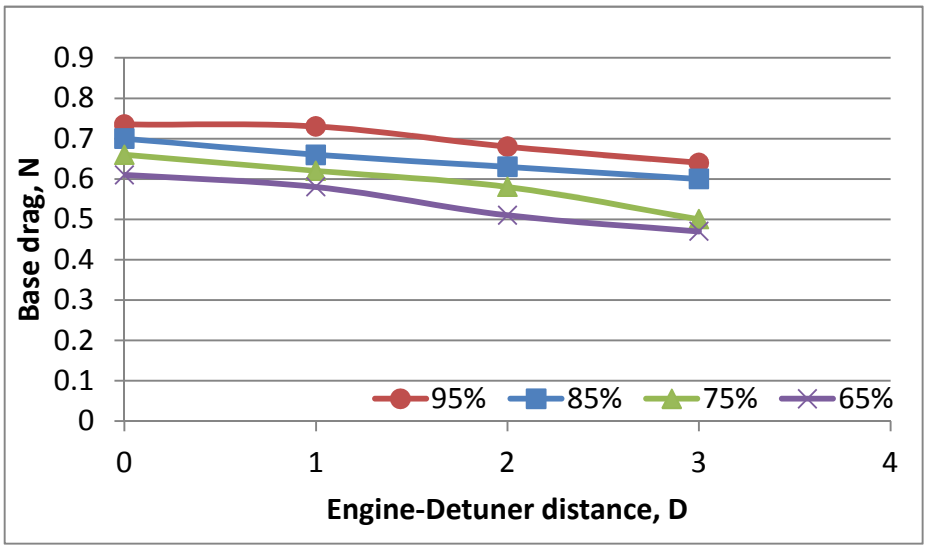

Figure 3.38 Base drag as a function of nozzle-detuner separation distance (Test cell: 700x700)

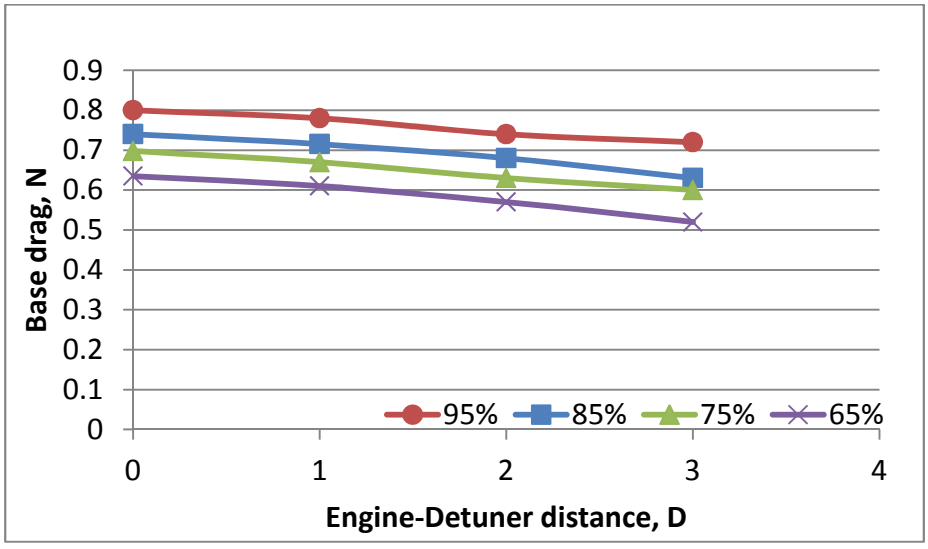

Figure 3.39 Base drag as a function of nozzle-detuner separation distance (Test cell: 550x550)

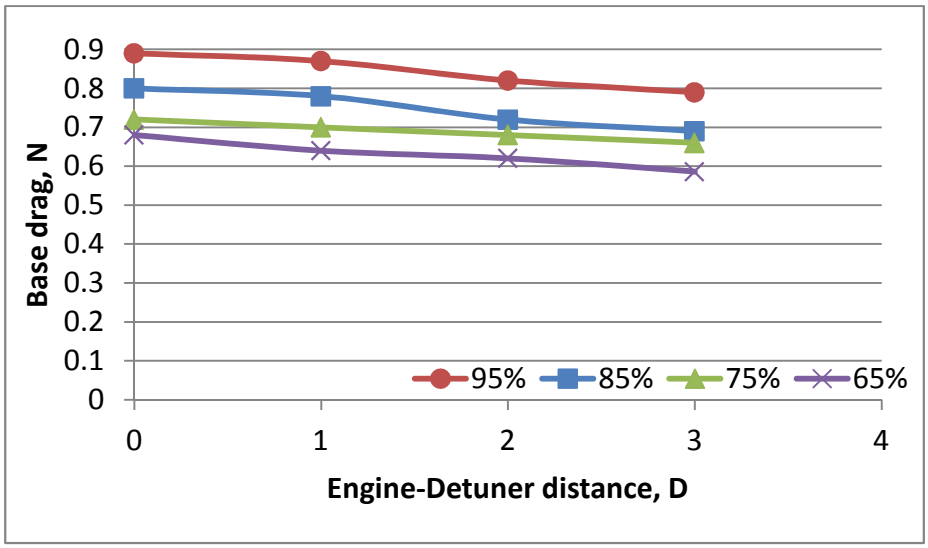

Figure 3.40 Base drag as a function of nozzle-detuner separation distance (Test cell: 400x470)

When the engine nozzle is in the same plane as the detuner inlet, the base drag is one order of magnitude higher. There is a higher degree of depression (the static pressure field around the engine nozzle) when the engine is set closer to the detuner. The depression around the engine nozzle increases as the test cell dimensions decrease.

4. Computational Fluid Dynamics Approach

The development of computational fluid dynamics nowadays becomes substantial. Due to the ever decreasing cost and exponential improvement of computing power and resources over this time, CFD has become commonly accepted by the engineering community as a capable and useful tool in the prediction and validation of fluid flow problems.

Determination of thrust correction factors experimentally is extremely time consuming and expensive whereby, complicated measurement equipment and processes are required to achieve acceptable results. Therefore, CFD has become extremely attractive to the engine manufacturer to incorporate its technological benefits to thrust measurement in test facilities to decrease the amount of required experimental work to determine thrust correction factors.

This chapter presents the use of CFD for the estimation of thrust correction factors. The CFD approach has been used to derive thrust correction factors which are not experimentally measurable. The software used for the CFD analysis is Fluent and user manual provides a complete description of how the software works and gives also a description of the possible computational choices available.

The aim of the CFD analysis in this work is to derive the thrust correction factor and to explore the flow fields inside the test cell in order to work out useful outcomes for their global understanding. The CFD analysis has been used for validating the findings arising from the experimental work results illustrated in chapter 3.

	0D	1D	2D	3D
65%	**X**			**X**
75%		**X**		
75%			**X**	
95%	**X**			**X**

Table 4.1 Experiments cases modelled by CFD

The full dimensions of the indoor test cells are described in chapter 3 on Figure 3.1. The proposed work is to analysis 48 cases which is a very big number and takes a very long time to model in CFD. Due to the limited time, a selective approach has been chosen to select 16 cases only to re-simulate and analyse which mostly give a general picture of all tested parameters as shown in Table 4.1. It is recommended in the future work to consider all cases together.

Two parameters, the accuracy of the result and the time for performing the simulation, are usually considered in generating a model. The accuracy relies on selecting the volume discretization and the turbulence model for solving it (Fluent incorporated). It is directly proportional to the number of cells as believed. This is for sure will increase the simulation time and for that reason it is obviously practical to refine the mesh just in the areas of interest which as a result implies an increase in the uncertainty. This means that there is a compromise in each case of modelling between the time and accuracy is valid.

Figure 4.1 shows the layout of the test cell produced by gambit. The air enters the test cell axially through a bellmouth. The engine on the cradle is located just right in front of the detune. All sizes and dimensions are same to that for the test cells used in the experiments.

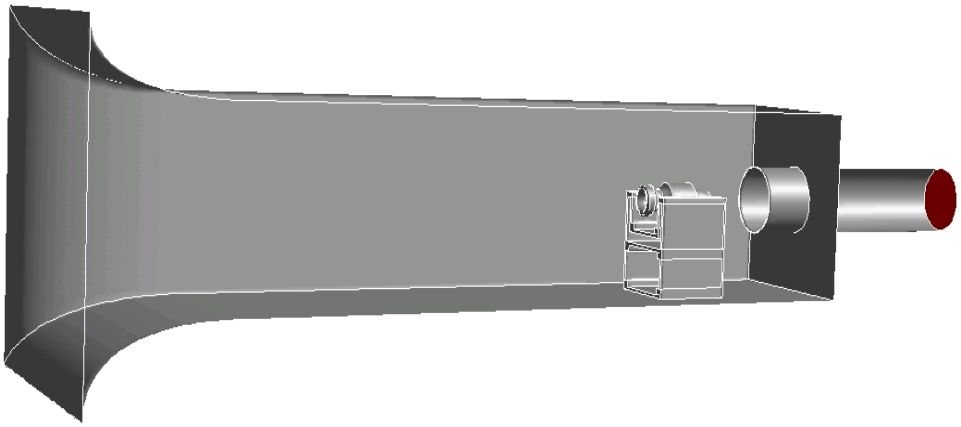

Figure 4.1 Test cell model for 700 mm x 700 mm cross section

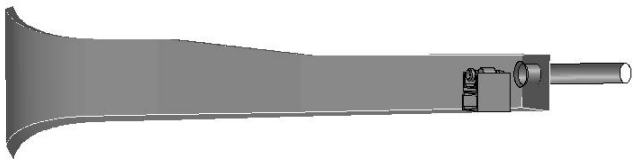

Figure 4.2 Test cell model for 550 mm x 550 mm cross section

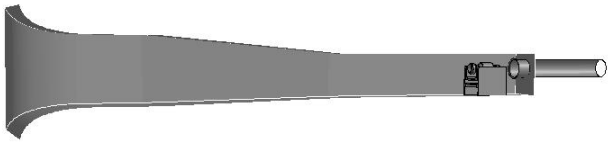

Figure 4.3 Test cell model for 400 mm x 470 mm cross section

The aim now is to find a matching process to enable the computational solution to be matched with the experimentally measured entrainment ratio. Accordingly the static pressure at the exit of the detuner is used as a handle parameter to match the cell mass flow to that in the experiment.

The total mass flow can be split into two parts; the primary one which is going directly into the engine and the secondary flow which is going around the engine and driven by the engine-detuner ejector pump effect. The engine primary flow is driven by the static conditions at the engine face (assuming that the conditions at the cell inlet are fixed) and the secondary flow is defined by the static pressure at the exit of the detuner. Therefore by varying the static pressure at the exit of the detuner the total mass flow is changes. This step is repeated until the same cell entrainment ratio as that experimentally measured is achieved. If the cell entrainment ratio is matched, many flow similarities between the real case and the simulation can also be captured and

thrust correction factors can be examined. Therefore if the computational geometry is similar to the actual geometry and the mass flow is the same, the gauge pressure distributions on the surfaces will also be very close.

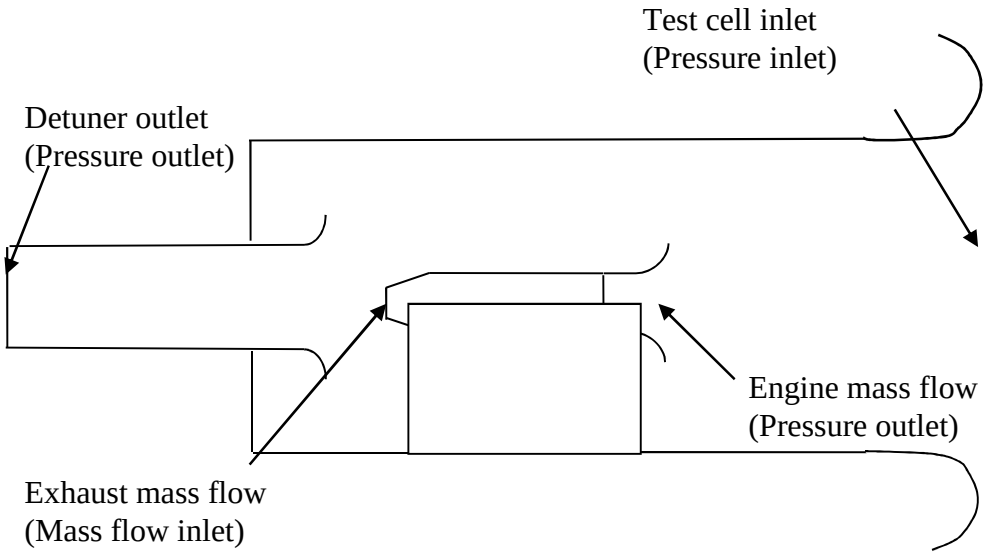

Figure 4.4 Boundary conditions for CFD model

4.1. Geometry And Grid Generation

The first step in the CFD simulation is to model the test cell and generate the appropriate mesh for each geometry. Gambit which is a compatible tool with Fluent was used to build the geometry and to generate the mesh. There are four different test cell configurations to be modelled for the simulation. Each test cell have three different distances between the engine and detuner. Basic dimensions for the test cells are provided in chapter 3.

The primary air of the engine is delivered through a bellmouth. The front view of the bellmouth is shown in Figure 4.5. The dimensions of the bellmouth is given in installation manual given by Rolls Royce (Rolls Royce, 2003).

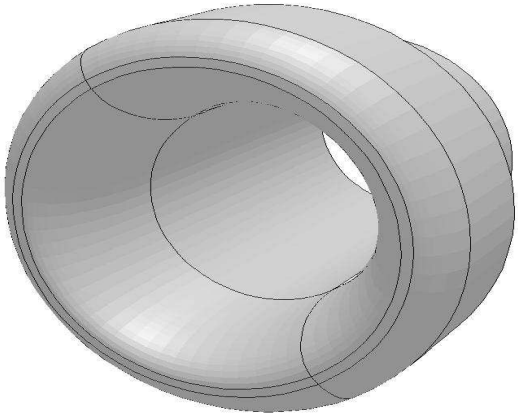

Figure 4.5 Engine bellmouth, front view

The cradle and the engine on the cradle are illustrated in Figure 4.6 and Figure 4.7 respectively. The cradle dimensions are provided by Rolls Royce (Rolls Royce, 2003). The cradle has movable and fixed parts. The cradle is fixed on the floor of the test cell.

Several attempts have been made to mesh the nine models. Since bellmouth, engine, cradle, and detuner are the same for all models the target was to keep the same mesh over all simulations. Due to the large number of models more than one kind of mesh scheme has been used. For most of parts of the cell hexahedral elements have been tried. Hexahedral elements can map in a lower number of elements an entire volume more regularly than tetrahedral cells (Fluent incorporated).

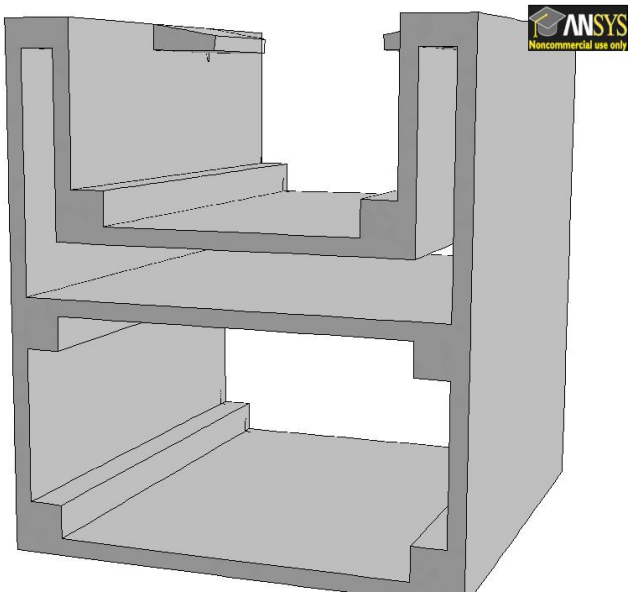

Figure 4.6 Cradle front view

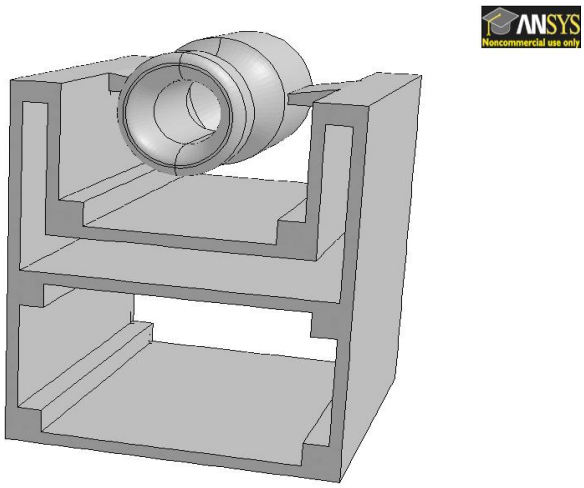

Figure 4.7 Engine on cradle

In most parts of the test cell flow paths are straight without any obstacle where the mesh has hexahedral cells. Hexahedral mesh structure will speed up the simulation compared to the tetrahedral (Fluent incorporated). The cylindrical shape of the detuner leads to use a cooper meshing scheme (Fluent incorporated) which was kept the same for all simulated models. In some preliminary simulations unwanted flow phenomena were observed around detuner.

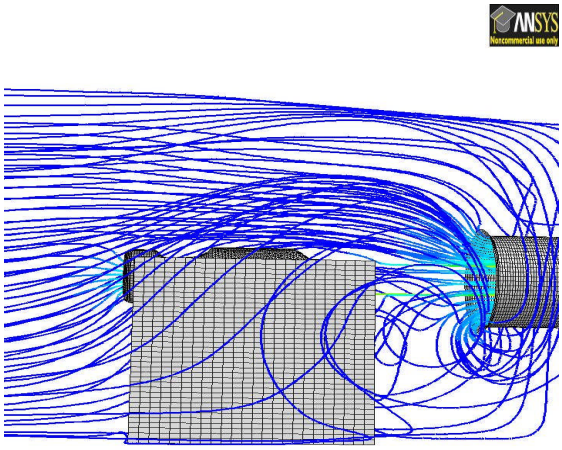

Figure 4.8 Flow separation and recirculation around detuner entry

Many attempts have been made to have a hexahedral mesh structure around the engine and cradle. However Figure 4.8 shows the recirculation and flow separation in that area just around the detuner. The interaction of the ejector pump effect and the cell walls generates some vortices as well. These flow phenomena are discussed earlier in chapter 2. Consequently a tetrahedral mesh structure was used in that part of the test cell.

The volume around the engine and detuner was divided in sub volumes. The mesh structure in volume around the engine bellmouth was hexahedral to enable a correct estimation of bellmouth force. The mixing process of high velocity and temperature of engine exhaust air with the secondary air at the detuner leads solution to diverge. Therefore the volume have fine mesh with a hexahedral cells structure. This approach minimise the size of the mesh and consequently the time of simulation while the areas of interest have a fine structure mesh.

The engine bellmouth force estimation is accurately needed. Therefore, the mesh around the bellmouth should have fine structure mesh. The accuracy of calculation is not only related to the mesh density but also the shape of cells. Several volumes have been generated around the bellmouth. The grid density for these volumes is different and their density decreases as the elements get further from the wall surface. This approach gives the possibility to control the mesh density in each volume independently. It is sometimes useful to adapt cells where it is needed after solution

convergence without affecting other areas. Cell adaptation depends on the shape of original elements. The same approach has been used in the areas around engine nozzle and in detuner entry.

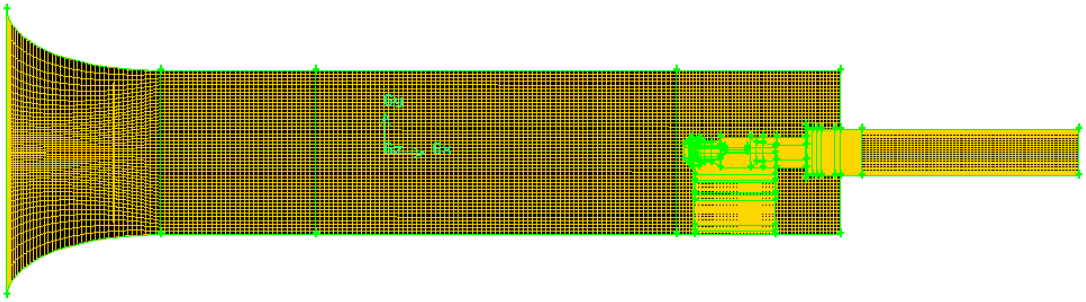

Figure 4.9 Mesh overview for the test cell

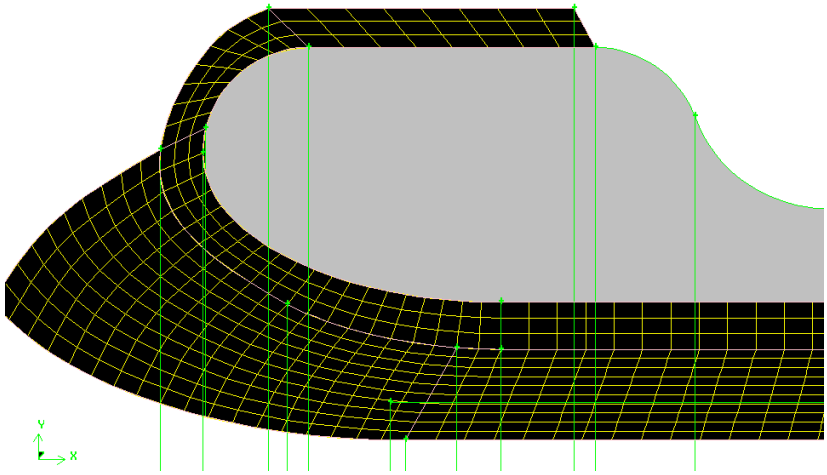

Figure 4.10 Grid structure around the engine bellmouth

The overview of the mesh for the entire test cell is shown in Figure 4.9. Figure 4.10 shows the mesh in details of the volumes inside and around the bellmouth. The mesh structure of the bellmouth has been kept the same for all models for consistency purpose.

4.1 Boundary Conditions

The cell inlet boundary condition is Pressure Inlet which uses the total pressure as main input parameter (Fluent incorporated). This parameter is experimentally measured inside the cell.

Indeed, some of the total mass flow which enters the cell is sucked by the engine. The engine draws the primary flow; air necessary for its cycle. An additional amount of air enters the cell; secondary flow, as a consequence of the ejector pump effect take place because of the interaction between the engine and detuner.

The boundary condition at the engine inlet was set as pressure outlet as fluent does not use any mass flow outlet boundary conditions. The parameter used for this boundary condition is the static pressure which is computed from static pressure drop. The static pressure depression was experimentally measured where the static pressure has been derived by using isentropic compressible flow relationships. This was sit as a starting input value and after every simulation the value has to be re adjusted to match the real mass flow.

The boundary conditions on Fluent do not use mass flow outlet boundary but use the mass flow inlet. So the same mass flow entered the engine has to exit the engine nozzle add the fuel mass flow. Therefore, mass flow inlet boundary condition has been selected. The boundary condition at the detuner outlet has been represented as the handle parameter of a trial procedure to match the actual cell entrainment ratio The influence of the value of the static pressure at the detuner exit on the cell mass flow is vital. That is because the dependence of the forces acting on the cradle on the entrainment ratio.

4.2 Fluent Settings

Mainly Fluent has three kinds of solvers; Segregated, Coupled Implicit and Coupled Explicit (Fluent incorporated). These solvers are valid for a broad range of flows. The Coupled solver is preferable for the compressible flow applications (Fluent incorporated). The Segregated solver was used in this set of simulations.

The choice of turbulence model depends on the level of accuracy required, the available computational resources, and the amount of time available for the simulation. The Reynolds Average Navier-Stokes (RANS) equations model has been chosen for the turbulence model. This model reduces the computational effort quite a lot and

compared to others account only for the mean flow quantities including all scales of turbulence.

Boussinesq approach is offered by Fluent for solving the governing equations with RANS (Fluent incorporated). The Boussinesq hypothesis performs well for industrial flows. The standard k-epsilon is a two-equation turbulence model in FLUENT was proposed by Launder and Spalding (Launder, B. et. al. 1972). The standard k-epsilon which uses the Boussineq assumptions has become the workhorse of practical engineering flow calculations. Due to its robustness, economy and reasonable accuracy in terms of turbulence flows it is applicable in many industrial flow. The standard k-ε model is based on model transport equations for the turbulence kinetic energy k and its dissipation rate ε.

The solver used for all simulations was standard segregated K-ε, implicit, steady. The mesh for every model has about one million elements which need a reasonable memory size to solve the governing equations for each discrete volume. The Segregated Solver implies the use of an implicit linearization of the governing equations where each "scalar" equation is solved once a time for all the cells at the same time.

The k-ε models are primarily for turbulent core flows where the flows are far from the walls. The turbulence is seriously affected by the presence of the wall. Fluent suggests Near Wall Treatments to be implemented. The standard Near Wall Treatments approach which is robust and economic in terms of calculation has been chosen.

The validity of the Wall Functions Treatment is linked to the y+ parameter (Fluent incorporated). So an estimation of the y+ has to be made when the simulation has converged. If it is out of the range of validity some grid adaptations has to be made.

4.3 Step-by-Step Approach for the Discretization

The discretization process in fluent converts the governing equations into algebraic equations. The second order scheme of the discretization process is useful for a grid

with tetrahedral cells. This improves the accuracy of the solution for this calculation (Fluent incorporated).

The discretization process involves the momentum, the continuity, kinetic turbulence, the turbulence dissipation and the energy equations. The momentum and the continuity equations are the most equations to be discretized.

A step-by-step approach is used to help in convergence. Firstly the model uses first order for all the terms until it converges. Secondly pressure, density and momentum equations are changed to second order and the model is allowed to run until it converges. Thirdly the two turbulence equations are changed to second order. After it converges the energy equation is changed to the second order and the model is run until it converges

The convergence occurs when the residual of continuity, x velocity, y velocity, z velocity, k and ε reaches 0.001 and 0.000001 for the energy. This means that a model has converged when continuity, x velocity, y velocity, z velocity, k and ε residual have reached 0.001 and the energy 0.000001.

4.4 Pre-Entry Force Estimation Methodology

It should be mentioned that before extracting any data the cell entrainment ratio for each model should match the experimentally measured ratio. To confirm that all models has to use the boundary conditions of the engine and cell conditions from the experiments.

Direct calculation of a force acting on a stream tube is not possible in Fluent. The surfaces of a stream tube are not solid and their shape and dimensions are unknown until the simulation has converged. The outline of the pre-entry stream tube is shown in Figure 4.11.

Due to the flow velocity up-stream of the engine the stream tube shape is in suction conditions where the engine mass flow has a larger cross sectional area than the bellmouth. Therefore at the engine bellmouth the stream tube must have a convergent shape to carry the air through the engine.

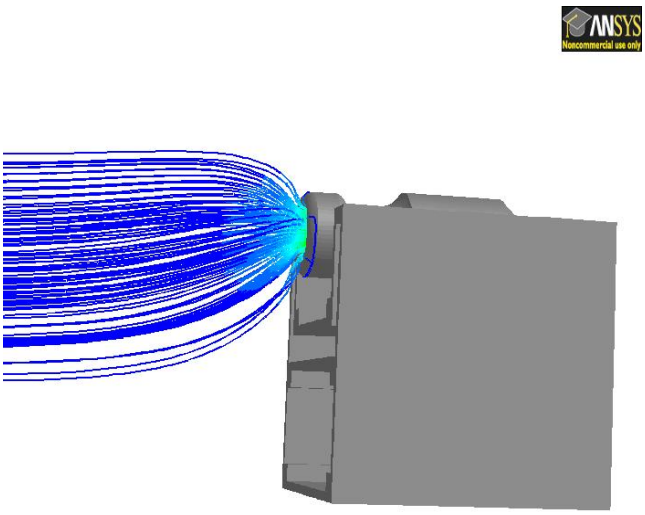

Figure 4.11 Pre-entry stream tube outline

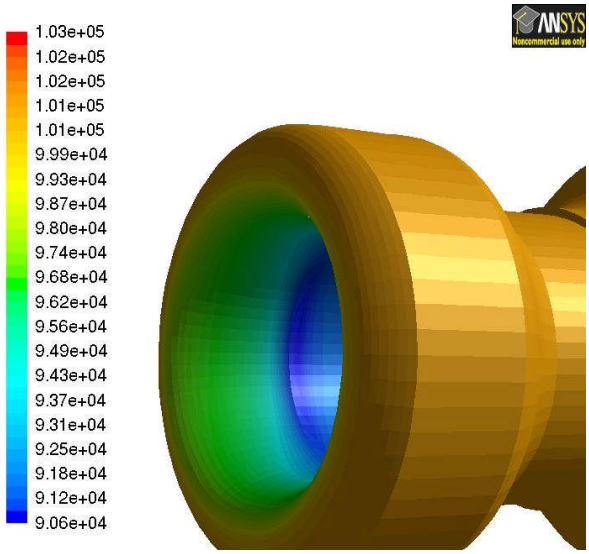

Figure 4.12 Static Pressure Contour of the engine Bellmouth

Stream tubes start from stagnation region on the bellmouth and expand upstream the engine. Therefore the starting point to define the pre-entry stream tube is to spot the stagnation region on the bellmouth surfaces. A generic stagnation region is characterized by an increase of the static pressure on the wall which will match the value of the total pressure (stagnation pressure). Indeed the velocity reduces until it becomes zero on the wall. It has been assumed that each path line belongs to a single longitudinal plane.

The engine mass flow starts to accelerate inside the bellmouth due to the reduction in cross sectional area. Accordingly a static pressure drop takes place inside the bellmouth as shown in Figure 4.12. However the secondary flow diffuses around the outer surfaces of the bellmouth. The stagnation region is where the static pressure has reached the stagnation value where the flow is stationary. This takes place on the bellmouth somewhere between the above mentioned regions.

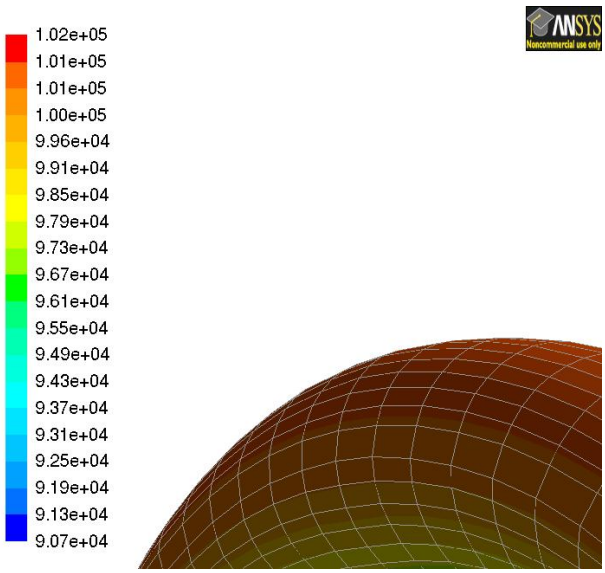

Figure 4.13 Static Pressure Contour with grid around the engine Bellmouth

Figure 4.13 shows the increase of static pressure on the static pressure contour of the outer surfaces of the bellmouth. The grid is used to simply identify the region of peak value.

Once the stagnation region has been identified the flow path lines can be released from these points opposite to the main direction of the flow (Fluent incorporated) as shown in Figure 4.11 above. However flow pathlines could not be released from a single point. Therefore a rake traversing the stagnation point has been generated. The path lines have been released from the rakes shown Figure 4.14.

The geometric and flow parameters for each grid node crossed by each pathline can be extracted in txt files. The pathlines can be plotted in numerical maps to understand which defines the pre-entry stream tube boundary. The same axes which have been

defined in Figure 4.11 are used in this calculations. Flow parameters could be extracted and plotted such as the co-ordinate values which is shown in Figure 4.15.

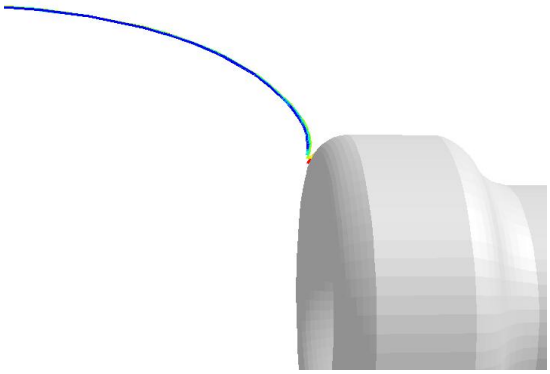

Figure 4.14 Flow Path Lines realised from a Rake

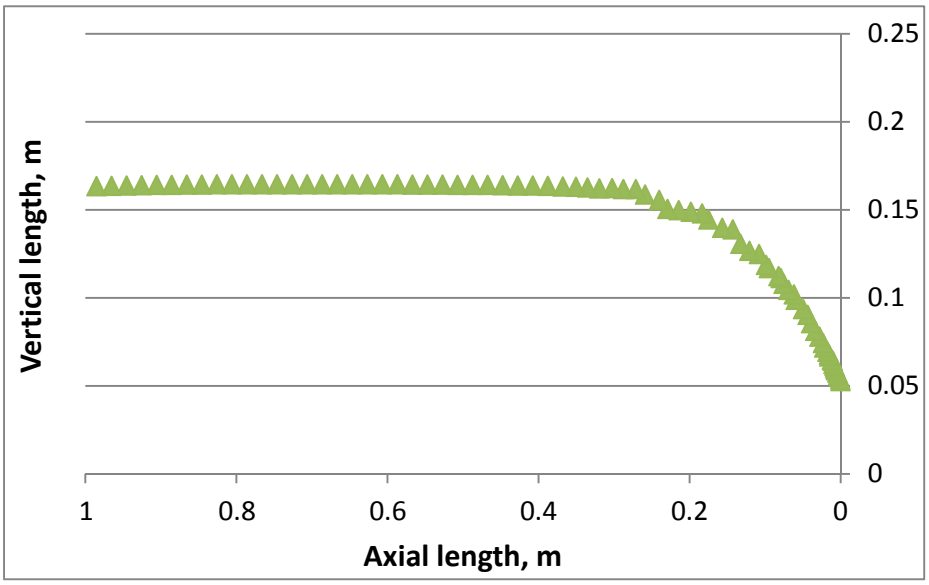

Figure 4.15 Stream Line Coordinate

Indeed in terms of TCF, the axial component of the force acting on the pre-entry stream tube is needed. The discretization of pathlines are the same to that used by Fluent in the calculations. The pathlines were divided in several segments based on its grid nodes as shown in Figure 4.16.

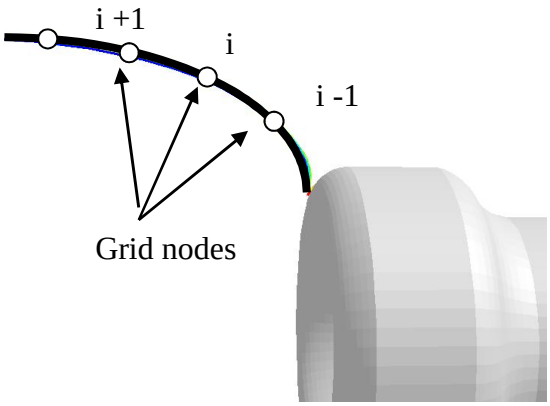

Figure 4.16 Discretization of the Stream Line

The pre-entry force is computed by the integration of static gauge pressure field along the boundary surface of the defined stream tubes.

The assumption was made to have four symmetric stagnation path lines on the bellmouth as shown in Figure 4.17. The static pressure field were extracted from the pathlines which were released from the four different stagnation. The stream tube of each one of the four defined points is related to the pathlines released by that point. The estimation of pre-entry force is the average of the four forces.

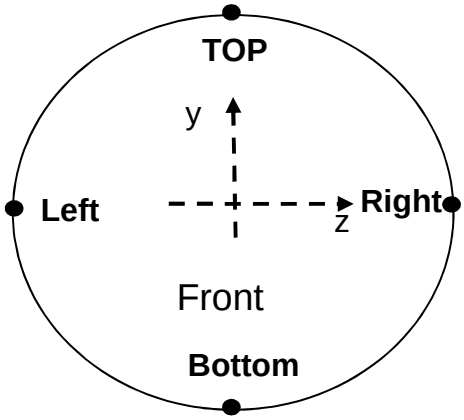

Figure 4.17 Stagnation points the Pre-Entry force

The gauge pre-entry force is defined as the integral of the gauge static pressure along the axially projected area of the stream tube equation (4.1).

$$\phi_{Gpre} = \int_{stream-tube} (p - p_0) dA \qquad \textbf{(4.1)}$$

Figure 4.18 shows the projected area associated with each nodes on a pathline which is defined by equation (4.2).

$$A_i = \left\{ \left[\left(\frac{R_{i+1} - R_i}{2} \right) + R_i \right]^2 - \left[\left(\frac{R_i - R_{i-1}}{2} \right) + R_{i-1} \right]^2 \right\} \pi \qquad \textbf{(4.2)}$$

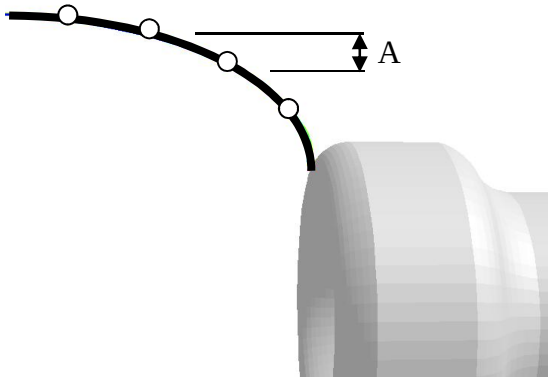

Figure 4.18: Area for each discretization point

The gauge pressure which is associated to A_i is defined as in equation (4.3).

$$p_{Gi} = (p_i - p_0) \qquad \textbf{(4.3)}$$

The reference pressure; p_0 was taken 1m up-stream of engine where there is less flow distortion.

Therefore, the pre-entry force associated with the pathline is represented by equation (4.4)

$$\phi_{Gpre-A} = \sum_{i=1}^{n} \phi_{Gpre-i} = \sum_{i=1}^{n} (p_i - p_0) A_i \qquad \textbf{(4.4)}$$

The procedure was repeated for the four path lines to estimate the total pre-entry force as given by equation (4.5).

$$\phi_{Gpre} = \frac{\sum_{j=A}^{D} \phi_{Gpre-j}}{4} \tag{4.5}$$

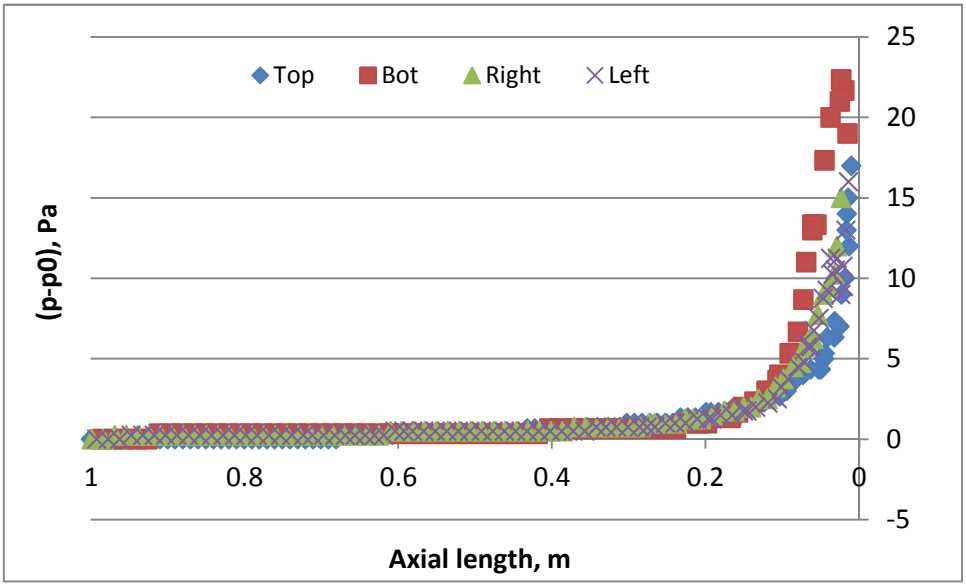

Figure 4.19 Gauge static pressure for the stagnation stream lines

The trends of the gauge static pressure for the four stagnation path lines are shown in Figure 4.19. Correspondingly the radial dimension of pre-entry stream tube are illustrated in Figure 4.20. These illustrations show the convergent shape of the stream tube. Furthermore the static pressure increases as the stream tube cross sectional area reduces until it matches the total pressure at the stagnation point.

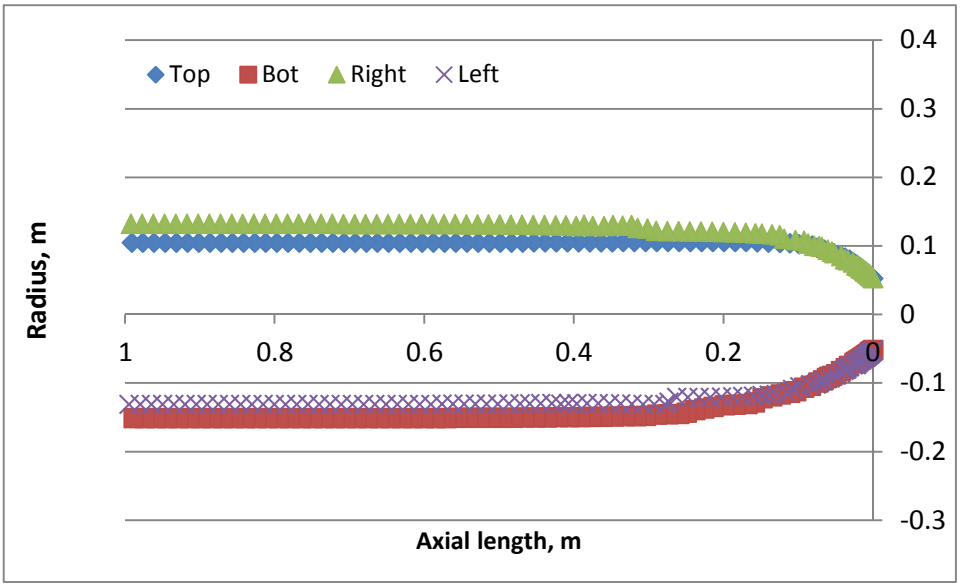

Figure 4.20 Pre-Entry stream tube dimensions

4.5 Bellmouth Force Calculation Methodology

Two different bellmouth gauge forces have to be defined, the external bellmouth force, and the whole bellmouth force. Fluent enables a direct calculation of force (Fluent incorporated).

The stagnation region on the bellmouth has to be defined before the external bellmouth force can be calculated. Therefore, it was assumed from the beginning to divide the bellmouth surface around the stagnation region into several surfaces. Therefore the force of the larger part of the bellmouth can be directly calculated.

However, the part of the bellmouth force which is around the stagnation region can not be calculated directly. Therefore, the values of the static pressure have to be extracted manually. The coordinates of the nodes were also extracted to calculate the projected area. The axial bellmouth force is the only needed component in this calculation.

The gauge static pressure magnitudes have been extracted manually from one side of the bellmouth and afterwards averaged (arithmetically).

$$\phi_{Gbell-lip} = \frac{\sum_{i-1}^{n}(p_i - p_0)}{n} A_{lip} \tag{4.6}$$

where, n is the number of the nodes and A_{lip} represents the bellmouth axial projected area from the known surface up to the stagnation point.

On the other hand the gauge force acting on the entire bellmouth can be calculated directly using the integration tools. It was expected that the force acting on the internal part of the bellmouth is directed in the up-stream direction due to the generated depression and the force acting on the external part of the bellmouth is directed up-stream due to the flow diffusion.

4.6 IMD Calculation by Using CFD

Intake momentum drag is calculated from the measurement of the engine airflow approaching velocity. The velocity was measured one meter upstream of the engine at

the same plane of the reference static pressure. The velocity should be measured before any acceleration into the intake bellmouth occurs. Figure 2.20 shows that the velocity profile at that plane is uniform.

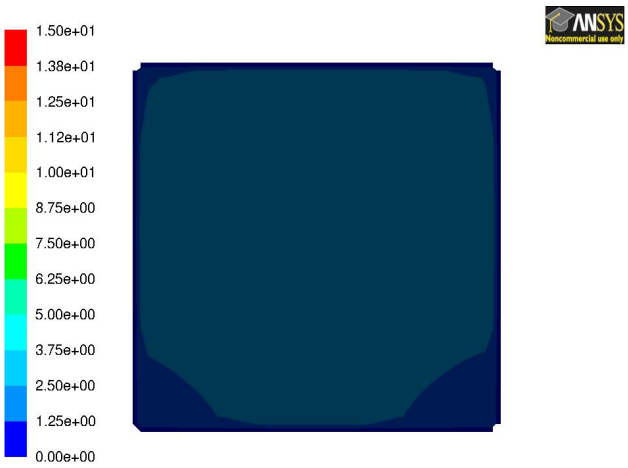

Figure 4.21 : Velocity profile at the reference region, 1m up-stream of the Engine

The velocity can be computed in Fluent by a mass weighted average integration (Fluent incorporated). However the measurements were made at the same points which have been used experimentally. The Intake Momentum Drag is computed by equation (2.8), where v_0 is the mean velocity and W_1 is the engine mass flow measured by CFD.

4.7 Cradle Drag Calculation by Using CFD

The same experimental approach was used in CFD. Hence the force acting on the cradle was calculated using velocity measurement around the cradle and using the same drag coefficient experimentally used. Figure 4.22 shows the points around the cradle where the velocity measurement were taken.

The force acting on the cradle could be estimated directly by Fluent. This approach would be correct if the mesh was very fine which is difficult in terms of time and CPU memory capacity. Therefore former approach was used.

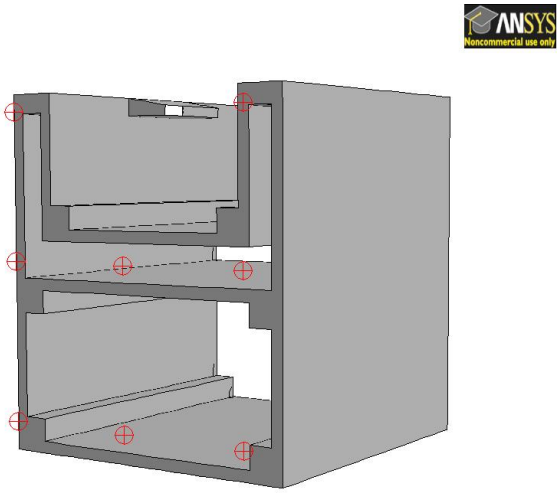

Figure 4.22 Velocity measurements around the cradle

4.8 Throat Force Calculation by Using CFD

The Throat force which is the gauge stream force can be evaluated in CFD by extracting the magnitude of the static pressure and the velocity at the engine throat.

4.9 Base Force Calculation by Using CFD

The secondary air flow starts to accelerate over the engine surface as consequence of the interaction between the engine exhausts and the detuner. This ejector pump effect creates a suction force which sucks the engine backward. Experimentally the static pressure is measured by four static probes over the converging shape of the engine nozzle.

Figure 4.23 Static pressure probes on the exhaust nozzle

Due to the high temperature at the nozzle exit plane probes were installed at 8 mm, 18 mm, 28 mm and 38 mm upstream of the nozzle exit plane as shown in Figure 4.23. Hence, the suction force was calculated using the product of the mean static pressure depression and the area change. The contribution given by the probe (1) to the base force is estimated in equation (4.7).

$$\phi_{Gbase-1} = (p_1 - p_0)A_{base} \tag{4.7}$$

Therefore, the axial base force is given in equation (4.8)

$$\phi_{Gbase} = \frac{\sum_{i-1}^{4}(p_i - p_0)}{4} A_{base} \tag{4.8}$$

where A_{base} is the base projected area.

Fluent integration tool allows a direct estimation of the static pressure distribution over the nozzle surface. The accuracy of this estimation is based on the quality of the mesh structure around the surfaces. The assumption was taken at the preparation stage of the models. Figure 4.24 shows the mesh around the engine converging nozzle.

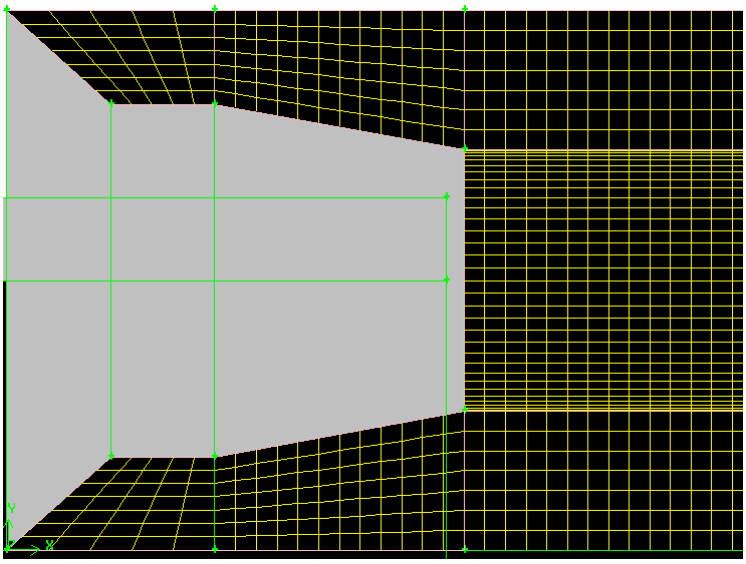

Figure 4.24 Grid structure around the exhaust nozzle

4.10 General Assumptions

Three thrust correction equations were derived by Gullia (Gullia, 2006). Each equation was derived relatively to a specific force accounting system around the engine. The task was to find the most applicable equation based on the shape of the engine and cradle in this research. Hence, Equation (2.21) is used in the analysis described in this paragraph. Some valid assumptions were considered in using the thrust correction equation. There are valid assumptions for the equation are discussed in this paragraph.

The drag of engine carcass appears in the thrust correction equations used in the comparison. Therefore it has the same effect on each thrust correction equation. However it is difficult to estimate this factor either experimentally or numerically. Hence this assumption is justified.

The derivation of the potential buoyancy effect factor has two approaches. The first was to use the accounting system starts from station (0); where the pre entry stream tubes start while the other one starts from station (f); after the bellmouth. Both approaches have the option of including the engine afterbody or not.

The base gauge force is computed experimentally by a direct measurement of the static pressure around the engine after-body. The thrust correction equations that Gullia (Gullia, 2006) derived were using a simple shape for the engine and cradle. However

the cradle shape which was simulated in this research was complicated and has a hollow h-shape. The assumption was that the potential buoyancy force starts from station (0) and includes the engine after body; ends at station (9).

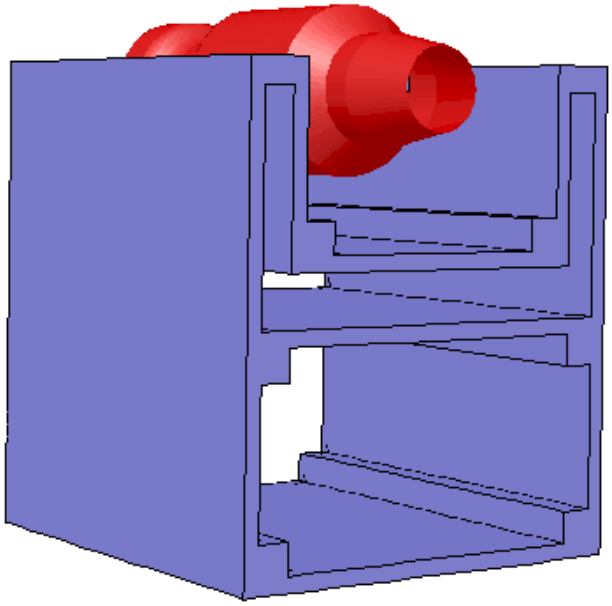

Figure 4.25 Cradle geometry on CFD

The other assumption is that the friction forces on the metric assembly; the engine or the floating part of the cradle are neglected.

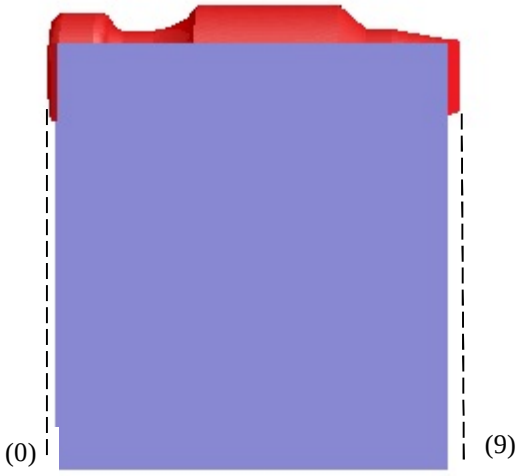

Figure 4.26 Engine entry and exit station

4.11 The derivation of Thrust Correction factor by CFD Analysis

The CFD simulations will be used in this paragraph to derive the thrust correction factors based on the methodology which have been described previously in this chapter. It should be reminded that the model boundary conditions were matched to that produced from the experiments. Such conditions are the engine and test cell mass flow rate. Accordingly the model should give the same entrainment ratio of that in the experiment.

Derived thrust correction factors will be substituted in equation (2.21). This thrust correction equation will be compared for the different test cell cross sections and power settings. The gross thrust is the unknown in the equation so F_{G9} can be put in the left side and all other factors in the right side. The equation was divide by the load measured to have it in percentage, so the equation can also be re-written as equation (4.9). Therefore in the figures TCF stands for $\frac{F_{G9}}{L}$.

$$\frac{F_{G9}}{L} = 1 + \frac{F_{G0}}{L} + \frac{D_{metric}}{L} - \frac{(F_{G9'} - F_{G0})_{ext\ pot}}{L} + \frac{\phi_{Gbase}}{L} \qquad \textbf{(4.9)}$$

The comparison over the other equations could not be made due to the difference in shape of the cradle to that used in the derivation of the thrust correction equations. However the comparison was able for the thrust correction factor individually. It should be noted that the potential buoyancy force term in the equation is computed by equation (2.23).

The CFD results for each test cell cross section are represented separately. The $\frac{F_{G9}}{L}$ for 700x700 test cell is shown in Figure 4.27. There is almost a linear variation between the $\frac{F_{G9}}{L}$ (in the vertical axis) with the engine to detuner distance (in the horizontal axis). The $\frac{F_{G9}}{L}$ factor increases with the power setting and decreases with the engine to detuner distance. Although 85% and 75% power settings are only represented at two distances but they correctly lay between 95% and 65%.

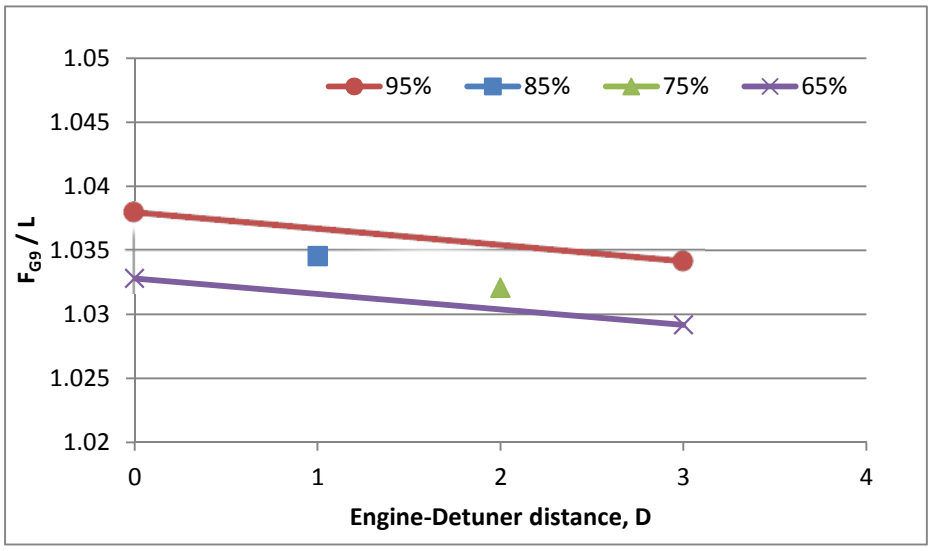

Figure 4.27 F_{G9} / L ratio for 700x700 cross section test cell

The two other configurations give similar trend lines with different gradients as shown in Figure 4.28 and Figure 4.29. The thrust correction factor is maximum at the smallest cross section area; 400x470. It decreases as the test cell cross section area increases.

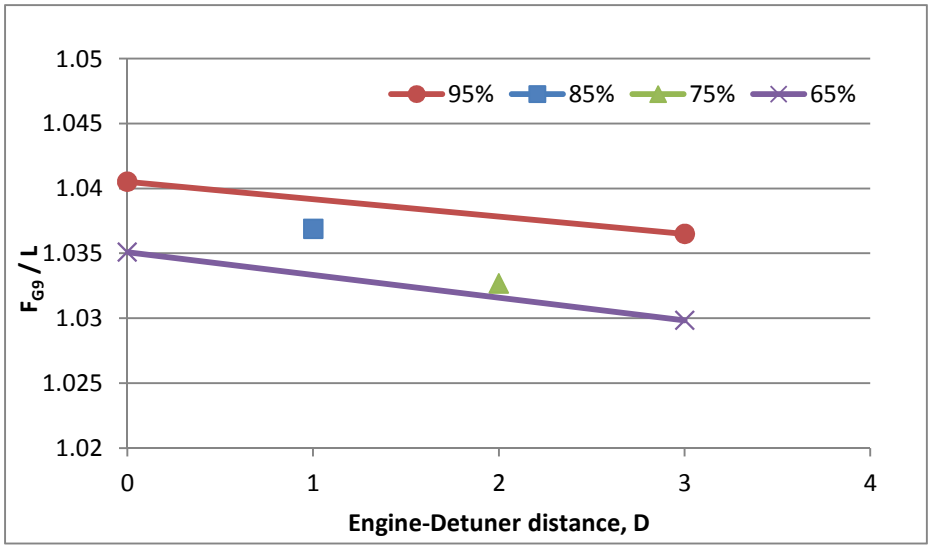

Figure 4.28 F_{G9} / L ratio for 550x550 cross section test cell

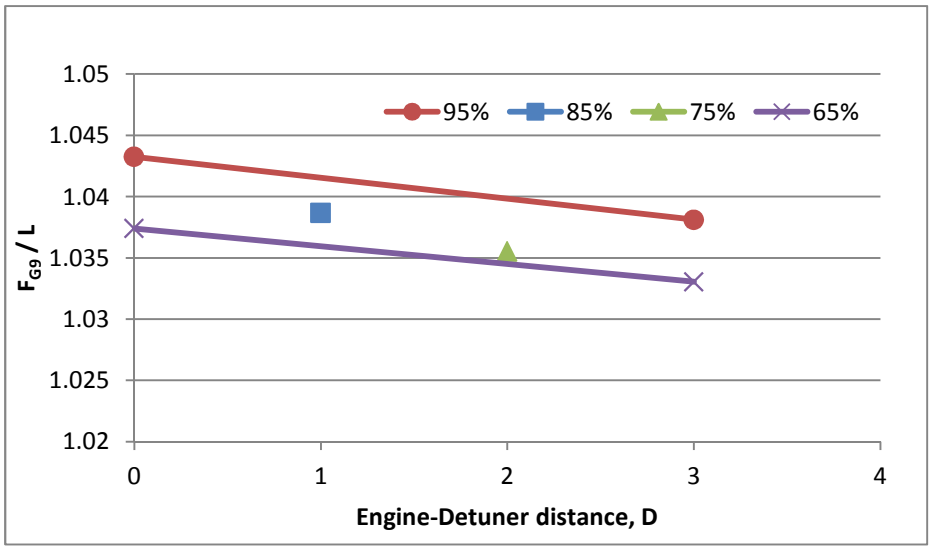

Figure 4.29 The F_{G9} / L ratio for 400x470 cross section test cell

The amount of the secondary air entering the test cell as well as the air flow velocity patterns inside the test cell are influenced by the distance between the engine and detuner. The effect of the engine to detuner separation distance on the TCF for 95% and 65% engine power settings for all three test cell cross sections are shown in Figure 4.30 and Figure 4.31.

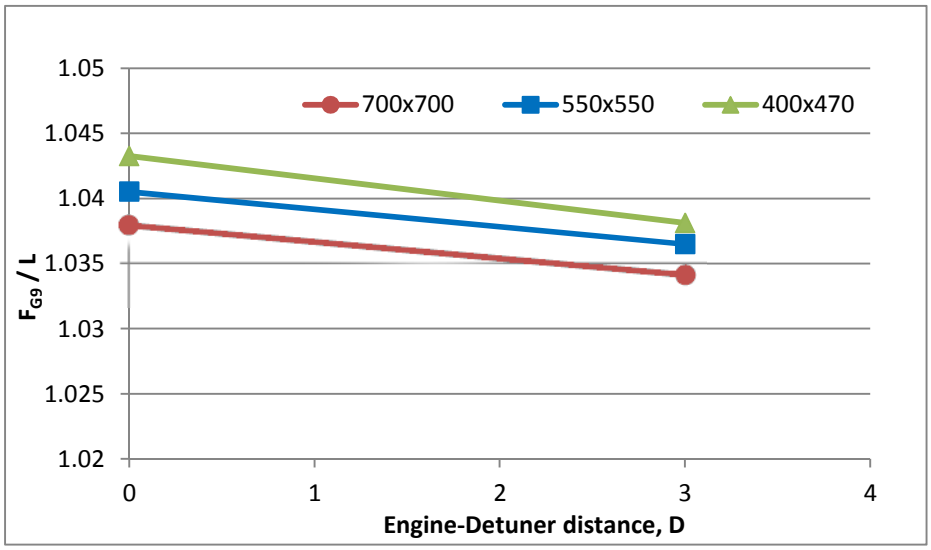

Figure 4.30 F_{G9} / L ratio for the three test cells and at 95% power setting

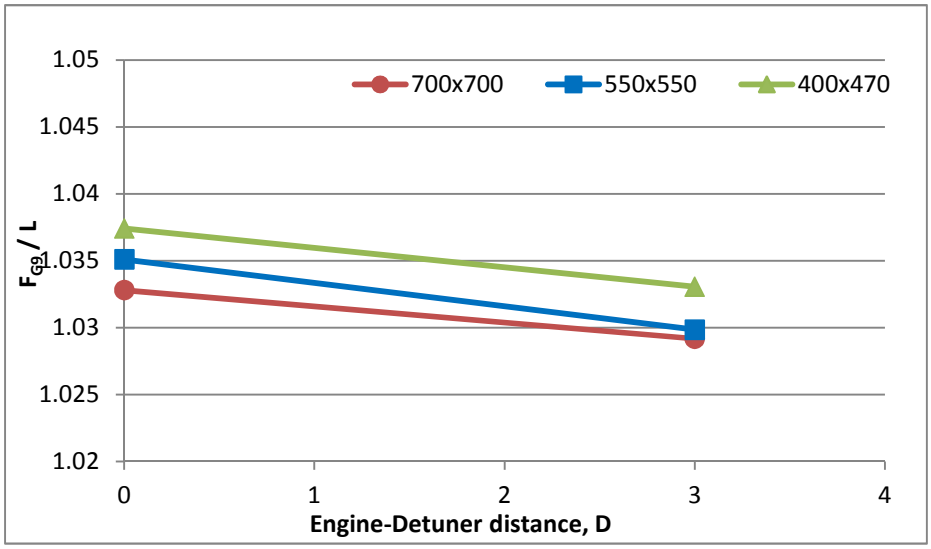

Figure 4.31 F_{G9} / L ratio for the three test cells and at 65% power setting

Figure 4.32 and Figure 4.33 show the calculated intake momentum drag for 95% and 65% engine power settings for different nozzle - detuner separation distances in each test cell. For a given engine power setting the intake momentum drag increases with nozzle - detuner separation distance. This could be related to the increase in the cell total air mass flow and the secondary air velocity. The intake momentum drag magnitude increases as the test cell cross section decreases.

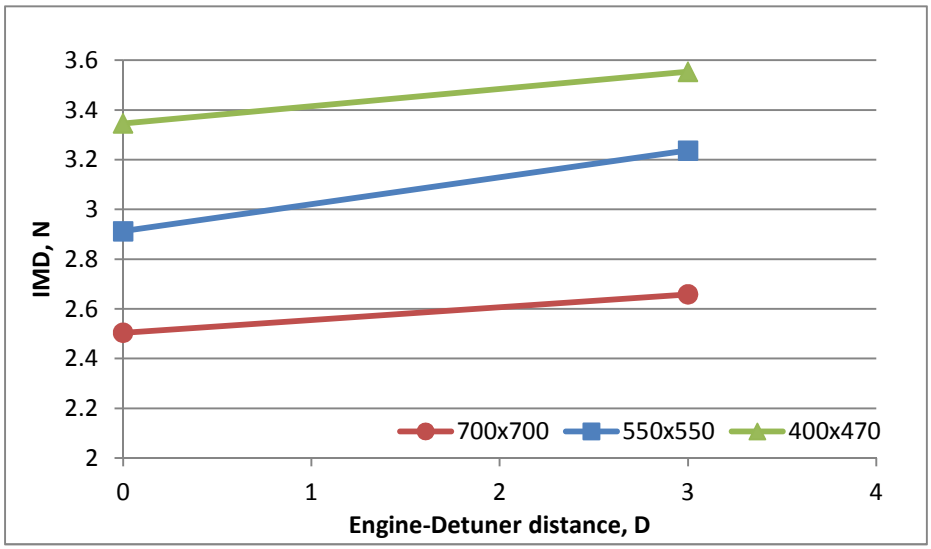

Figure 4.32 Intake momentum drag for all test cells at 95% power setting

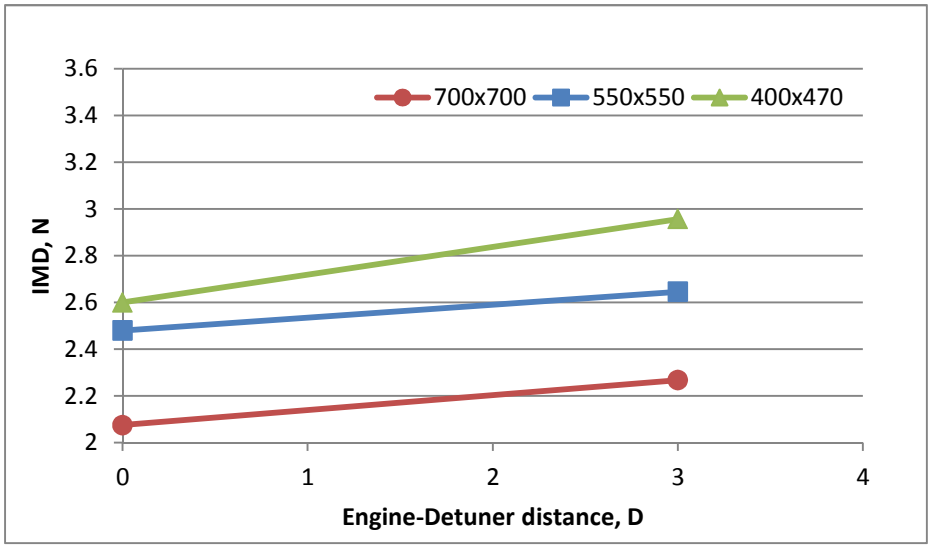

Figure 4.33 Intake momentum drag for all test cells at 65% power setting

The intake momentum drag could be shown for each test cell individually to represent the other two engine power setting in the same figure. The IMD at 85% and 75% engine power settings magnitude come between the other two extreme power settings as can be seen in Figure 4.34. Therefore this validates that the IMD increases with the engine power setting. Figure 4.35 and Figure 4.36 show the intake momentum drag for other test cells.

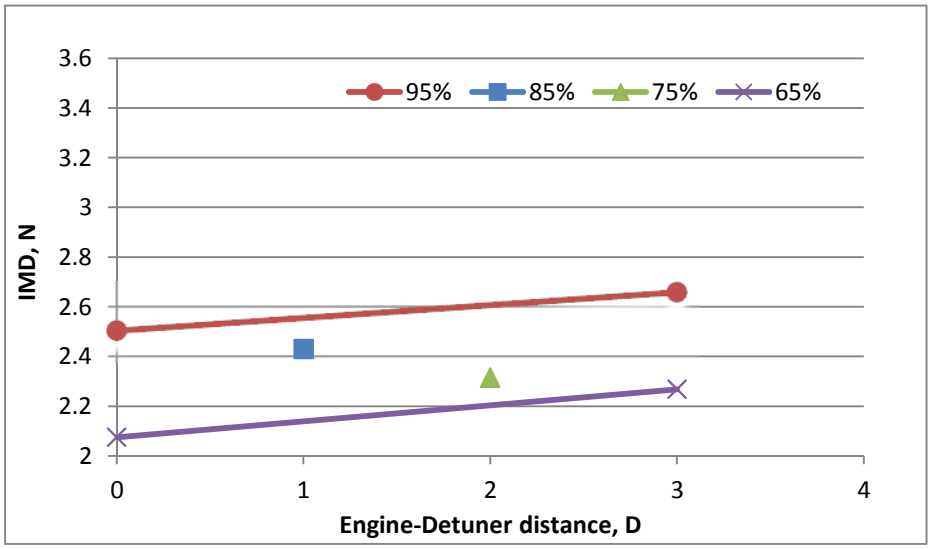

Figure 4.34 Intake momentum drag for 700x700 test cell

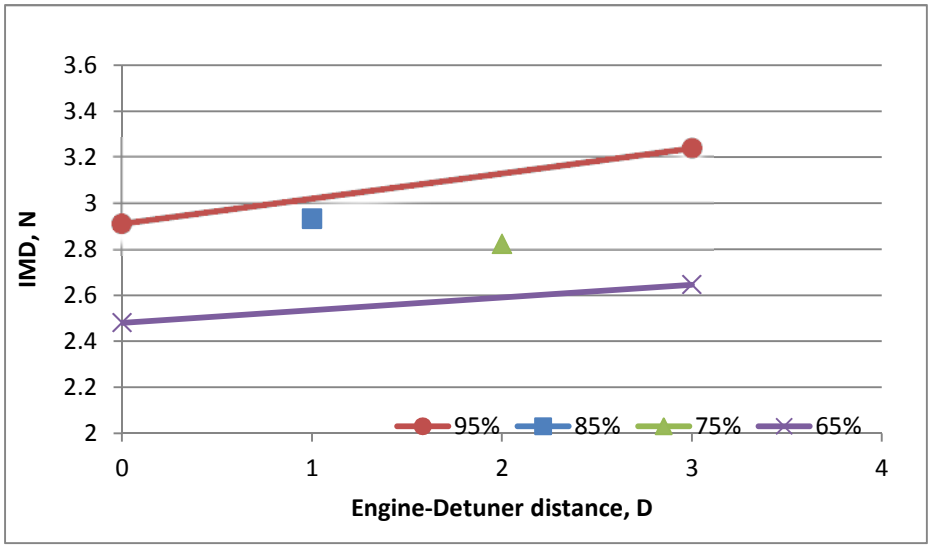

Figure 4.35 Intake momentum drag for 550x550 test cell

In summary intake momentum drag is the largest thrust correction factor. It increases with the engine-detuner gap. This is related to the entrainment ratio since increasing the gap causes the total mass flow going through the cell to increases and the intake momentum drag follows the entrainment ratio trend. In addition, for the same cell dimension, the free stream velocity increases. Intake momentum drag increases as the test cell size decreases. Decreasing test cell size increases the flow velocity.

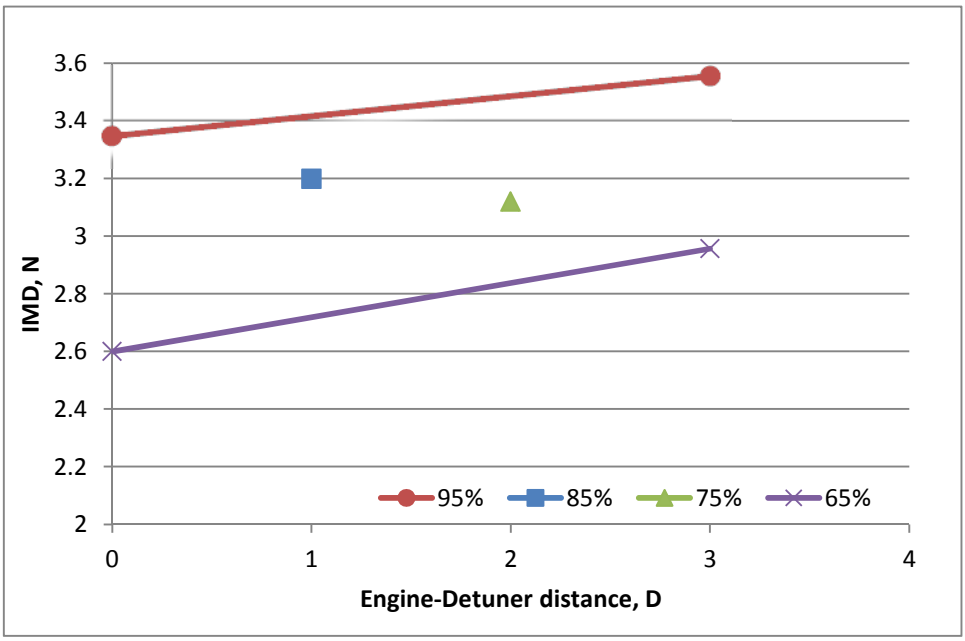

Figure 4.36 Intake momentum drag for 400x470 test cell

The Rolls-Royce First Principle approach has been used to compute the cradle drag. Fluent was used to measure the airflow velocity near the frontal blockage areas of the moving part of cradle, see Figure 4.22. The pressure load is computed by using equation (2.9) and the cradle drag is computed using equation (2.10).

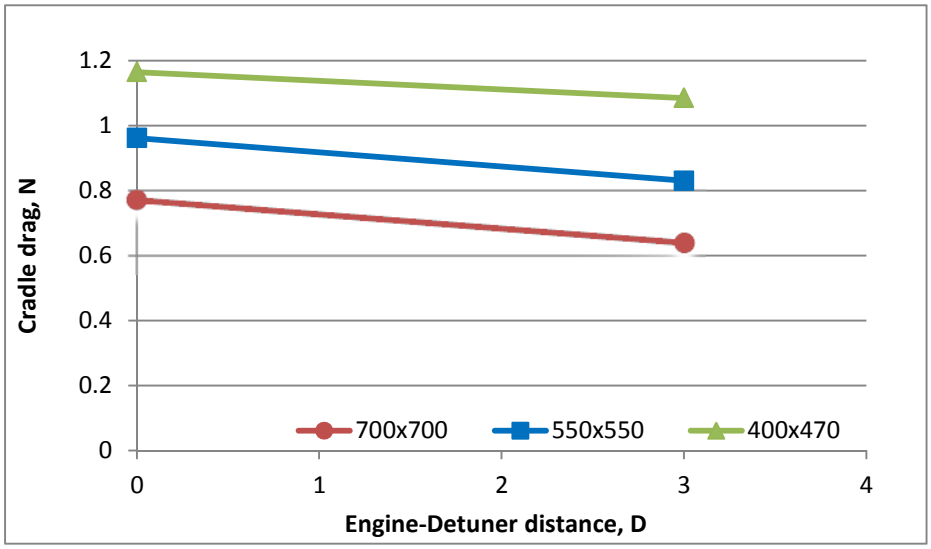

Figure 4.37 Cradle drag estimation for all test cells and at 95% power setting

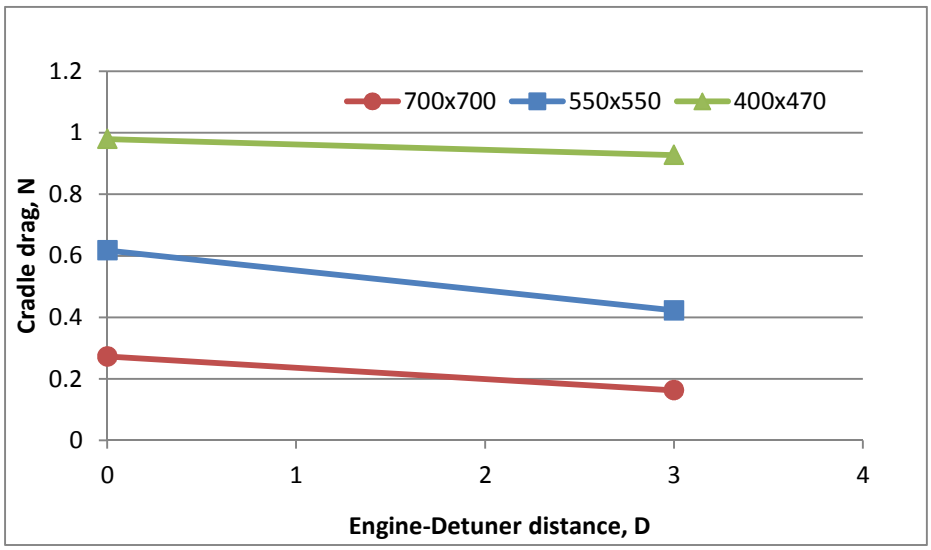

Figure 4.38 Cradle drag estimation for all test cells and at 65% power setting

The average of the eight points velocity in front of the cradle is taken; see Figure 4.22. The cradle drag coefficient (Cd) used is the same used in the experimental estimation. Figure 4.37 and Figure 4.38 show the computed cradle drag with nozzle-detuner separation distance for two power settings; 95% and 65%. The cradle drag in general decreases with the distance between nozzle and detuner. The decrease trend of the

cradle drag can be related to the increase of ejector pump effect as the nozzle-detuner separation decreases. The ejector pump effect will affect the velocity profile around the cradle and consequently the cradle drag. It should also be noted that the cradle drag increases with engine rotational speed.

It should be noted as well that the cradle drag for the other two power settings are not been shown in the previous figures. Hence represinting the cradle for each test cell cross section will help to show it for all the power settings. Figure 4.39 to Figure 4.41 show the cradle drag for each test cell at all the power settings.

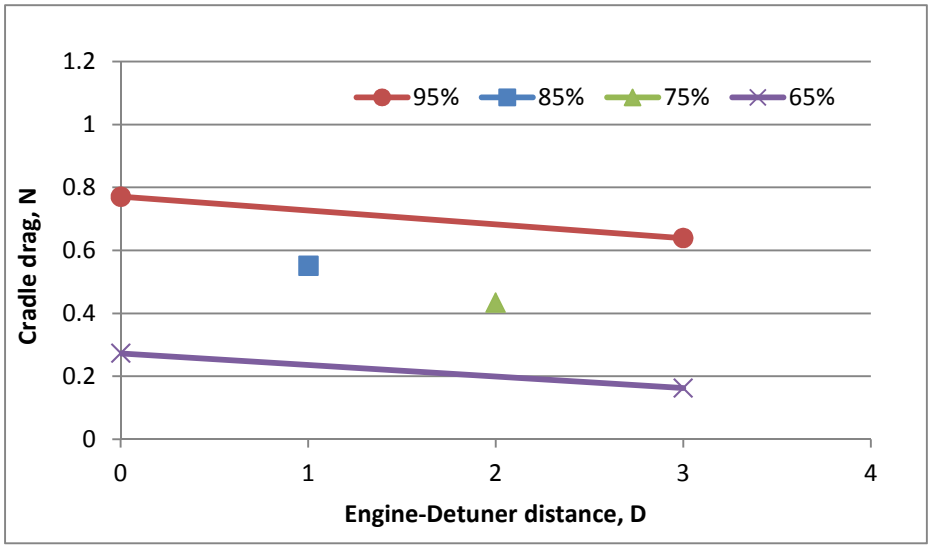

Figure 4.39 Cradle drag estimation for 700x700 test cell

The CFD models have been used for computing the base drag using equation (4.8). The results of the calculation will be shown where it can be seen that when the engine nozzle is in the same plane as the detuner inlet, the base drag is one order of magnitude higher.

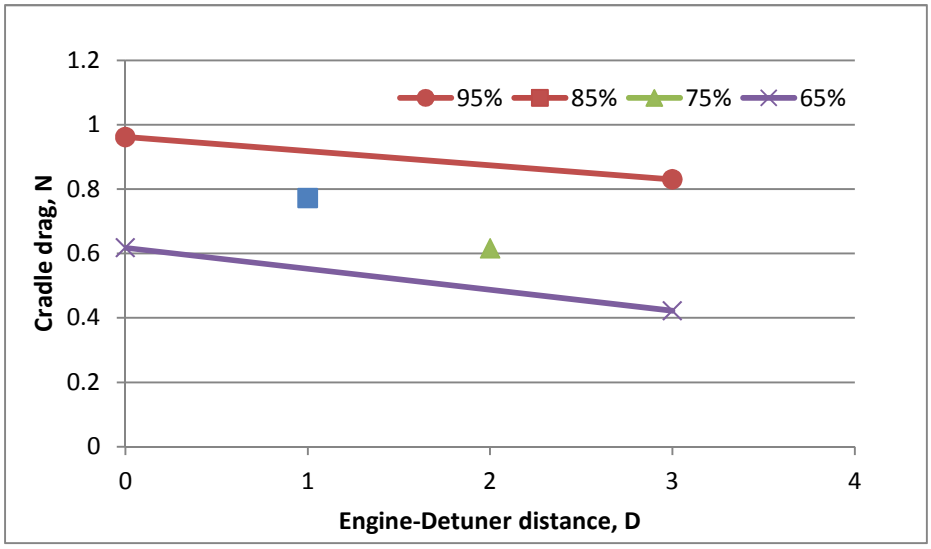

Figure 4.40 Cradle drag estimation for 550x550 test cell

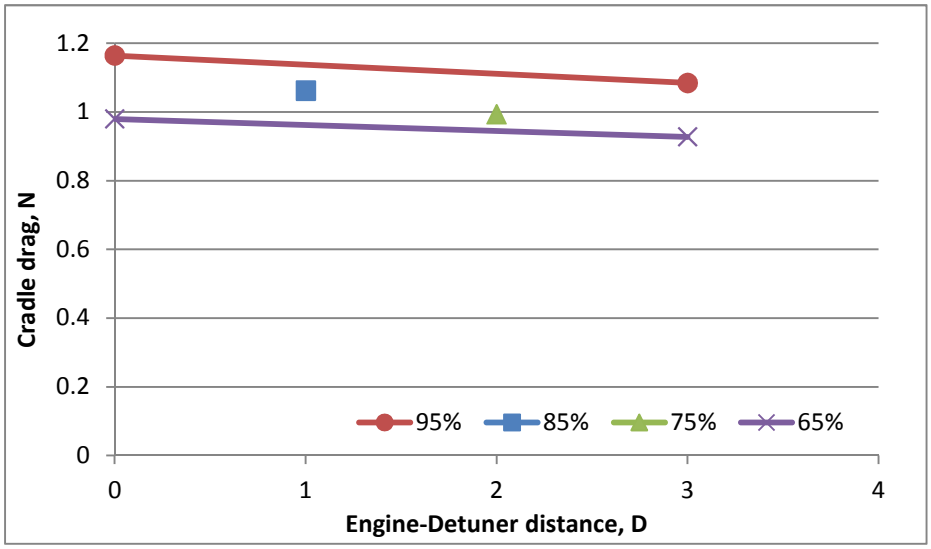

Figure 4.41 Cradle drag estimation for 400x470 test cell

In summary reducing the gap the ejector effect Increases the flow velocity around the Cradle and the after-body of the engine. Small distances between the engine nozzle and detuner the ejector pump effect increases the velocity around the cradle due to the increased blockages hence total pressure losses increase. Secondary flow entering the detuner experiences an acceleration which can be felt also by the flow around the cradle if the exhaust collector is close to the engine stand. There is a detuner position which gives rise to a minimum cradle drag. This is probably due to a balance between the entrainment flow and the ejector pump effect which accelerates the flow around the cradle

Figure 4.42 and Figure 4.43 give the base drag for the largest and smallest power settings in all test cell cross sections. It can be seen also that the base drag increases with the engine power setting in all test cells. Figure 4.44 to Figure 4.46 show the base drag in each test cell for all engine power settings. It can be also noted that the base drag increases as the test cell cross section decreases. This can be related to the increase in the air flow speed with the decrease in the cross section of the test cell.

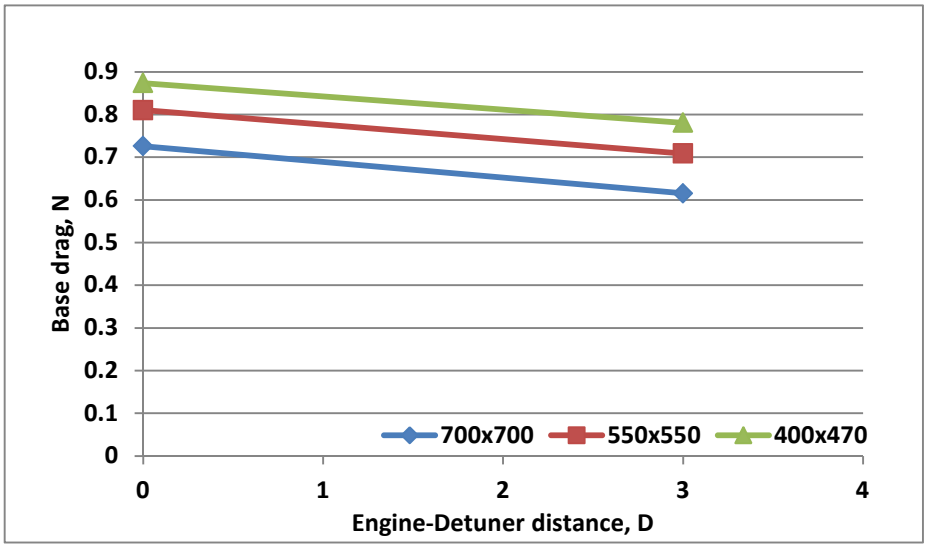

Figure 4.42 Base drag estimation for all test cells and at 95% power setting

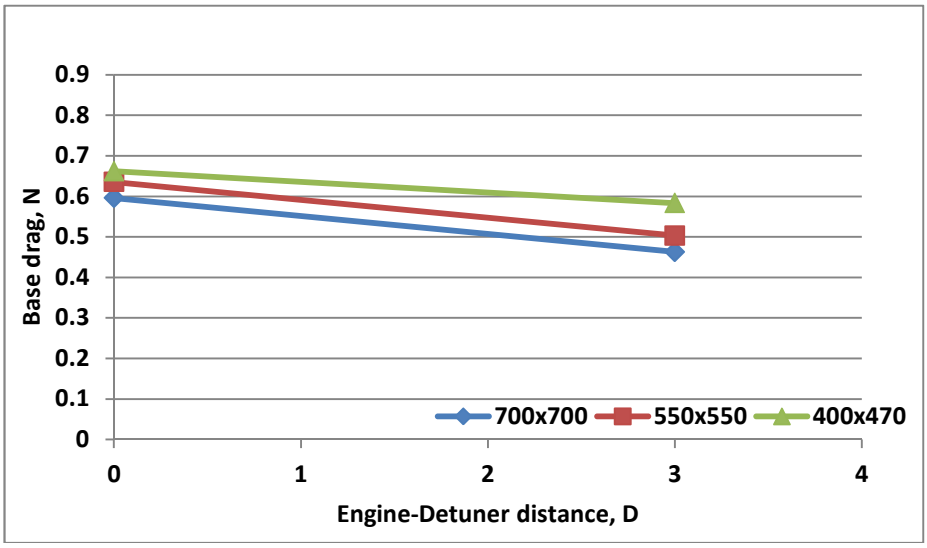

Figure 4.43 Base drag estimation for all test cells and at 65% power setting

The base drag in each test cell cross section could be represented for all engine power settings together as will be shown next. Figure 4.44 to Figure 4.46 show the base drag

in each test cell. The trends in all test cells are similar where the base drag increases with the engine power setting.

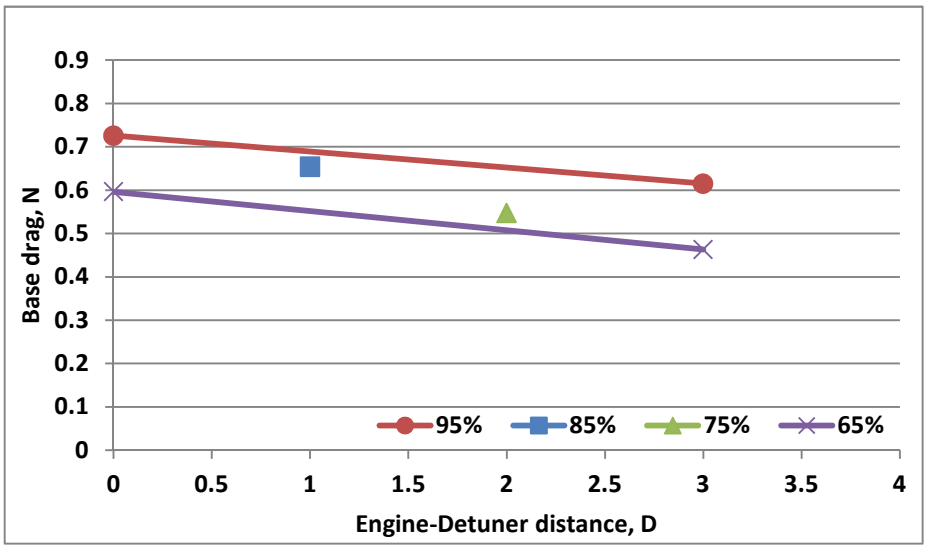

Figure 4.44 Base drag estimation for 700x700 test cell

When the engine nozzle is in the same plane of the detuner inlet, the base drag is an order of magnitude higher than in any other position. This can be related to the ejector pump effect. The secondary flow around the afterbody of the engine starts to accelerate and as consequence a region of low static pressure is created on the rear part of the engine. The engine, therefore, tends to be to be sucked rearwards by the depression and consequently the thrust measured accounts for this undesired effect.

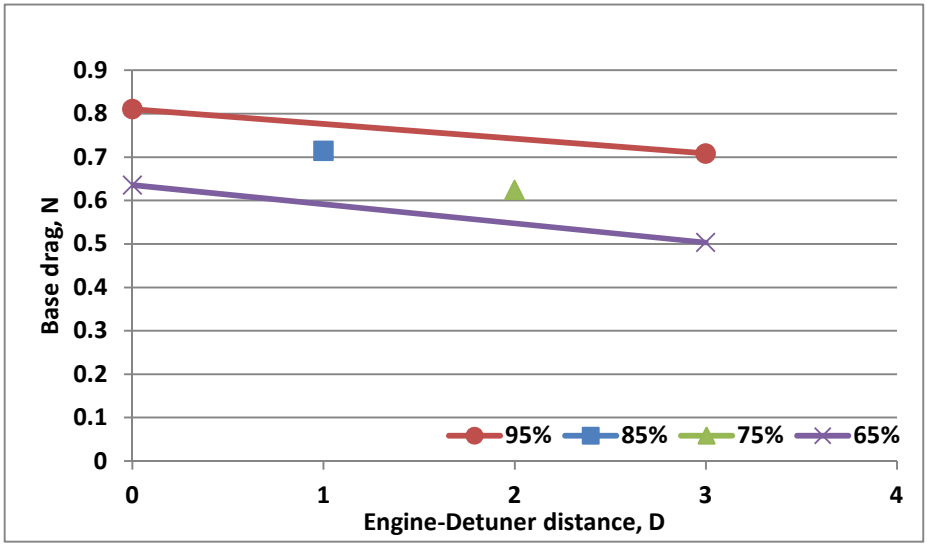

Figure 4.45 Base drag estimation for 550x5500 test cell

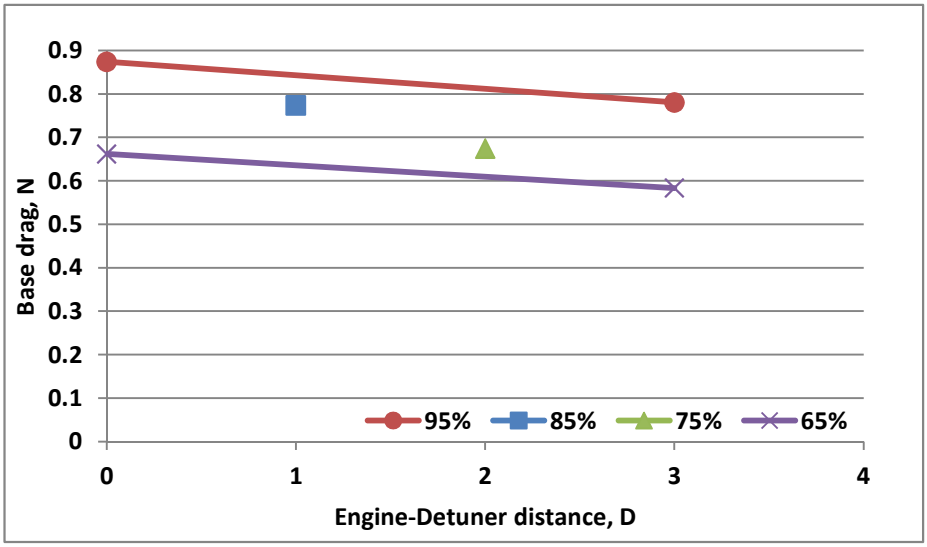

Figure 4.46 Base drag estimation for 400x470 test cell

In summary when the engine nozzle is in the same plane as the detuner inlet, the base drag is one order of magnitude higher. It has been noted that a higher degree of depression (the static pressure field around the engine nozzle) occured when the engine is set closer to the detuner. The depression around the engine nozzle increases as the test cell dimensions decrease.

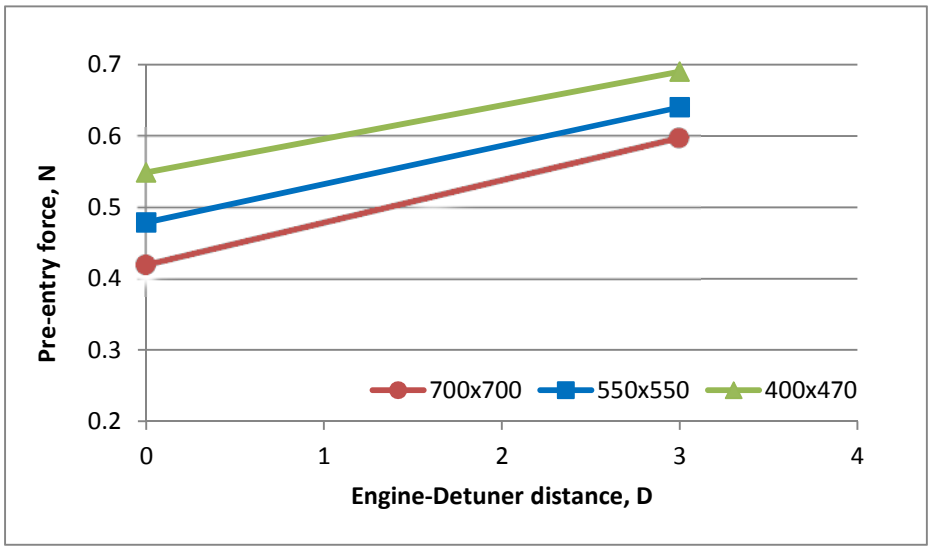

Figure 4.47 Pre-entry force estimation for all test cells and at 95% power setting

The pre-entry force definition is a relation between the pressure difference and the projected area of the stream tube which was generated from the stagnation point on the

engine bellmouth. From the pre-entry force point of view these two effects act in opposite way.

Figure 4.47 and Figure 4.48 show the pre-entry force in all test cells for the maximum and minimum engine power settings respectively. It is possible to note the effect of changes of the cell cross sectional area on the force factor. The pre entry force decreases with the increase in test cell cross sectional area. Increasing that area the flow velocity inside the cell reduces. If from one side this allows a reduction in the pressure difference from the other side this increases the projected area of the stream tube. From the pre-entry force point of view these two effects act in opposite way.

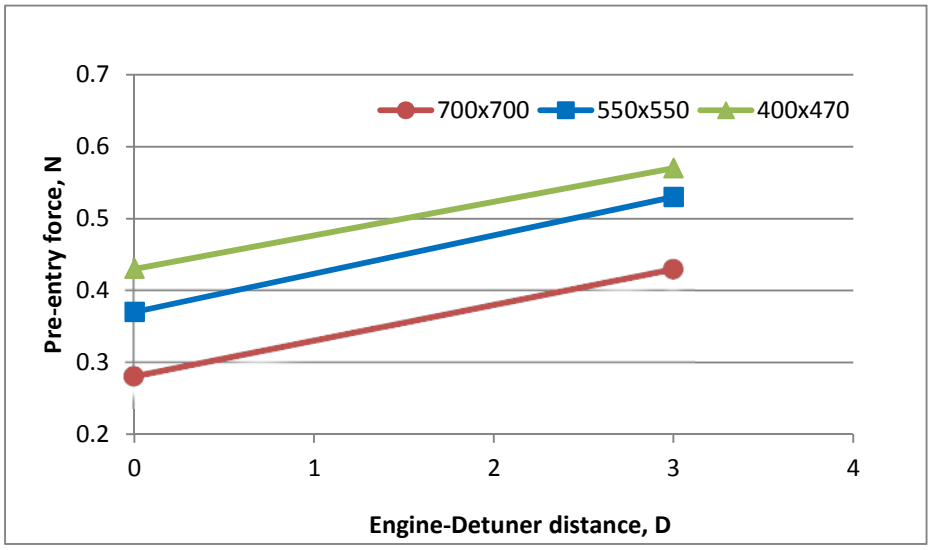

Figure 4.48 Pre-entry force estimation for all test cells and at 65% power setting

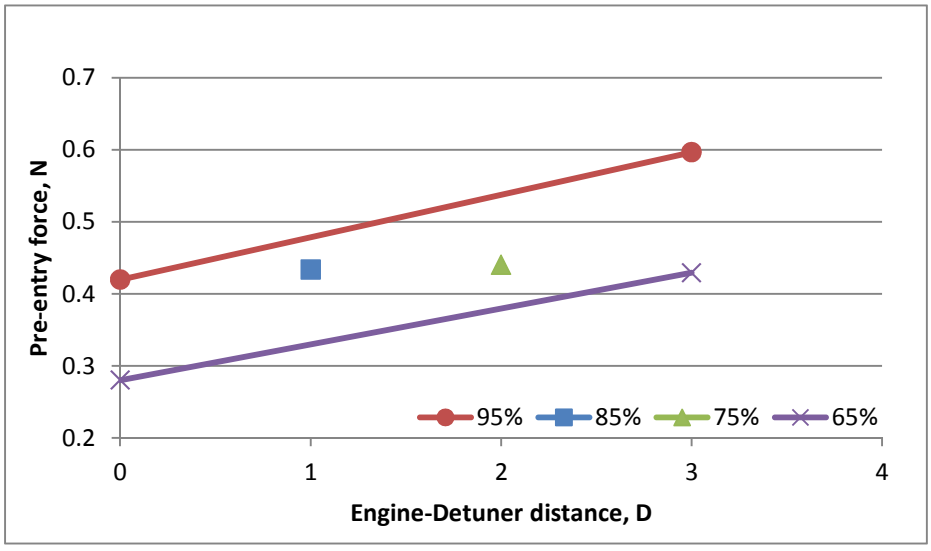

Figure 4.49 Pre-entry force estimation for 700x700 test cell

Indeed a reduction in the pressure difference brings a reduction in Φ_{pre} and an increase in projected area brings an increase in Φ_{pre}. It is clear that the pressure reduction has a bigger contribute than the area increasing and therefore the pre-entry force decrease as the cross sectional area increases.

The pre-entry force is shown for each test cell individually in Figure 4.49 to Figure 4.51. The trend of the curves shows an increase in the pre-entry force with distance between the engine and the detuner entry. The explanation of this could be the increase in the flow velocity within the test cell as the engine moves out from the detuner entry.

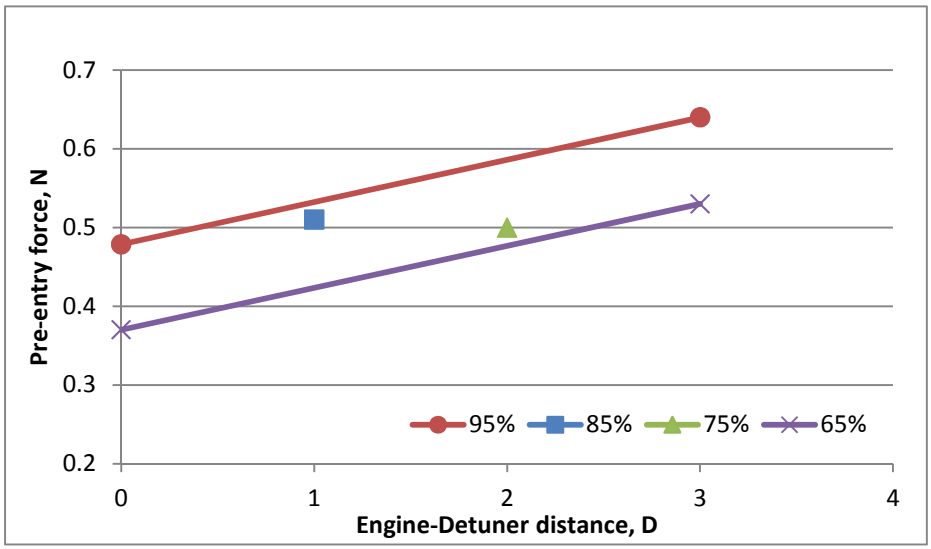

Figure 4.50 Pre-entry force estimation for 550x550 test cell

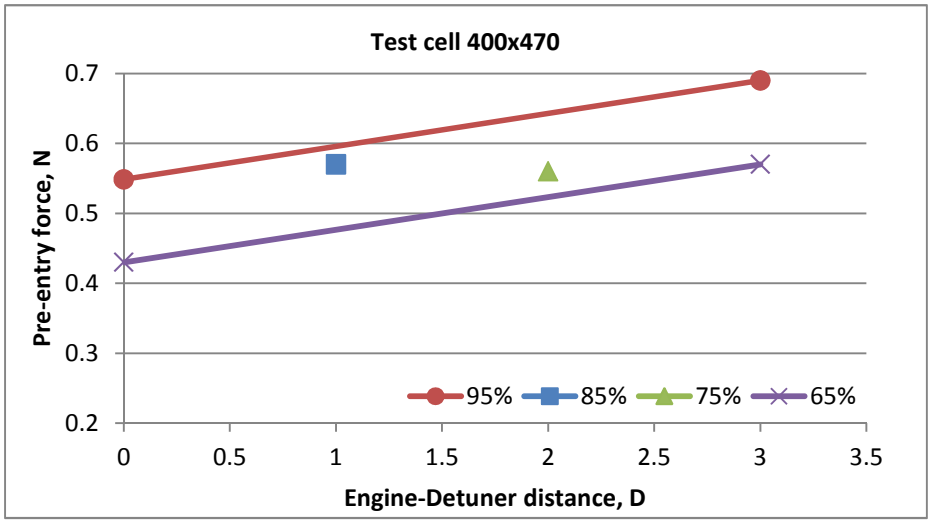

Figure 4.51 Pre-entry force estimation for 400x470 test cell

4.12 The CFD and Experimental Results Comparison

The comparison between the measured and simulated thrust correction factor starts by showing the thrust correction factor for each test cell as per each power setting. The data lost problem which happened prevented the author form having all cases simulated in CFD. Therefore the approach was to chose the most cases which possibly give a general view for the whole work.

It is essential before start discussing the comparison to define the representation difference of TCF in both CFD and experimental results. Experimentally the thrust correction factor was the ratio of the outdoor to indoor engine thrust measurements. However the TCF in CFD was used as the ratio of the engine gross thrust by the load measured; F_{G9}/L.

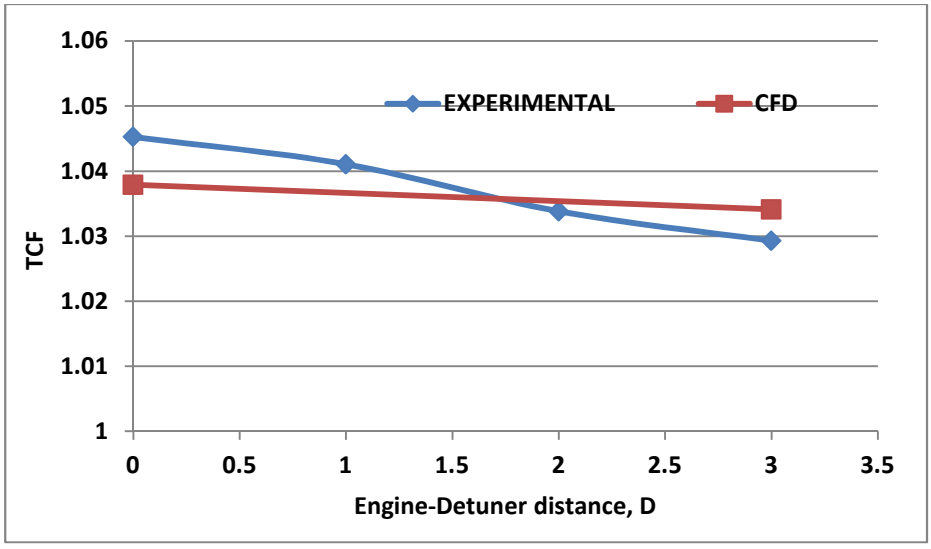

Figure 4.52 Thrust correction factor, CFD with experimental comparison; cell 700x700 and 95%

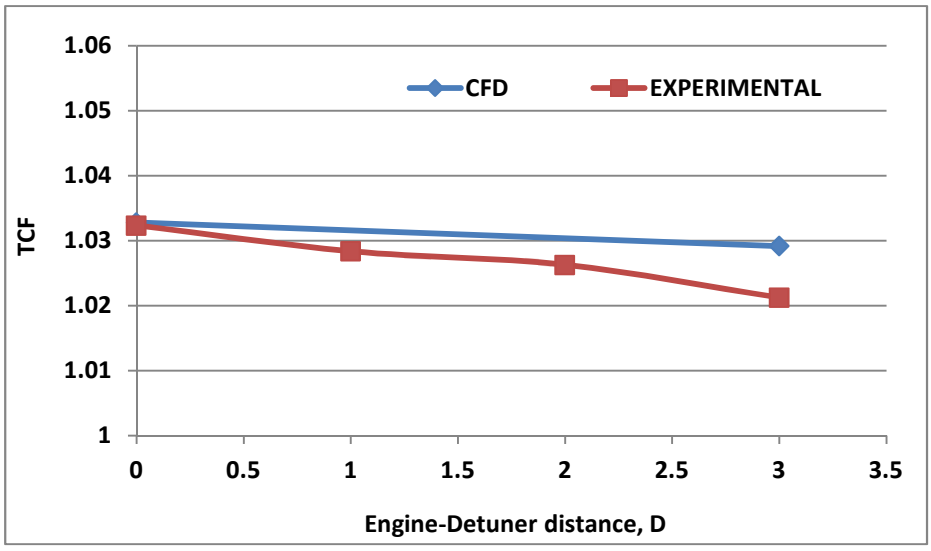

Figure 4.53 Thrust correction factor, CFD with experimental comparison; cell 700x700 and 65%

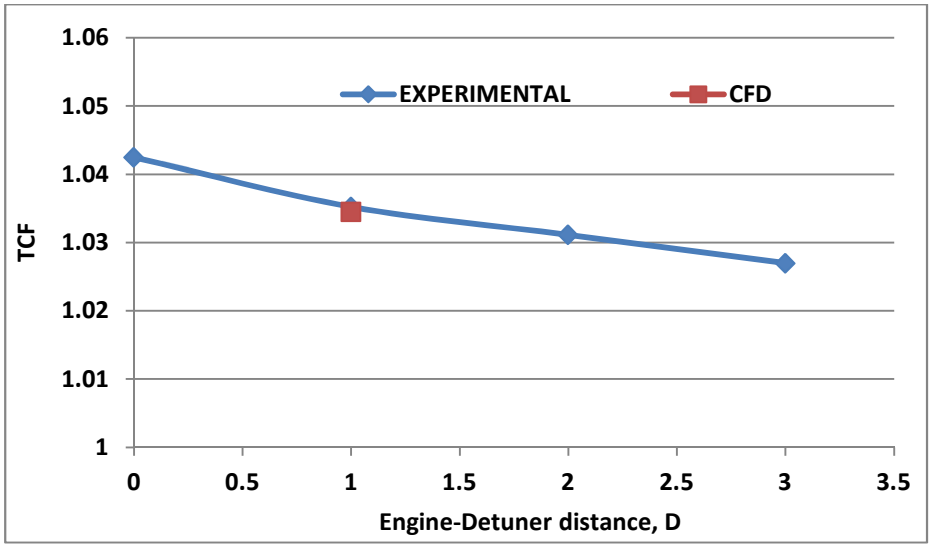

Figure 4.54 Thrust correction factor, CFD with experimental comparison; cell 700x700 and 85%

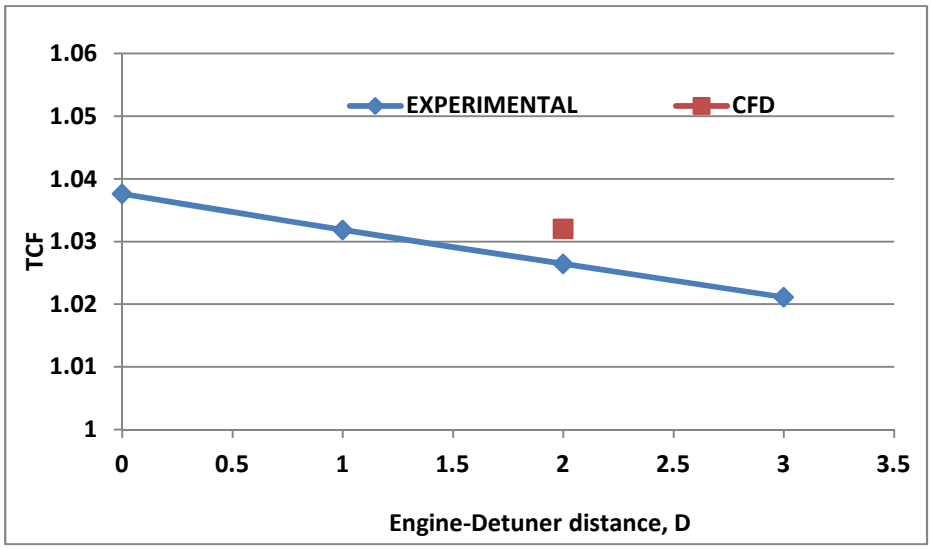

Figure 4.55 Thrust correction factor, CFD with experimental comparison; cell 700x700 and 75%

To start with the test cell of 700x700 cross sectional area, Figure 4.52 to Figure 4.55 show the comparison of thrust correction factor (TCF) for both CFD and the experiments. Although some cases are overlapping each other the difference in others was less than 2%. Figure 4.52and Figure 4.53 show the comparison for 95% and 65% engine power setting have two CFD modelled cases. This gives a better representation of the comparison as it covers more cases. It should be noticed that both approaches give same trend in relation with the engine to detuner distance.

The TCF decreases as the distance between the engine nozzle and detuner increases. The ejector pump effect between the engine nozzle and the detuner decreases as the engine nozzle moves away from the detuner. This can be related to the trend of the TCF.

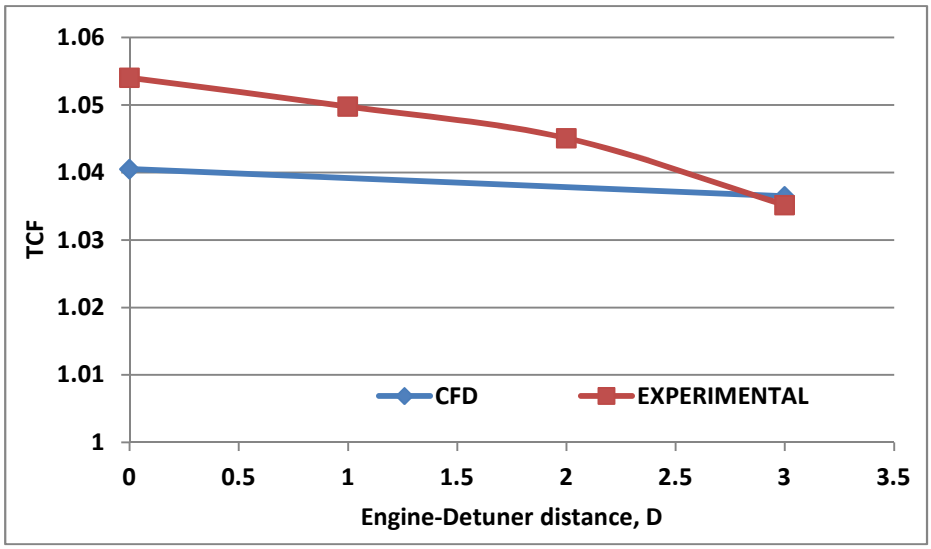

Figure 4.56 Thrust correction factor, CFD with experimental comparison; cell 550x550 and 95%

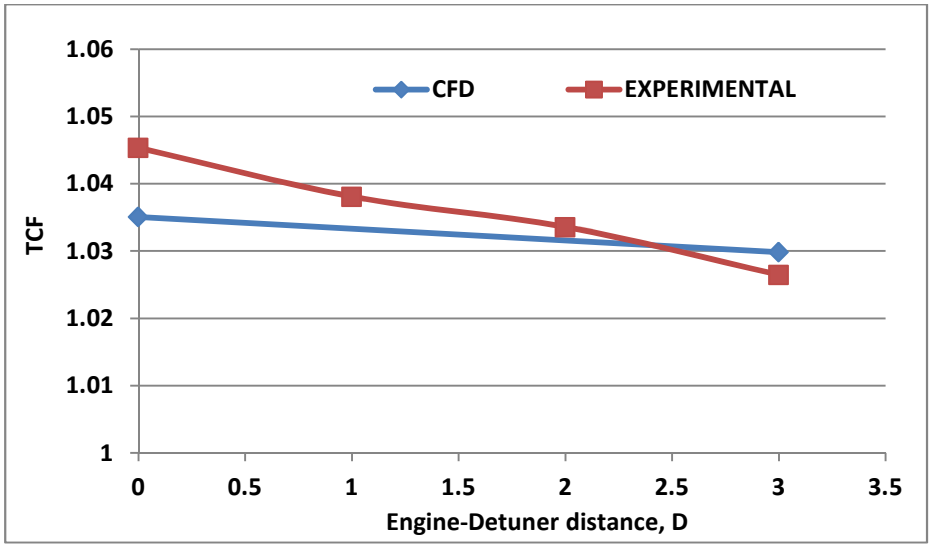

Figure 4.57 Thrust correction factor, CFD with experimental comparison; cell 550x550 and 65%

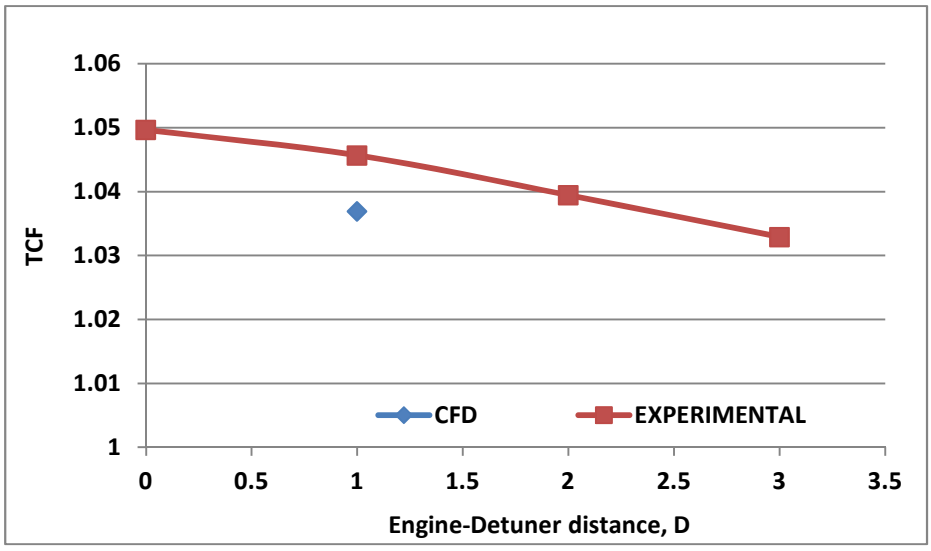

Figure 4.58 Thrust correction factor, CFD with experimental comparison; cell 550x550 and 85%

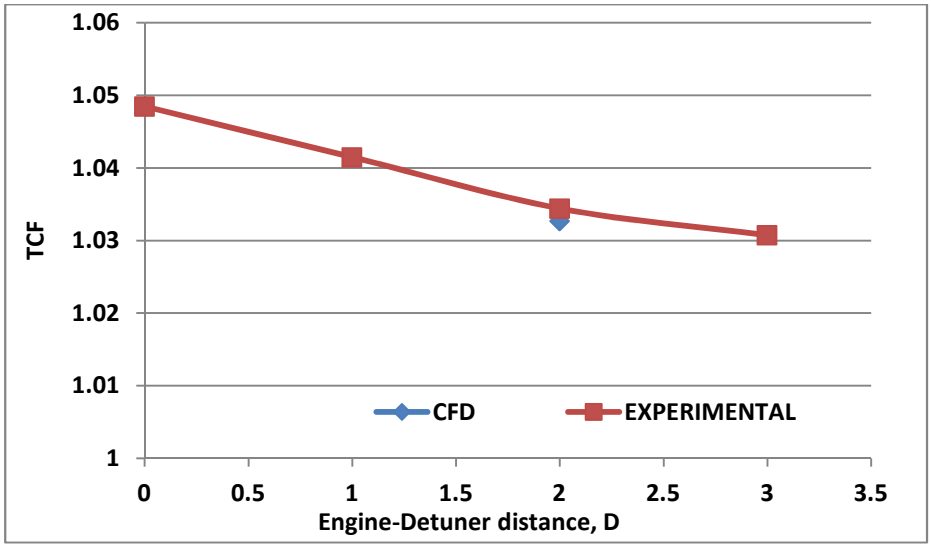

Figure 4.59 Thrust correction factor, CFD with experimental comparison; cell 550x550 and 75%

Figure 4.56 to Figure 4.59 show the results comparison for 550x550 cross sectional area test cell. The first two figures are for 95% and 65% power settings where two CFD cases were simulated. Similar to the larger test cell the TCF in 550x550 test cell shows a good degree of the matching.

The results confirm that the estimation of the thrust correction factor by Fluent was able to account to the thrust difference in the practical work. Comparing the result obtained by compiling the thrust correction equation by CFD and the experimental results it is possible to obtain a validation of the findings.

The last set of results comparison is for the 400x470 cross sectional area test cell, see Figure 4.60 to Figure 4.63. The same issues considered in the other test cell are applied here. There is a big match between the CFD and experimental results with respect to the small percentage of error.

The bigger difference between the thrust correction equations derived by CFD and the experimental result is about 0.55% of the load measured. Therefore regardless of the method used to compute the thrust correction factors (back-to-back test, experimental measurements, or computational analysis) errors will be always present. The error reported here is within the acceptable margin defined above in the literature.

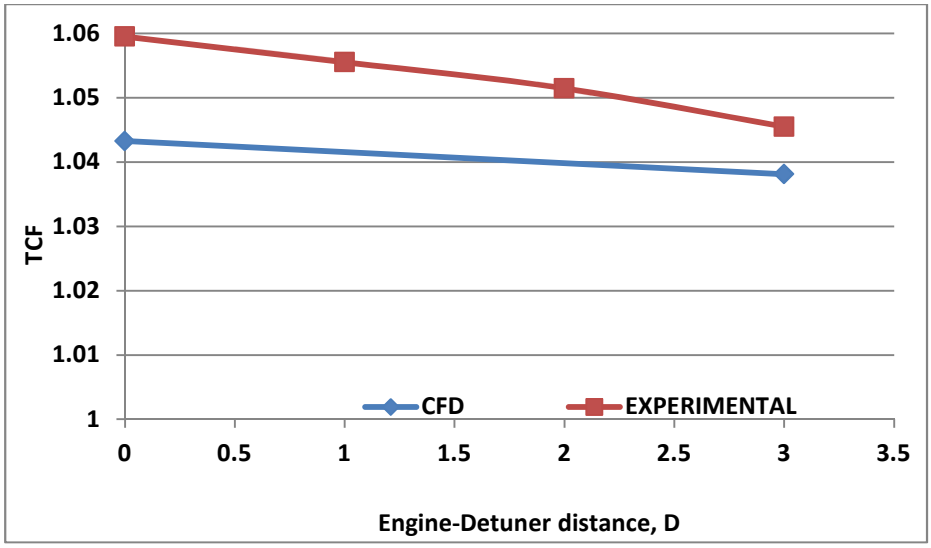

Figure 4.60 Thrust correction factor, CFD with experimental comparison; cell 400x470 and 95%

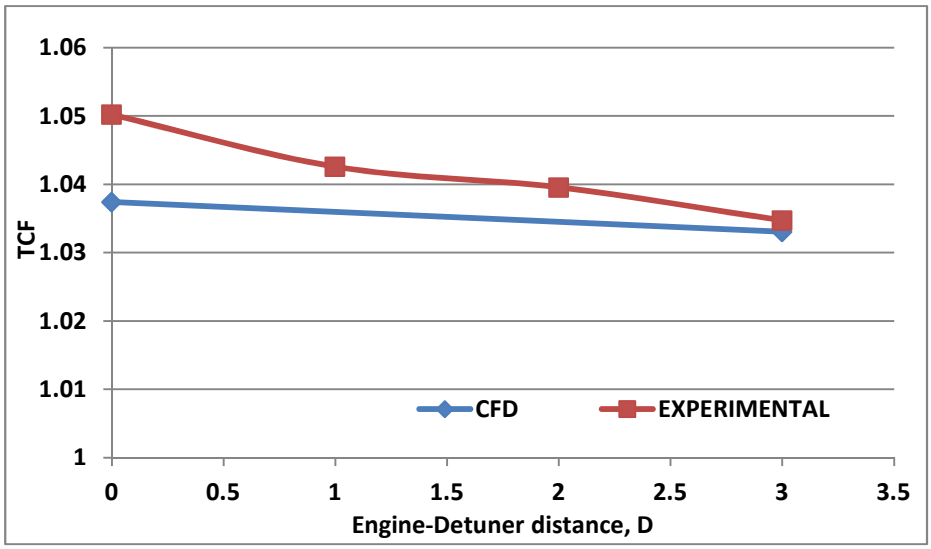

Figure 4.61 Thrust correction factor, CFD with experimental comparison; cell 400x470 and 65%

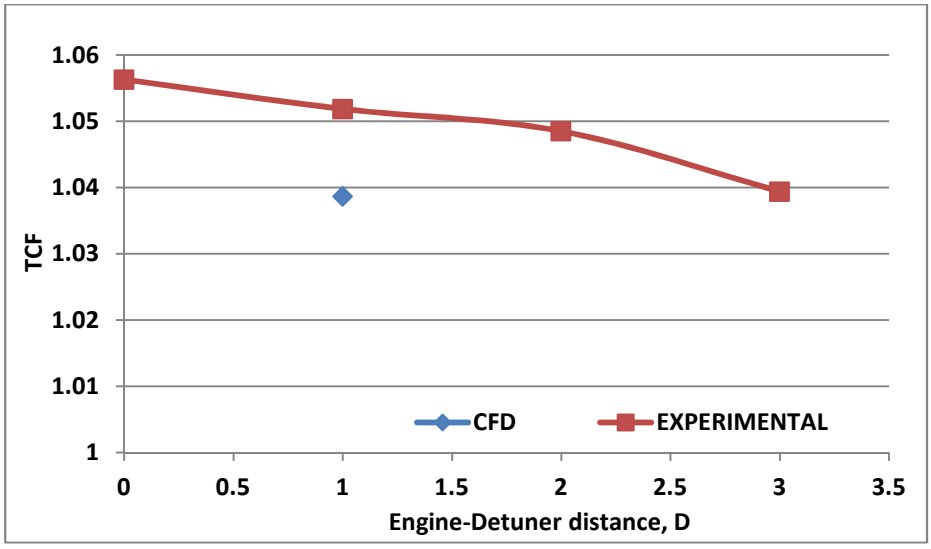

Figure 4.62 Thrust correction factor, CFD with experimental comparison; cell 400x470 and 85%

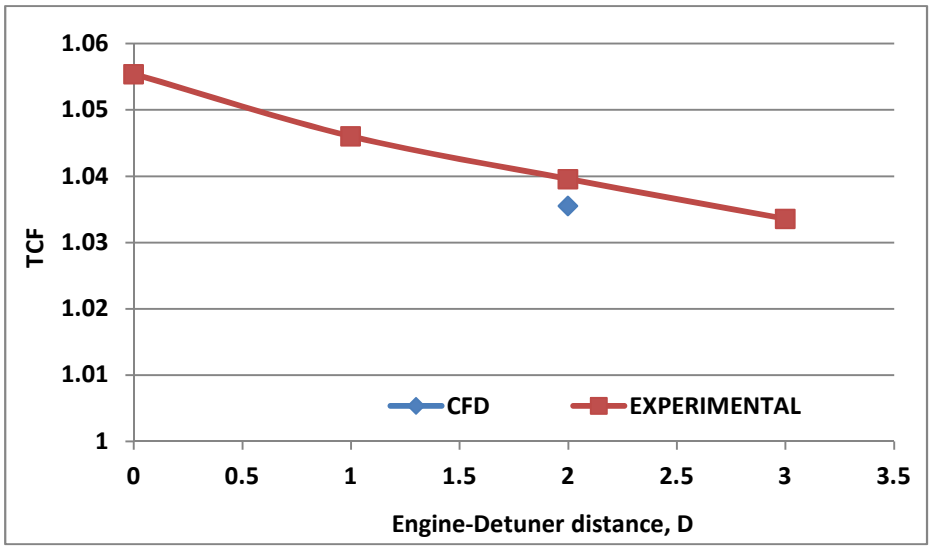

Figure 4.63 Thrust correction factor, CFD with experimental comparison; cell 400x470 and 75%

In summary both computational fluid dynamics and experimental results gave same trends of thrust correction factor. It has been found that the biggest difference is only 1% for the largest test cell. In addition the biggest difference is only 2% for the smallest test cell. These outcomes will be emphasised later in the conclusions section.

It was able to estimate experimentally the intake momentum dag, cradle drag and base drag. Therefore it was able to have a comparison of the experimental and CFD estimation between these factors. Figure 4.64 to Figure 4.66 show the intake momentam comparison for the three test cells. The boundary conditions in the CFD analysis was derived from the experiments. The CFD simulatios were able to validate those derived experimentally.

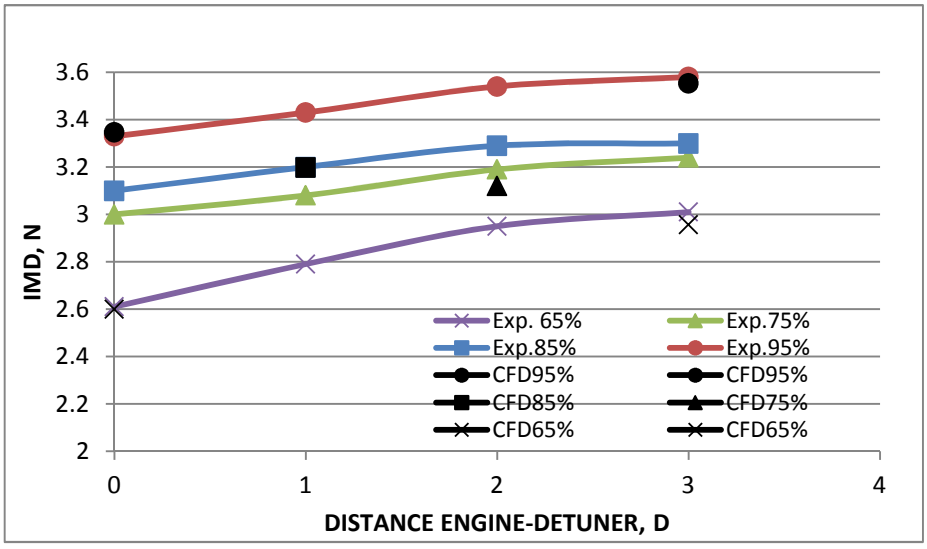

Figure 4.64 Intake momentum drag, CFD with experimental comparison; cell 700x700

The trend line of both approaches was the same. Regardless of the method used to compute the thrust correction factor errors will be always present. The error reported here is within a small margin. The intake momentum drag increases with engine nozzle to detuner distance. The effect of the engine power setting was clear as the intake momentum drag increases with the engine power setting.

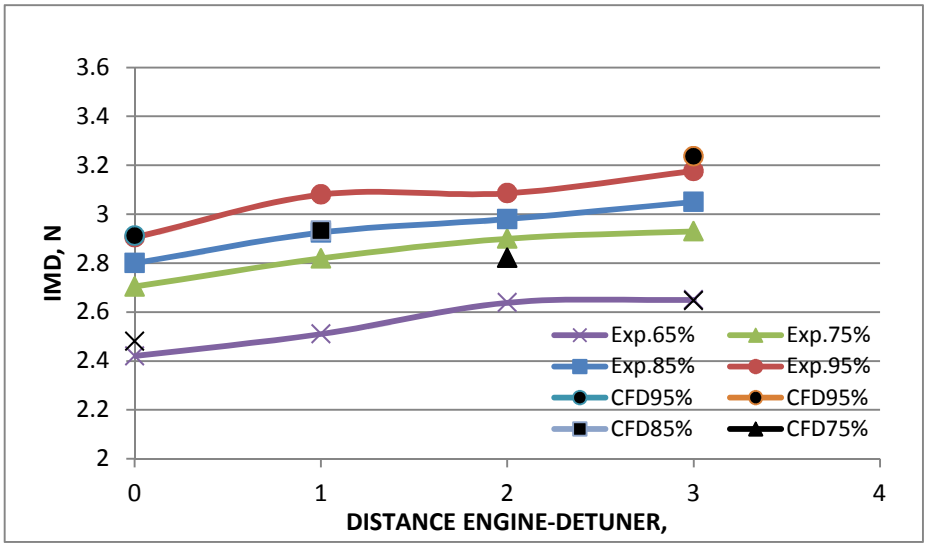

Figure 4.65 Intake momentum drag, CFD with experimental comparison; cell 550x550

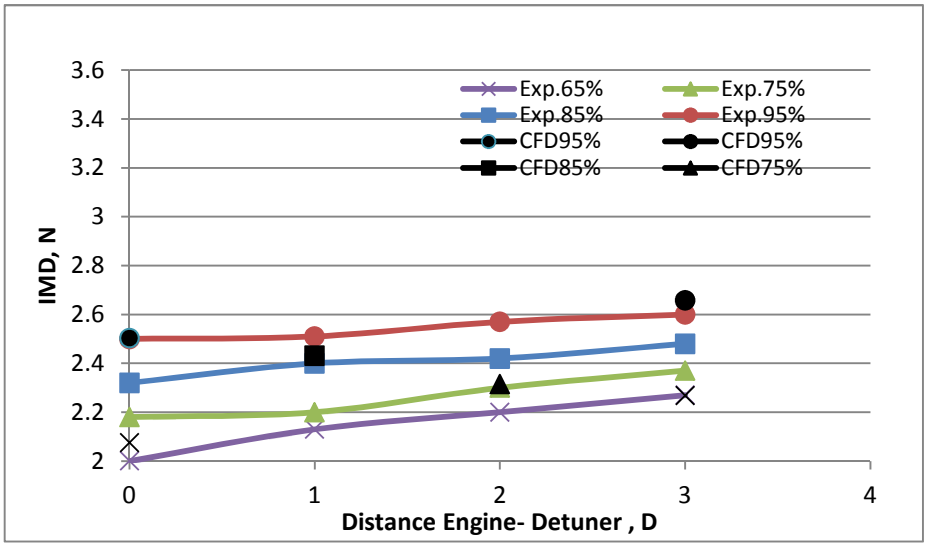

Figure 4.66 Intake momentum drag, CFD with experimental comparison; cell 400x470

The comparison was done also for the cradle drag since it was able to derive it experimentally and by CFD analysis. Figure 4.67 to Figure 4.69 show the comparisons for the cradle drag between the two approaches in the three test cells. The trend lines for both approaches are similar where the cradle drag decreases as the distance between the engine nozzle to the detuner increases. It could be noticed that the cradle drag increases with the engine power settings.

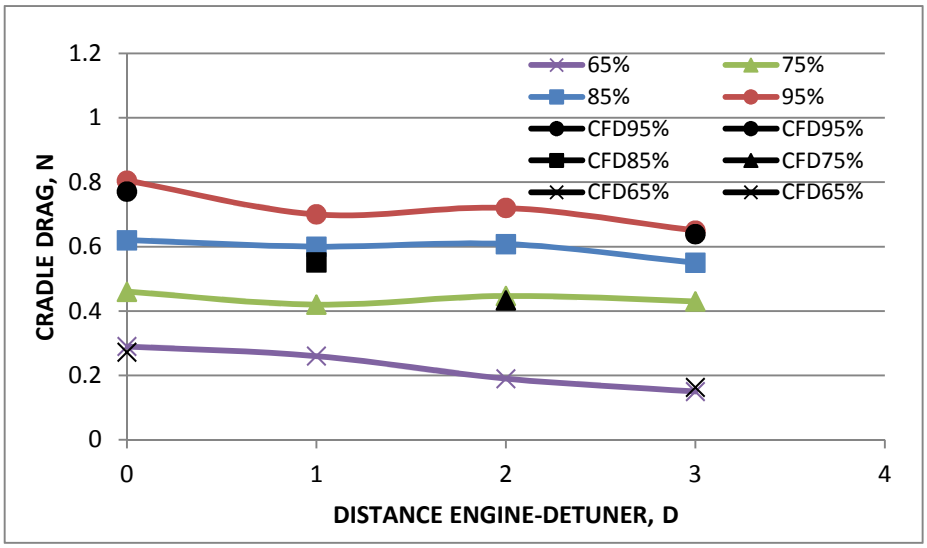

Figure 4.67 Cradle drag, CFD with experimental comparison; cell 700x700

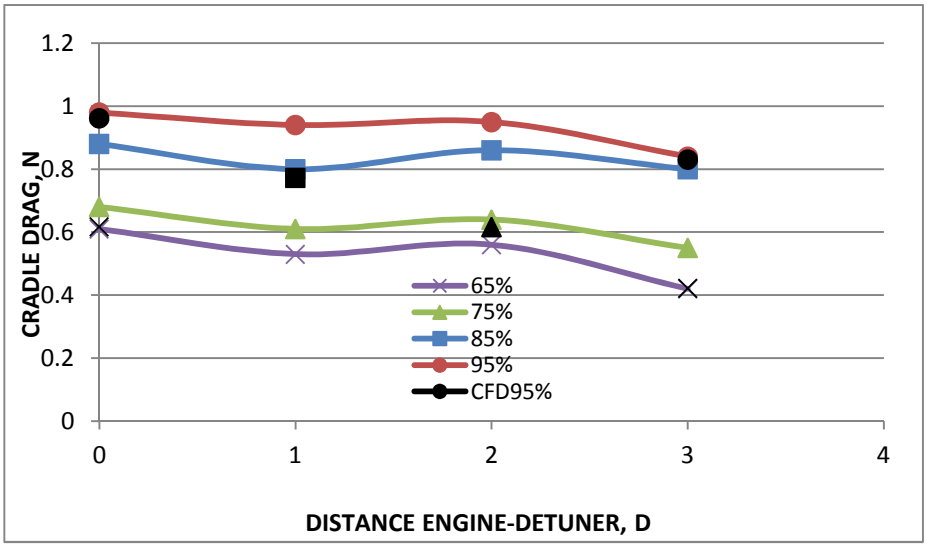

Figure 4.68 Cradle drag, CFD with experimental comparison; cell 550x550

The thrust correction factor which was derived by the CFD simulation increases as the aspect ratio of the test cell decrease. This verifies the same conclusion derived from the experimental analysis.

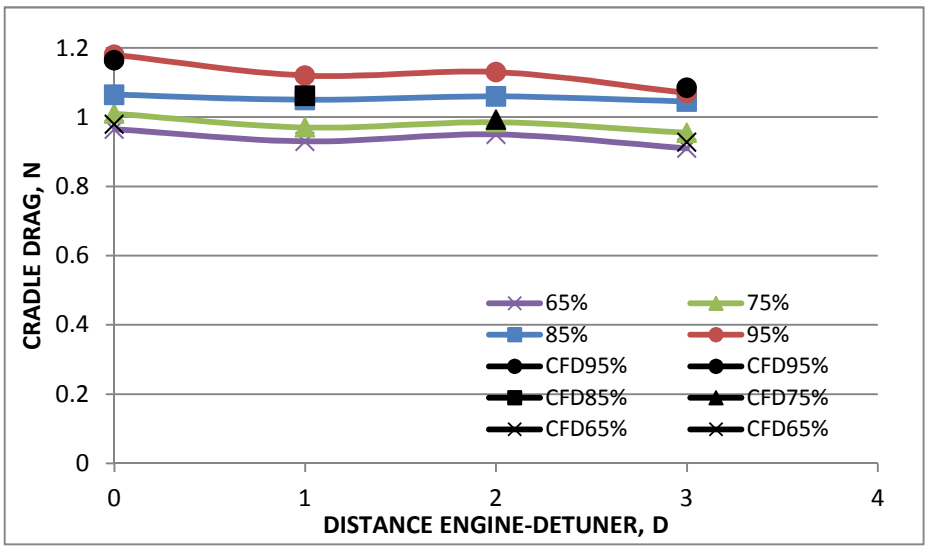

Figure 4.69 Cradle drag, CFD with experimental comparison; cell 400x470

Similarly the comparison was done also for the base drag since it was able to derive it experimentally and by CFD analysis. Figure 4.70 to Figure 4.72 show the comparison for the base drag between the two approaches in the three test cells. The trend lines for both approaches are similar where the base drag decreases as the distance between the engine nozzle to the detuner increases. Both approaches confirm that the base drag

increases as the test cell cross sectional area decreases. The base drag increase with the engine power settings.

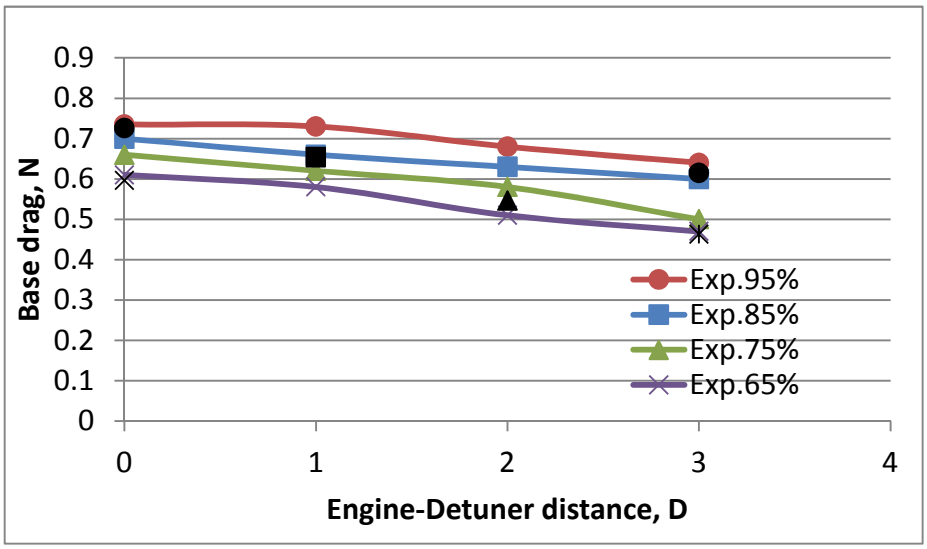

Figure 4.70 Base drag, CFD with experimental comparison; cell 700x700

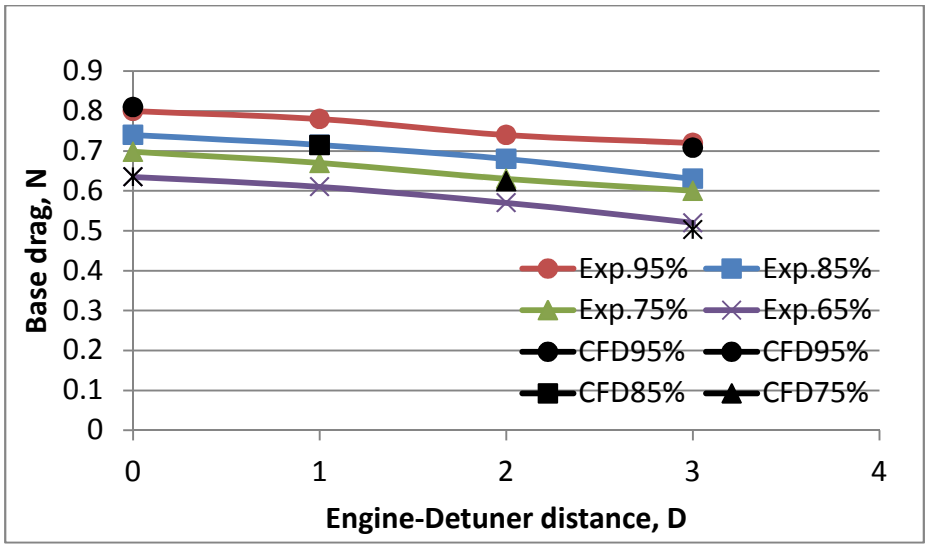

Figure 4.71 Base drag, CFD with experimental comparison; cell 550x550

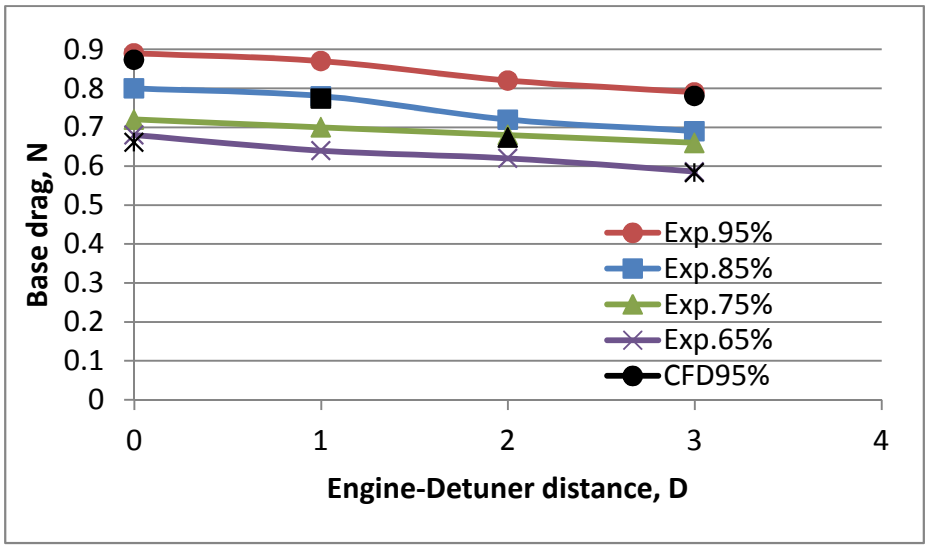

Figure 4.72 Base Cradle drag, CFD with experimental comparison; cell 400x470

In summary the results obtained and the comparison of the CFD analysis and the experimental show a good agreement since the maximum difference between them is 2.0 % of the total load measured. However, not all the thrust correction equations were used in CFD analysis due to the difference in cradle shape.

5. Conclusion and Future Work

The current research work presents the effect of aero gas turbine engine test cell aspect ratio on thrust measurement. This is achieved through both experimental and numerical investigations. The experimental tool involved a change of the test cell cross sectional area and the measurement of the resultant thrust and entrainment ratio.

Cranfield University has invested in the design and production of a small scale test facility that is used in conjunction with a micro jet engine. The test cell which has an aspect ratio of 162 (cross sectional area:700x700) has been designed and built with the facility to change the cell cross sectional area as well as the distance between the engine nozzle and the de-tuner. The instrumentation employed allows for the computation of the total mass flow into the cell as well as the primary mass flow into the engine. These values can then be used to compute the cell entrainment ratio. The facility is also equipped with two high precession load cells attached to the engine that are used to measure the thrust. In addition a number of engine parameters such as rotational speed, fuel flow, and exhaust gas temperature are measured.

Three cell cross sectional areas were considered; 700x700, 550x550, and 400x470 mm. The changes in the test cell were combined with four nozzle to detuner distances; namely, 0, 1, 2 and 3 engine diameters (62mm). The thrust correction factor was defined experimentally as the ratio of the outdoor to indoor thrust measurements. The intake momentum drag, cradle drag, and engine nozzle base drag were computed experimentally using the Rolls Royce First Principle Anemometer.

The effect of the aspect ratio of the test cell on the thrust correction factor was clearly noticed. The thrust correction factor decreases with the aspect ratio. For example, The thrust correction factor for test cell with 700 x700 cross sectional area at the maximum engine rotational speed and 3D engine to detuner distance was 1.03. However for the test cell with 400x470 cross sectional area it was 1.045. This gives a 0.015 thrust correction factor difference between the two extreme test cell cross sectional areas. This result is related to the increase in air velocity as the test cell cross sectional area decreases. It was also possible to observe that thrust correction factor decreases as the engine to detuner distance increase, a maximum of 0.015 difference from 0 to 3D

engine to detuner distance was observed in all test cells. However an increase in engine power setting leads to an increase in the thrust correction factor.

The effect of the test cell aspect ratio on the estimated intake momentum drag, cradle drag and base drag was also investigated. The intake momentum drag increased by 0.9N as the test cell cross sectional area was changed from 700x700 to 400x470. However the cradle drag increased from 0.65N in the test cell of 700x700 cross sectional area to 1.1N in the test cell of 400x470 cross sectional area.

It has been observed that the engine approach velocity increased with the distance between the engine and detuner. Hence, the intake momentum drag increases. However both the cradle drag and base drag had a decreasing trend line with the engine to detuner distance.

A very important contribution in this work has been the computational fluid dynamic (CFD) study of the flow field within the test cell and the computation of the thrust correction factors. The experimental facility was used to determine the total thrust correction through a series of a back to back tests (indoor, outdoor, indoor) while the CFD analysis was carried out in order to be able to compute the individual drag components and study how they are affected by changes in the cell cross sectional area.

For this purpose the CFD model that represents the experimental facility has been developed. The boundary conditions are taken from the experimental facility. The plan was to analyse all the 48 experimental cases. However due to time limitation only 16 cases have been simulated and analysed. The map of the selected cases are shown in Table 4.1. The author believes that these cases give a sufficient reflection of the complete picture.

Three thrust correction equations which were derived by Gullia (Gullia, A. 2006) were intended to be used to derive the thrust correction factors. Due to the differences in the cradle and engine to that used in the original, it was not possible to use two of these equations in the present work. Hence, equation (2.21) is used in the analysis described in section 2.15. This equation considered the computation of the intake momentum drag, cradle drag, base drag, and the potential buoyancy force. The computation of the

first three factors implemented the use of the same experimental methodology. However, in this case, all velocities and pressures are derived from Fluent. The calculation of the potential buoyancy force used a one dimensional equation derived by Gullia (Gullia, A. 2006).

The thrust correction factor which has been derived by CFD showed the same trends to that derived experimentally in all aspects. The thrust correction factor increased as the aspect ratio of the test cell decreases. For example, The thrust correction factor for test cell with 700 x700 cross sectional area at the maximum engine rotational speed and 3D engine to detuner distance was 1.034. However for the test cell with 400x470 cross sectional area it was 1.039. This gives a 0.005 thrust correction factor difference between the two test cell cross sectional areas. It showed a tendency of a decrease as the engine to detuner distance increases; a magnitude of 0.005 difference from 0 to 3D engine to detuner distance was observed in all test cells. Furthermore, the thrust correction factor increases with a similar magnitude with the engine power settings.

The intake momentum drag increased of 0.2N from 0 to 3D engine to detuner distance. However it increased of 1N from 65% to 95% engine power settings. The intake momentum drag increased with 1N from the largest test cell (700x700) to the smallest test cell (400x470). The cradle drag decreased with engine to detuner distance (0.2 N from 0 to 3D). However it increases as the test cell cross section decreases (0.4N from 700x700 to 400x470 test cells cross sectional areas). The base drag increased with the engine power setting. The base drag was 0.5N for test cell cross sectional area of 500x500 at 65% engine power setting. It increased to 0.7N at 95% engine power setting. However 0.1N increase was observed when the engine to detuner distance was increased from 0 to 3D. An increase of 0.1N was observed as the test cell aspect ratio increases.

The comparison of the experimental to CFD results shows closely matching values. In some cases the difference are less than 2%. This has been confirmed on the comparison of the thrust correction factor, intake momentum drag, cradle drag, and base drag.

The following list sum up the major conclusions in this research work:

- The CFD predictions show that the biggest difference with experimental data is only 1 % in TCF for the largest cell size.
- For the smallest test cell this difference increases to only 2%.
- These results in terms of accuracy are lower than what one would normally be expected for general CFD work.
- The CFD model is also predicting the trends in TCF consistently for all power settings, for all test cell cross sections and detuner to nozzle distances.
- These outcomes give the author a great deal of confidence that the CFD model can accurately and consistently predict both magnitude and trends in the change of TCF that occur with both the test cell size and the nozzle to detuner distances.
- Finally therefore the future user of the CFD model can gain enhanced confidents in its use to predict actual engine test bed performance.
- This will provide an opportunity in the future for engine manufacturer to reduce time consuming and expensive engine tests.
- It can improve even further with refinement of the CFD model.
- Against this background, further refinement of the CFD model is a recommended action for future research.

5.1. Future Work

To extend the scope of the experimental data to include:

- Static pressure measurement at a position one diameter inside the detuner
- Whilst the current CFD predictions are good they have been achieved using a small scale engine model. So future work could be attempted to use a full scale to further validate the results.
- implement other thrust correction equations will give more understanding and explaining of the results.
- To use SST k-ω turbulence model as calculation model in CFD will enrich the accuracy of the analysis. The comparison of the results will improve the accuracy of the results.

6. References

Adkins, C. and Anas, A. 1996, The Blast Basket a New Component Used in Testing Large, High By-Pass Ratio, Fan Engines. International Gas Turbine and Aeroengine Congress and Exhibition .

AMT Netherland Manual Olympus. AMT Netherland Revision 2.09 .

Anas, A. 1995. Engine test cell aerodynamics. Msc. Thesis, Cranfield University.

Anderson, J.D. 2001, Fundamental of Aerodynamics. McGraw Hill.

Ashwood, P.F. 1984. Operation and Performance Measurement on Engine in Sea Level Test Facilities. AGARD Lecture Series No. 307

Choi, Y. H. and W. Y. Soh 1990. Computational analysis of the flowfield of a two-dimensional ejector nozzle. AIAA 90-1901 26th Joint Propulsion Conference.

Cross, M.A. 1997. Application of Computational Fluid Dynamics to Analysis of Exhaust Gas-Diffuser Interactions in a Turbine Engine Altitude Test Cell. AIAA 87-2412 23rd Joint Propulsion Conference.

Deen, J. 2004. Turbine Test Cell Phenomena: The Inlet Vortex a Computational and Empirical Analysis. Msc. Thesis, Cranfield University.

Correlation, Operation, Design, and Modification of Turbofan/Jet Engine Test Cells. 2002. Federal Aviation Administration.

Fluent incorporated User's Guide HTML format. Fluent 6.2 Documentation.

Franco, S. 2000. Gas Turbine Engine Test Cell Simulation. Msc. Thesis, Cranfield University.

Freuler, R. J. 1993. Recent Successes in Modifying Several Existing Jet Engine Test Cells to Accomodate Large, High- By-Pass Turbofan Engines. AIAA 93-2542 29th Joint Propulsion Conference and Exhibit.

Freuler, R. J. and Dickman, R.A. 1982. Current Techniques for Jet Engine Test Cell Modelling. AIAA 82-1272 Joint Propulsion Conference.

Ghanshyam, S., Sundararajan, T. and Bhaskaran, K.A. 2003. Mixing and Entrainment Characteristics of Circular and Noncircular Confined Jets. Journal of Fluids Engineering. vol. 125, no. 5, pp. 835-843.

Glenny, D.E. 1968. Ingestion of Debris into Intakes by Vortex Action. N.G.T.E. Pystock Current Paper No. 1114, Ministry of technology.

Gonzalez Galinez, S. E. 2003. Thrust Correction Factors for Small Gas Turbine Indoor Test Bed. Cranfield University.

Gullia, A. 2006. Thrust and Flow Prediction in Gas Turbine Engine Indoor Sea-Level Test Cell Facilities. PhD. Thesis, Cranfield University.

Gullia, A., Laskaridis, P. and Ramsden, K.W. 2006. Ejector Pump Theroy Applied to Gas Turbine Engine Performance inside Indoor Sea-Level Test Cell-Analytical and CFD Study. AIAA 25th Aerodynamic Measurement Technology and Ground Testing Conference.

Gullia, A., Laskaridis, P., Ramsden, K.W. and Pilidis, P. 2005. A Preliminary Investigation of Thrust Measurement Correction in an Enclosed Engine Test Cell Facility. AIAA 43rd Aerospace Sciences Meeting and Exhibit.

Hagues, A. 2005. Gas Turbine Performance in Test Bed: 3D CFD Exhaust System Modelling. Cranfield University.

Hastings, R. 1983, Simulation of a Jet Engine Test Cell, National Research Council, Canada.

Jacques, R. 1984. Aero-Thermodynamic and Acoustic Consideration in the Design of Test Beds for Turbojets and Turbofans. Operation and Performance Measurement on Engines in Sea Level Test Facilities. AGARD Lecture Series No. 132.

Karamanlis, A.I., Sokhey, J.S., Bellomy, D.C. and Dunn, T.C. 1986. Theoretical and Experimental Investigation of Test Cell Aerodynamics for Turbofan Application. AIAA 86-1732.

Karamanlis, A.I., Holmer, W. and Bellomy, D.C. 1985. A Universal Turboshaft Engine Test Cell Design Consideration and Model Test Result. AIAA 23rd Aerospace Sciences Meeting .

Kodres, C.A. and G. L. Murphy. 1998. Jet Engine Test Cell Augmentor Performance. Journal of Propulsion and Power. vol. 14, no. 2, pp. 129-134.

Kromer, S.L. and Dietrich, D.A. 1985. Flow Field Analysis of Low By-Pass Ratio Test Cell. Journal of Aircraft. vol. 22 No 2 pp 99-100, .

Kromer-Oehler, S.L. and D. A. Dietrich. 1984. Computational Analysis of the Flow Field in an Engine Test Cell. AIAA 84-0285.

Launder, B. E. and Spalding, D. B. 1972. Mathematical Models of Turbulence. Academic Press

Laskaridis, P., Gullia, A. and Ramsden, K.W. 2006. A Novel Method for Charactererising Indoor Gas Turbine Test Facilities-Prediction and Control of Engine-Cell Performance. AIAA 25th Aerodynamic Measurement Technology and Ground Testing Conference.

Lighthill, M.J. 1961. Sound Generated Aerodynamically. The Bakerian lecture. Proc. R. Soc. Lond. A 267:147-182.

McLoughlin, A. 2005. Entrainment Ratio Prediction in Gas Turbine Test Beds. Msc. Thesis, Cranfield University.

Mott, L. 2005. Applied Fluid Mechanics. 6th ed., Prentice Hall, NJ (2006).

Nakayama, A. and Jones, J.R. 1996. Vortex Formation in Inlet Flow Near a Wall. AIAA 96-0803 34th Aerospace Sciences Meeting and Exhibit.

Zhu, J. and T.-H. Shih. 1994. A numerical study of confined turbulent jets. Journal of fluids engineering. NASA Technical Memorandum 106197

Nilavalgan, S., Ravindran, M. and Radhakrishna, H. 1988. Analysis of Mixing Characteristics of Flow in a Jet Pump using a Finite-difference Method. The Chemical Engineering Journal. vol. 39, pp. 97-109.

Osborn, A.R. 1990. Experience in Developing and Improving Altitude Test Capability. Comparative Engine Performance Measurement. AGARD Lecture Series.

Parfitt, R.N. 2002a. Concept Demonstration and Initial Derivation of Aerodynamics Thurst Correction for Trent 500 on RR Derby 56 Test Bed Using the Indoor "First Principle" Anemometer Method. Rolls-Royce DNS86648, .

Parfitt, R.N. and M. Bristow 2006. Derivation of Aerodynamic Thrust Correction for an Indoor Gas Turbine Engine Test Facility Using the ''First Principles'' Anemometer Method. 25th International Congress of the Aeronautical Sciences.

Prufert, M.B. and Williamson, J.W. 2000. Computational Analysis of Turbine Engine Test Cell Flow Phenomena. AIAA 2000-2210 Aerodynamic Measurement and Ground Testing Conference.

Quinn, B. 1976. Ejector Performance at High Temperature and Pressure. Journal of Aircraft, vol. 13, number 12.

Razinsky, E. and Brighton, J.A. 1971. Confined Jet Mixing for Nonseparating Conditions. Journal of Fluids Engineering, Trans. ASME, vol. 94, pp. 333--349.

Rios, R.M. and Martin, R.M. 1998. Thrust Correction on Jet Engine in Sea Level Test Facility. AIAA 98-3109 34th AIAA/ASME/SAE/ASEE Joint Propulsion Conference and Exhibit.

Rodert, L.A. and F. B. Garrett 1955. Ingestion of Foreign Objects into Turbine Engines by Vortices, NACA.

Rolls Royce plc 2003. Thrust Measurement Rig For A Micro Gas Turbine. Assembly, Operation and Maintenance Manual. Rolls Royce Document Ref.16180.

Rudnitski, D.M. 1990. Experience in Developing and Improving Ground-Level Test Capability. Comparative Engine Performance Measurement, AGARD Lecture Series No. 169.

Rudnitski, D.M. 1984, Performance Derivation of Turbojet and Turbofans from Tests in Sea-Level Tests cells. Operation and Performance Measurement on Engines in Sea Level Test Facilities. AGARD-LS-132.

SAE .1976. Turbofan and Turbojet Gas Turbine Engine Test Cell Correlation. SAE APR741

SAE Committee E-33. 1985. In-Flight Thrust Determination.SAE AIR 1703.

Sapp, C.N. and Netzer, D.W. 1978. Experimental Investigation of Turbojet Test Cell Augmenters. Monterey, California: Naval Post Graduate School 67-78-009.

Saravanamuttoo, H.I.H., Rogers, G.F.C. and Cohen, H. 1996. Gas Turbine Theory. Prentice Hall

Vyas, B.D. and Kar, S. 1975. Study of the Entrainment and Mixing Process for an Air to Air jet Ejector. 2ND Symposium on Jet Punps and Ejectors and Gas Lift Techniques. pp. C2-15 to C2-25.

Walsh, P.P. and Fletcher, P. 1998. Gas Turbine Performance. Blackwell Science.

Wei Hua, H. 2009. Investigation into the Vortex Formation and Infrasound Generation in a Jet Engine Test Cell. University of Canterbury.

Woodfield, P.L., NAKABE, K. and Suzuki, K. 2000. Numerical Computation on Recirculation Flow Structures in Confined Co-Axial Laminar Jets. Suchi Ryutai Rikigaku Shinpojiumu Koen Ronbunshu, vol. 14, pp. 95.

Yinhai, Z., Wenjian, C., Changyun, W. and Yanzhong, L. 2008. Numerical investigation of geometry parameters for design of high performance ejectors. Applied Thermal Engineering.

APPENDIX A. Bellmouth calibration data

A1. Bellmouth calibration data

Power Setting: 60%

Mini Turbine/Cranfield University

PTdcr1	PTdcr2			P-p	Vj	V_L	Wcell	
0.196	-0.088							
0.194	-0.212	Bottom Wall	1stLcorner(LD)	0.12	4.44413596			
0.207	-0.21			0.133	4.6786713			
0.206	-0.215			0.132	4.66104912	**4.607025**	**0.0618054**	
0.206	-0.212			0.132	4.66104912			
0.205	-0.22			0.131	4.64336007			
0.2	-0.216			0.126	4.55388424			
0.17	-0.213	Left Wall	4thBto(LD)corner	0.098	4.0161484			
0.172	-0.214			0.1	4.05692253			
0.213	-0.219			0.141	4.81732859	**4.4817285**	**0.0601245**	
0.201	-0.217			0.129	4.60777824			
0.208	-0.219			0.136	4.73114402			
0.204	-0.21			0.132	4.66104912			
0.162	-0.207		2ndBto(LD)corner	0.088	3.80573067			
0.191	-0.211	Right Wall		0.117	4.38823266			
0.203	-0.209			0.129	4.60777824	**4.4491579**	**0.0596875**	
0.209	-0.209			0.135	4.71371801			
0.2	-0.207			0.126	4.55388424			
0.204	-0.211			0.13	4.62560337			
0.147	-0.205		1stBto(LD)corner	0.075	3.51339797			
0.204	-0.204			0.132	4.66104912			
0.195	-0.201	Top Wall		0.123	4.49934474	**4.492149**	**0.0602643**	
0.212	-0.212			0.14	4.80021547			
0.212	-0.211			0.14	4.80021547			
0.205	-0.215			0.133	4.6786713			
0.211	-0.218							
0.208	-0.215							
0.207	-0.21							
0.211	-0.144	Corner(LD)	-0.122	0.066	3.29585944			
0.208	-0.079							
0.209	-0.123		-0.122	0.087	3.78404542			
0.207	-0.106		-0.122	0.104	4.13726542	**4.0949205**	**0.0716547**	
0.21	-0.113		-0.122	0.097	3.99560531			
0.213	-0.08		-0.122	0.13	4.62560337			
0.21	-0.074		-0.122	0.136	4.73114402			
							0.314	**Total**

Table A. 1 Bellmouth calibration data (power setting 65%)

Power Setting: 75%

Mini Turbine/Cranfield University

PTdcr1	PTdcr2			P-p	Vj	V_L	Wcell	
0.204	-0.048							
0.188	-0.157	Bottom Wall	1stLcorner(LD)	0.1	4.056882002	4.39741	0.058994	
0.214	-0.154			0.126	4.553838752			
0.213	-0.159			0.125	4.535731966			
0.205	-0.165			0.117	4.388188823			
0.203	-0.169			0.115	4.350521269			
0.211	-0.164			0.123	4.499299794			
0.203	-0.163	Left Wall	4thBto(LD)corner	0.116	4.369395636	4.411328	0.059181	
0.196	-0.161			0.109	4.235509157			
0.199	-0.17			0.112	4.29340035			
0.215	-0.173			0.128	4.589838038			
0.212	-0.171			0.125	4.535731966			
0.207	-0.164			0.12	4.444091571			
0.195	-0.169	Right Wall	2ndBto(LD)corner	0.097	3.995565395	4.140284	0.055545	
0.193	-0.165			0.095	3.954159455			
0.22	-0.167			0.122	4.480972631			
0.201	-0.169			0.103	4.117285553			
0.205	-0.169			0.107	4.196471373			
0.2	-0.167			0.102	4.097249981			
0.199	-0.168	Top Wall	1stBto(LD)corner	0.104	4.137224098	4.189539	0.056206	
0.198	-0.171			0.103	4.117285553			
0.207	-0.169			0.112	4.29340035			
0.203	-0.176			0.108	4.216035448			
0.202	-0.183			0.107	4.196471373			
0.201	-0.181			0.106	4.176815661			
0.202	-0.179							
0.206	-0.179							
0.205	-0.171							
0.204	-0.128	Corner(LD)	-0.115	0.035	2.400083759	3.689702	0.064565	
0.203	-0.056							
0.201	-0.079		-0.115	0.084	3.718193772			
0.201	-0.083		-0.115	0.08	3.628585573			
0.2	-0.06		-0.115	0.103	4.117285553			
0.202	-0.057		-0.115	0.106	4.176815661			
0.2	-0.061		-0.115	0.102	4.097249981			
							0.294	Total

Table A. 2 Bellmouth calibration data (power setting 75%)

Power Setting: 85%

Mini Turbine/Cranfield University

PTdcr1	PTdcr2			P-p	Vj	V_L	Wcell	
0.208	-0.062							
0.215	-0.192	Bottom Wall	1stLcorner(LD)	0.133	4.678601195	4.735929	0.063537	
0.208	-0.185			0.126	4.553816009			
0.22	-0.187			0.138	4.76573347			
0.221	-0.19			0.139	4.782969452			
0.224	-0.196			0.142	4.834308698			
0.222	-0.192			0.14	4.800143544			
0.175	-0.189	Left Wall	4thBto(LD)corner	0.095	3.954139706	4.536887	0.060866	
0.187	-0.189			0.107	4.196450414			
0.205	-0.196			0.125	4.535709313			
0.229	-0.198			0.149	4.952030845			
0.218	-0.213			0.138	4.76573347			
0.221	-0.188			0.141	4.81725641			
0.199	-0.192	Right Wall	2ndBto(LD)corner	0.114	4.331543025	4.552093	0.06107	
0.194	-0.19			0.109	4.235488003			
0.21	-0.189			0.125	4.535709313			
0.225	-0.187			0.14	4.800143544			
0.218	-0.187			0.133	4.678601195			
0.221	-0.19			0.136	4.73107313			
0.189	-0.186	Top Wall	1stBto(LD)corner	0.111	4.274169061	4.757261	0.063823	
0.224	-0.189			0.146	4.901924691			
0.23	-0.189			0.152	5.001635064			
0.218	-0.196			0.14	4.800143544			
0.215	-0.203			0.137	4.748434924			
0.219	-0.203			0.141	4.81725641			
0.22	-0.206							
0.218	-0.204							
0.217	-0.192							
0.217	-0.15	Corner(LD)	-0.13	0.042	2.629146899	4.068492	0.071194	
0.218	-0.058							
0.217	-0.12		-0.13	0.072	3.442361336			
0.219	-0.091		-0.13	0.101	4.07709559			
0.218	-0.053		-0.13	0.139	4.782969452			
0.216	-0.057		-0.13	0.135	4.713647387			
0.216	-0.054		-0.13	0.138	4.76573347			
							0.32	Total

Table A. 3 Bellmouth calibration data (power setting 85%)

Power Setting: 95%

Mini Turbine/Cranfield University

PTdcr1	PTdcr2			P-p	Vj	V_L	Wcell
0.21	-0.052						
0.213	-0.186	Bottom Wall	1stLcorner(LD)	0.133	4.678624562	**4.725182**	**0.063392**
0.215	-0.182			0.135	4.713670929		
0.215	-0.191			0.135	4.713670929		
0.215	-0.186			0.135	4.713670929		
0.217	-0.194			0.137	4.74845864		
0.219	-0.184			0.139	4.78299334		
0.184	-0.189	Left Wall	4thBto(LD)corner	0.108	4.216035448	**4.840142**	**0.064934**
0.224	-0.185			0.148	4.935409966		
0.221	-0.189			0.145	4.885132832		
0.231	-0.19			0.155	5.05077736		
0.224	-0.201			0.148	4.935409966		
0.229	-0.182			0.153	5.018085901		
0.194	-0.185	Right Wall	2ndBto(LD)corner	0.114	4.331564659	**4.679433**	**0.062778**
0.201	-0.182			0.121	4.462570202		
0.213	-0.181			0.133	4.678624562		
0.228	-0.181			0.148	4.935409966		
0.224	-0.181			0.144	4.868258402		
0.22	-0.185			0.14	4.800167518		
0.192	-0.182	Top Wall	1stBto(LD)corner	0.116	4.369395636	**4.733634**	**0.063505**
0.218	-0.186			0.142	4.834332843		
0.219	-0.182			0.143	4.851325278		
0.209	-0.184			0.133	4.678624562		
0.215	-0.199			0.139	4.78299334		
0.221	-0.191			0.145	4.885132832		
0.219	-0.201						
0.219	-0.203						
0.218	-0.187						
0.217	-0.132	Corner(LD)	-0.134	0.054	2.981187255	**4.220737**	**0.073858**
0.217	-0.051						
0.216	-0.107		-0.134	0.079	3.605835596		
0.219	-0.068		-0.134	0.118	4.406901866		
0.217	-0.052		-0.134	0.134	4.696180438		
0.215	-0.043		-0.134	0.143	4.851325278		
0.217	-0.047		-0.134	0.139	4.78299334		
							0.328 **Total**

Table A. 4 Bellmouth calibration data (power setting 95%)